

Modification Strategy for Mn-based Layered Transition Metal Oxide as Sodium-ion Battery
Cathodes

by

Ka Ho Wong

A thesis

presented to the University of Waterloo

in fulfillment of the

thesis requirement for the degree of

Master of Applied Science

in

Chemical Engineering (Nanotechnology)

Waterloo, Ontario, Canada, 2024

© Ka Ho Wong 2024

Author's Declaration

This thesis consists of material all of which I authored or co-authored: see Statement of Contributions included in the thesis. This is a true copy of the thesis, including any required final revisions, as accepted by my examiners.

I understand that my thesis may be made electronically available to the public.

Statement of Contributions

The body of this thesis is based upon unpublished works.

Chapter 1, 2, 3, 5 of this thesis contain paragraphs from a submitted review paper of which I am the first author. My co-authors are Maiwen Zhang, Tingzhou Yang, Qianyi Ma, Shuqi Dai, Jing Wei, Ganesh Kuma, Ali Abdulkareem AlHammadi, Georgios Karanikolos, Elena Bekyarova, Ali Elkamel, Aiping Yu. I conducted conceptual study design, data collection, and manuscript writing.

Chapter 4, 5 of this thesis contain paragraphs from an unpublished research work. I conceptualized study design, performed data collection, and constructed the manuscript.

Abstract

Sodium-ion batteries (SIBs) are being touted as the future of energy storage. However, the lackluster performance of current cathode technology is a major roadblock to their widespread use. Among the promising candidates for cathodes, layered sodium manganese oxide stands out due to its low cost and higher energy density. However, its cycling performance is limited due to structural and surface instabilities. To overcome these challenges, researchers are exploring various strategies, such as doping, coating, and heterostructure design, to enhance the performance of manganese-based oxide. Doping involves introducing foreign atoms to enhance structural stability and electrochemical performance. Coating is a surface protection method, while heterostructure design involves developing a composite material composed of different crystal phases of sodium manganese oxide to leverage the intrinsic advantage of each phase. By analyzing the latest research, a novel coating approach of utilizing functionalized polymer (polyamic acid) as an encapsulation layer for P2-Na_{0.7}MnO₂ cathode is demonstrated. The polymer is equipped with abundant functional groups such as hydroxyl, carboxyl, amide, fluoromethyl, and aromatic, that endow a high oxidative stability and high toughness, thereby mitigating structural transition and electrolyte decomposition. Additionally, a high percentage of polar groups enable ionic conduction of Na⁺ through the polymer coating, as well as reducing active material dissolution through a chelation mechanism. Hence, the encapsulated cathode exhibits significant improvement in its cycling performance, maintaining stable discharge capacity for 500 cycles at 1000 mA g⁻¹.

Acknowledgements

This work has been supported by the University of Waterloo.

I would like to express my sincere gratitude to my supervisor, Dr. Aiping Yu, for her guidance and support during my MASc studies.

The work would not have been possible without the support and mentorship of colleagues and mentor, including Dr. Maiwen Zhang, Shuqi Dai, Dr. Weinan Zhao, Qianyi Ma, Dr. Tingzhou Yang, Dr. Rui Gao.

I would also like to acknowledge and thank the readers of this thesis: Dr. Aiping Yu, Dr. Ali Elkamel, Dr. Ting Tsui.

Table of Contents

Author's Declaration	ii
Statement of Contributions.....	iii
Abstract	iv
Acknowledgements	v
List of Figures	viii
List of Tables.....	xi
List of Abbreviations.....	xii
Chapter 1 Introduction.....	1
Chapter 2 Current Limitation of Mn-based Layered Oxide	4
Chapter 3 Literature Review on Modification Strategies	9
3.1 Doping.....	9
3.1.1 Single doping.....	11
3.1.2 Multiple doping	17
3.2 Coating	21
3.3 Heterostructure	26
3.4 Summary	31
Chapter 4 Functionalized Polyamic Acid as a Protective Layer on a P2-Na _{0.7} MnO ₂ cathode for Sodium-ion Batteries.....	34
4.1 Introduction	34
4.2 Results and Discussions	35
4.3 Experimental	45
Chapter 5 Conclusion	47
Supplementary Information.....	50

References 57

List of Figures

Figure 1. The crystal structure and Na environment of a) P2 and O3-phase Na_xTMO_2 . b) Schematic of a sodium ion battery.	3
Figure 2. a) Schematic illustration of the O3 and P2 phase transition upon de/intercalation of Na^+ . Reproduced with permission.[12] b) ABF STEM showing intergrown P2 and O2-phase. c) schematic illustration of structural collapse due to extraction of Na^+ in P2-phase. Reproduced with permission. [26] d) STEM showing the growth of cracks with cycling. Reproduced with permission.[27] e) unit cell volume variation as a function of charging voltage. f) Cross sectional SEM images of cycled electrode when charged to 3.58 V and 4.0 V. Reproduced with permission.[25]	5
Figure 3. Schematic illustration of material degradation in $\text{Na}_x\text{MnyTM}_{1-y}\text{O}_2$	8
Figure 4. a) evolution of Mg^{2+} doping site with increasing Mg^{2+} concentration. Reproduced with permission.[74] b) schematic of oxygen redox mechanism showing cation-vacancy clusters and loss of honeycomb ordering. Reproduced with permission.[86] c) proposed P2-O2 suppression mechanism due to oxygen redox. Reproduced with permission.[26] d) superstructure schematic and 1st cycle charge-discharge curve of honeycomb-ordered $\text{Na}_{0.75}[\text{Li}_{0.25}\text{Mn}_{0.75}]\text{O}_2$ and ribbon-ordered $\text{Na}_{0.6}[\text{Li}_{0.2}\text{Mn}_{0.8}]\text{O}_2$. Reproduced with permission.[98] e) schematics of α - α , α - β , and α - γ stackings. Reproduced with permission.[99]	14
Figure 5. a) ^7Li NMR spectra at different stage of first charge/discharge cycle of samples with single honeycomb (LiMn_6 , left) and dual honeycomb ($\text{LiMn}_6\text{-MgMn}_6$, right) showing a reversible Li shuttling in the dual honeycomb sample. Reproduced with permission.[110] b) schematic summarizing the structural evolution of $\text{O}_3\text{-NaNi}_{0.25}\text{Mg}_{0.05}\text{Cu}_{0.1}\text{Fe}_{0.2}\text{Mn}_{0.2}\text{Ti}_{0.1}\text{Sn}_{0.1}\text{O}_2$, showing capacity were mainly stored in P-phase. Reproduced with permission.[113] c) schematic illustrations of active facets {010} family of planes for Na^+ de/intercalation. d) experimentally measured percentage of {010} facet in HEO and low entropy (NaMnO_2) materials. Reproduced with permission.[116]	20
Figure 6. a) schematics showing the layer and bulk structure, and f) cycling performance of $\text{NaMnTi}_{0.1}\text{NiO}_2$ with a reconstructed Ti(III)-concentrated spinel-like oxide layer. Reproduced with permission.[128] b) schematics showing design strategies of Zr^{4+} doping induced ZrO_2 coating. Reproduced with permission.[128] c) schematic illustration of suppressed oxygen release mechanism with Ca/Ti co-doping and CaTiO_2 coating. Reproduced with permission.[132] d) schematic illustrations of MLD deposition of alucone. Reproduced with permission.[136] e) schematic illustrations of PR-co-PAA coating protective mechanisms. Reproduced with permission.[138]	26

Figure 7. a) the SAED patterns, b) HADDF and c) ABF images of P2/O3 Na_{0.66}Li_{0.18}Mn_{0.71}Ni_{0.21}Co_{0.08}O_{2+d} composite. Reproduced with permission.^[140] d) ABF images and e) the GPA analysis of Na-P2/Li-O3 composite. Reproduced with permission.^[143] f) crystal structure of tunnel-phase. g) proposed mechanism for P2-tunnel current redistribution effect. Reproduced with permission.^[149] 30

Figure 8. a) Schematic illustration of coating of NM cathode and multiple protective mechanism of PAA coating. b) Chemical structure, c) ¹⁹F (top) and ¹H (bottom)NMR spectra, and d) FTIR spectrum of the functionalized PAA polymer. e) XRD patterns of NM and PAA@NM. f) SEM image, g) EDS mapping, and h) HR-TEM image of PAA@NM..... 36

Figure 9. XPS spectra of PAA@NM and NM powder a) Na 1s, b) Mn 2p, c) O 1s, d) C 1s, e) F 1s, and f) N 1s..... 38

Figure 10. a) charge-discharge curve of the initial activation at 10 mA g⁻¹, and b) corresponding dQ dV⁻¹ profiles for the PAA@NM cathode. c) rate capability test at different current density from 50 mA g⁻¹ to 2000 mA g⁻¹, d) cycling test at 200 mA g⁻¹, and e) long cycling test at 1000 mA g⁻¹ for NM and PAA@NM cathodes..... 41

Figure 11. a) Nyquist plot of pre-cycling, and b) after 500 cycles at 1000 mA g⁻¹. SEM image of the electrodes c) before and d) after 500 cycles at 1000 mA g⁻¹. 44

Figure S 1. a) GPC, b) XRD, and c) TGA results of the functionalized PAA polymer. 50

Figure S 2. a-b) SEM images and c-d) TEM images of NM..... 51

Figure S 3. a) charge-discharge curve of NM cathode and b) corresponding dQ dV⁻¹. c) charge and discharge capacities, and corresponding Coulombic efficiencies during the first cycles of activation process for NM and d) PAA@NM cathodes..... 52

Figure S 4. Comparison of XRD patterns of NM and PAA@NM cathodes when charged to 4.2 V and discharged to 1.5 V..... 52

Figure S 5. a) Charge-discharge curve during rate capability test of NM and b) PAA@NM cathodes. 53

Figure S 6. a) rate capability, b) cycling test at 200 mA g⁻¹, and c) cycling test at 1000 mA g⁻¹ for the 1wt% PAA coated NM cathodes..... 54

Figure S 7. a) Randles model for fitting EIS results. b) comparison of experimental and fitted impedance data. 55

Figure S 8. Nyquist plot of fresh NM and PAA@NM cathode..... 55

Figure S 9. Additional SEM images of cycled cathode. a-b) NM cathode. c-d) 2PAA@NM cathode.
..... 56

List of Tables

Table 1. Summary of model parameters of pristine and cycled NM and PAA@NM cathodes.	42
--	----

List of Abbreviations

ABF	annular bright field
AIMD	ab initio molecular dynamics
ALD	atomic layer deposition
CEI	cathode-electrolyte interphase
COHP	crystal orbital Hamilton populations
DFT	density functional theory
DMAC	dimethylacetamide
DMC	dimethyl carbonate
DOS	density of states
DSC	differential scanning calorimetry
EC	ethylene carbonate
EDS	energy-dispersive X-ray spectroscopy
EIS	electrochemical impedance spectroscopy
EVs	electric vehicles
FEC	fluoroethylene carbonate
FTIR	Fourier-transform infrared spectroscopy
GITT	galvanostatic intermittent titration technique
GPA	geometric phase analysis
GPC	gel permeation chromatography
HADDF	high-angle annular dark-field
HC	hard carbon
HEO	high entropy oxide

HR-TEM	high-resolution transmission electron microscope
ICP	inductively coupled plasma
LIBs	lithium-ion batteries
MAS	magic-angle-spinning
MD	molecular dynamics
MLD	molecular layer deposition
mRIXS	mapping of resonant inelastic X-ray scattering
MSDs	mean square displacements
NASICON	sodium (Na) super ionic conductor
NMP	N-Methylpyrrolidone
NMR	nuclear magnetic resonance
OCV	open circuit voltage
ODA	4,4'-diaminodiphenyl ether
PAA	polyamic acid
PC	propylene carbonate
PMDA	pyromellitic dianhydride
PVDF	polyvinylidene fluoride
RCM	reductive coupling mechanism
RDF	radial distribution function
SAED	selected area electron diffraction
SEI	solid-electrolyte interphase
SEM	scanning electron microscope
SIBs	sodium-ion batteries

sPFY	super-partial fluorescence yield
STEM	scanning transmission electron microscopy
TGA	thermogravimetric analysis
THF	tetrahydrofuran
ToF-SIMS	time-of-flight secondary-ion mass spectroscopy
XAS	X-ray absorption spectroscopy
XPS	X-ray photoelectron spectroscopy
XRD	X-ray diffraction

Chapter 1 Introduction

Lithium-ion batteries (LIBs) are efficient energy storage systems that play a crucial role in the shift towards a sustainable future, powering the growing use of electric vehicles (EVs). However, the depletion of lithium reserves and uneven distribution of raw materials such as cobalt, with over half the global supply originating from the Congo, bring about unstable costs and societal inequalities, challenging the sustainability of EVs. This has led to the development of next-generation energy systems. Among promising candidates, interest in advancing sodium-ion batteries (SIBs) have been suddenly renewed in 2008 owing to the large similarities between the two systems. There exist two major branches of cathode technologies, namely layered transition metal oxides, and polyanion compounds. Polyanion compounds feature better structural stability thus longer cycling^[1], while layered transition metal oxides output higher capacity.^[2] The classification of polyanion compounds includes phosphates (olivine^[3] and maricite^[4] NaFePO_4 , NASICON- $\text{Na}_3\text{V}_2(\text{PO}_4)_3$ ^[5]), pyrophosphate ($\text{Na}_2\text{FeP}_2\text{O}_7$ ^[6], $\text{Na}_2(\text{VO})\text{P}_2\text{O}_7$ ^[7]), fluorophosphate (NaVPO_4F ^[8]), sulfates ($\text{Na}_2\text{Fe}(\text{SO}_4)_2$ ^[9]), and silicate ($\text{Na}_2\text{FeSiO}_4$ ^[10]).

The common phases of layered sodium transition metal oxide (Na_xTMO_2 , typically $x \leq 1$) are P2 and O3, following the naming convention coined by Delmas who studied them in 1980.^[11] Specifically, the layered structures consist of sheets made of MO_6 edge-sharing octahedra (thereafter called the TM layer), between which the sodium atoms are intercalated (AM layer), taking up either the prismatic (P) or octahedral (O) environments. The TM layer can exist as three different possible packings, namely A, B, and C, which are determined by the positions of oxygen atoms.

The crystal structure of O3-type Na_xTMO_2 is classified as 3R phase (space group: R3m). It consists of three different repeating TMO_2 layers, which are AB, BC, and CA, as shown in Figure 1a. Between the layers, Na^+ are accommodated in the octahedral sites. As such, the material is categorized as O3. That is, “O” describes the Na^+ environment, while the number indicates the repeating number of TMO_2 layers. Similarly, the unit cell of P2-type Na_xTMO_2 consists of AB and BA TMO_2 layers, with Na^+ residing at the prismatic layer. It is classified as 2H phase (space group: $\text{P6}_3/\text{mmc}$). Empirically speaking, common P2-phase with prismatic environment can only be stabilized when $0.44 < x < 0.7$ in Na_xTMO_2 due to the large ionic radius of Na^+ , while O3-phase can typically accommodate $x = 1$ in its structure (Na_xTMO_2 , $x = 1$). From a practicality point of view, lower Na^+ content of P2 can lead to lower initial charge capacity compared to the following discharge capacity that results in inferior

Coulombic efficiency. However, P2-phase generally has a higher in-plane Na^+ diffusivity compared to O3-phase, leading to a higher rate capability that can be promising for high power applications. The origin of which is explained by the Na^+ accommodation site; in O3-phase, high energy barrier prohibits the direct hopping of Na^+ from one octahedral site to another, forcing Na^+ to transport through interstitial tetrahedral sites. Comparatively, the diffusion barrier of Na^+ in-plane conduction in P2-phase is smaller due to the open diffusion framework which is beneficial for the intercalation kinetics.^[12]

A schematic showing cathode, anode, and electrolyte of a typical SIB full cell is shown in Figure 1b. During charging, Na^+ ions are extracted from cathode, and inserted into anode. Upon discharge, Na^+ ions are extracted from anode and intercalated into cathode. Since the discovery of hard carbon (HC) for its electrochemical activities in a SIB, it remains undoubtedly the top-choice for SIB anode, owing to its high capacity (over 300 mAh g^{-1}), low-cost, and various facile synthesis routes such as high temperature carbonization of biomass. For instance, Mitlin et al. reported a banana peels-derived HC with 355 mAh g^{-1} .^[13] The model of HC was introduced by Dahn and coworkers to be “house of cards” in 2000, where fragments of few-layers graphene with random orientations are embedded in a carbon matrix.^[14] Several Na^+ storage mechanisms have been proposed, but they can be summarized as a combination of adsorption and intercalation of Na^+ in HC.^[15] Nonetheless, utilizing HC in an unoptimized setting can lead to a high first cycle capacity loss.

On that note, design of electrolyte (solvent, salt, additive) can have a significant impact on the performance of anode.^[16] In a full cell consists of Na_xTMO_2 as cathode and HC as anode, the commonly used solvents are propylene carbonate (PC), ethylene carbonate (EC), and dimethyl carbonate (DMC), while the salt are almost exclusively sodium perchlorate (NaClO_4) and sodium hexafluorophosphate (NaPF_6) for organic solvent-based electrolyte. Fluoroethylene carbonate (FEC) is a popular electrolyte additive owing to its prominent effect in creating stable solid-electrolyte interphase (SEI) on HC. A summary of various combinations of electrolyte systems with improved performance was provided.^[17]

Various Na_xTMO_2 cathode materials such as NaCrO_2 ^[18] and NaVO_2 ^[19] have been shown to be electrochemically active in SIBs, but their practical capacities are limited to 120 mAh g^{-1} . Mn-based system such as $\text{Na}_{0.6}\text{MnO}_2$ ^[20], $\text{Na}_{2/3}\text{Fe}_{1/2}\text{Mn}_{1/2}\text{O}_2$ ^[21], and $\text{Na}_{2/3}\text{Ni}_{1/3}\text{Mn}_{2/3}\text{O}_2$ ^[22] demonstrated relatively high capacity of at least 160 mAh g^{-1} . $\text{Na}_{0.5}\text{CoO}_2$ ^[23] can deliver similar charge storage capability, but the socioeconomical issues of Co can limit their scalability. Contrary to Co, earth-abundance and low-cost of Mn-based cathode material offers as a more scalable technology.

Despite higher capacity, Mn-based layered oxide ($\text{Na}_x\text{Mn}_y\text{TM}_{1-y}\text{O}_2$) suffers from structural and surface instability that result in fast energy density fading and low diffusion rate, and its below-3V operating voltage prevents it from high-voltage applications. In addition, the energy density of Mn-based layered oxide is still at an unsatisfactory level for practical applications. Chapter 2 explains the limitations of $\text{Na}_x\text{Mn}_y\text{TM}_{1-y}\text{O}_2$ and chapter 3 provides an update on the existing strategies to improve them. Finally, chapter 4 presents a novel strategy of applying a functionalized polymer as a protective coating to improve the cyclability of a $\text{Na}_{0.7}\text{MnO}_2$ cathode.

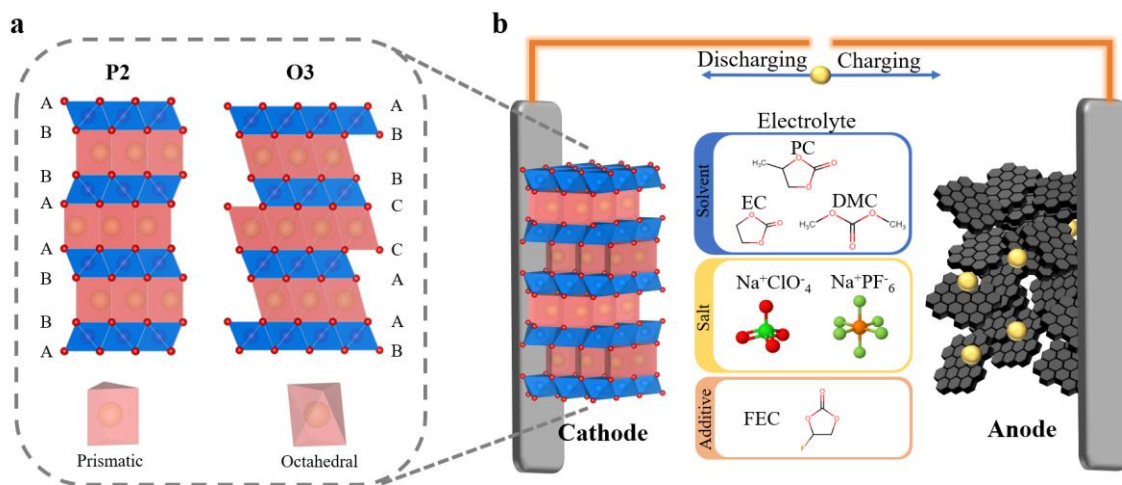


Figure 1. The crystal structure and Na environment of a) P2 and O3-phase Na_xTMO_2 . b) Schematic of a sodium ion battery.

Chapter 2 Current Limitation of Mn-based Layered Oxide

The commonly observed phenomenon during Na⁺ de/intercalation in P2 and O3-phases is the phase transition, which is shown in Figure 2a. In P2-phase, as prismatic environment is stabilized by Na⁺, the extraction of Na⁺ upon charging the material causes the TMO₂ layer to glide without destroying the TM-O bonds. In other words, the electrostatic repulsion between the oxygen of adjacent TMO₂ layers can no longer be screened by the Na⁺ ions. The resulting phase is “O2”, whose unit cell consists of AB and AC TMO₂ layers, and the remaining Na⁺ occupies in the octahedral site. The re-insertion of Na⁺ in the following discharge cycle can convert it back to P2-phase, however, such transition is not completely reversible due to the occurrence of stacking faults.^[22] The whole picture of phase transition in O3-phase is a bit more complicated, where it undergoes the following transitions: hexagonal O3 → monoclinic O'3 → hexagonal P3 → monoclinic P'3 → hexagonal P3' → hexagonal O'3.^[24,25]

In P2-phase, the de-intercalation of Na⁺ causes the interlayer spacing (spacing between adjacent TMO₂ layers) to continuously increase upon reaching ~0.3 mol Na, where a P2/O2 intergrown composite started to appear (Figure 2b). Further de-intercalation causes the O2 phase to grow, which can be visualized with annular bright field (ABF) scanning transmission electron microscopy (STEM). The onset of O2 formation causes sudden collapse of interlayer spacing, from 5.5 Å to 4.5 Å, in the area that O2 formed (Figure 2c).^[26] Due to a large lattice mismatch between P2 and O2, the material experiences large strain that results in crack nucleation and growth upon further cycling (Figure 2d).^[27] Similarly, the phase transitions occurring in O3-phase during charging also lead to large volume variations. Yu et al. investigated the phase transition that is responsible for the lattice strain. Via in-situ x-ray diffraction (XRD) analysis, the calculated volume variation as a function of charge voltage revealed a large volume drop during the hexagonal P3' → hexagonal O'3 transition, corresponding to a charge voltage of 3.58 V to 4.0 V (Figure 2e). The Cross sectional secondary electron microscopy (SEM) images of the cycled material confirmed the existence of large strain in the material due to the volume drop, as the extend of cracks intensified when charged to 4.0 V compared to that of 3.58 V (Figure 2f).^[25]

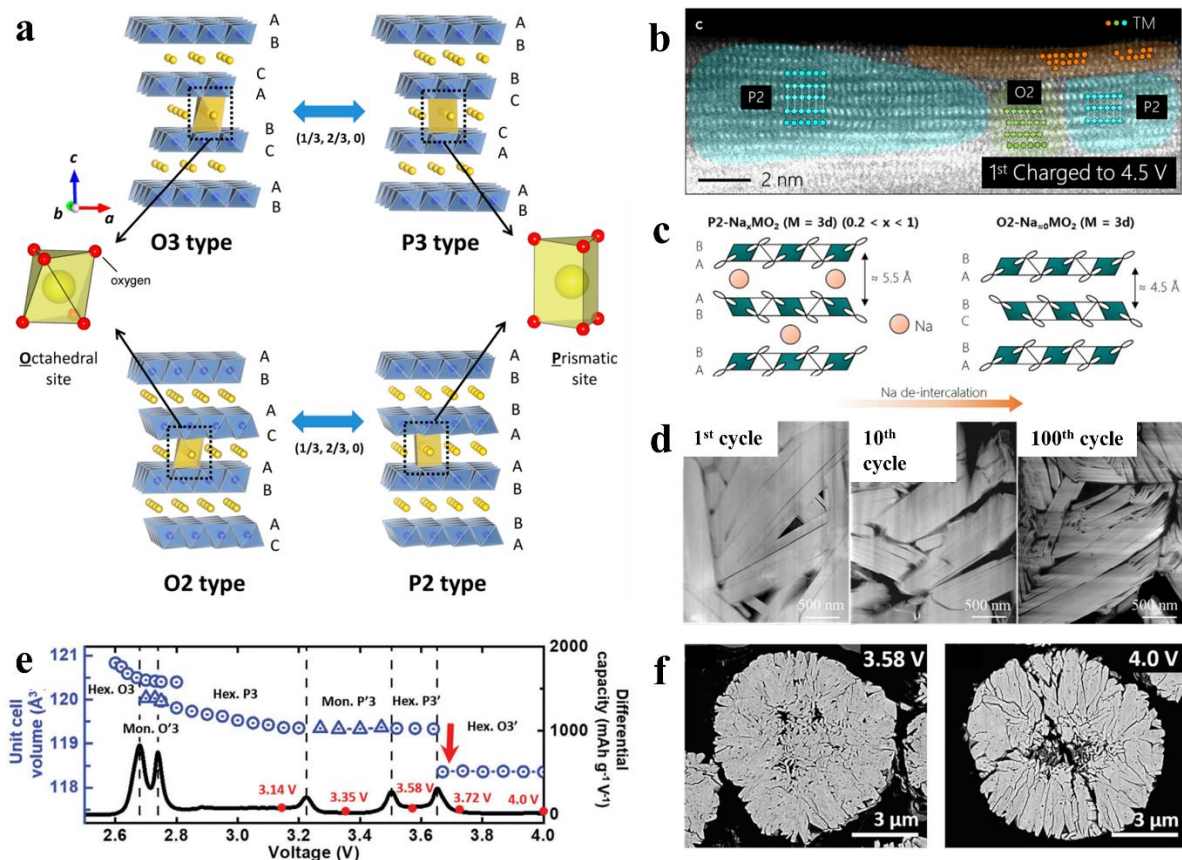


Figure 2. a) Schematic illustration of the O3 and P2 phase transition upon de/intercalation of Na⁺. Reproduced with permission.[12] b) ABF STEM showing intergrown P2 and O2-phase. c) schematic illustration of structural collapse due to extraction of Na⁺ in P2-phase. Reproduced with permission. [26] d) STEM showing the growth of cracks with cycling. Reproduced with permission.[27] e) unit cell volume variation as a function of charging voltage. f) Cross sectional SEM images of cycled electrode when charged to 3.58 V and 4.0 V. Reproduced with permission.[25]

Several studies have reported on the potential dissolution of Mn in Na_xMn_yTM_{1-y}O₂ cathodes, which contributes to their surface instability. This dissolution is thought to be caused by the disproportionation reaction of Mn³⁺ leading to the formation of Mn²⁺. The dissolved Mn²⁺ ions can deposit on the anode, altering the composition of SEI, which in turn increases the resistance for Na⁺ to pass through.[28] Additionally, it has been observed that the use of NaPF₆ as an electrolyte salt can cause the dissolution of TM due to the formation of hydrogen fluoride (HF) during cycling. The formation of HF is a result

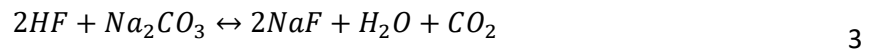
of the reaction between PF_5 , a decomposition product of $NaPF_6$, and H_2O . This can lead to the degradation of the active material, negatively impacting the overall performance of the SIBs. Specifically, HF are formed according to the following^[29]:



Operating the cathode at high voltage (~ 3.6 V) decomposes the electrolyte and favors the formation of HF. The by-products of the decomposition react with the cathode, forming a layer of substance around the electrode called the cathode-electrolyte interphase (CEI), which continuously grows upon further cycling. The CEI can hinder the transport of Na^+ , thus decreasing the rate capability of the cathode.^[28,30]

$NaClO_4$ is another popular salt used in SIB, and unlike $NaPF_6$, it is not subjected to forming reactive F species. However, it is important to note that the binder commonly used in SIBs, polyvinylidene fluoride (PVDF), has been reported to generate F species. Furthermore, recent studies show that Na^+ and PF_6^- exhibit weak interaction that promotes Na^+ desolvation and thus improve the kinetics of Na^+ intercalation.^[31] Therefore, $NaPF_6$ may be more preferable as $NaClO_4$ has been shown to be an explosive hazard that raises safety concerns.^[32]

Sodium hydroxide ($NaOH$) and sodium carbonate (Na_2CO_3) are commonly found surface residual as sodiated transition metal oxide are reactive with CO_2 and water.^[33] However, the presence of $NaOH$ and Na_2CO_3 as insulating layers can hinder electronic conduction and lead to decreased capacity and increased cell polarization. Furthermore, Na_2CO_3 can react with HF, exacerbating the deterioration of the electrode with more H_2O formation:^[29]



In addition to the growth of CEI that impacts the rate performance of cathode, another factor that affects Na^+ diffusion is the Na^+ /vacancy ordering. This ordering causes a reduction in the dimensionality of the diffusion pathway, which results in slower diffusion rates.^[34] Interestingly, recent studies have reported that the occurrence of Na^+ /vacancy ordering depends on the configuration of TM layer. Specifically, Na^+ /vacancy ordering occurs more frequently when the redox potential between the TM species is similar, as this creates an environment that is more conducive to the formation of ordered structures.^[35]

The Jahn-Teller effect frequently causes a phase transition in materials containing Jahn-Teller active transition metals such as Ni^{3+} and Mn^{3+} . In a pristine cathode, $\text{Mn}^{3+}/\text{Mn}^{4+}$ coexist in the lattice, and their redox couple occurs below 2 V vs. Na/Na^+ . Upon discharging to below 2 V, a distorted lattice can be detected with XRD analysis. This distortion is unfavorable, as it is associated with poor rate capability and severe capacity decay. The exact degradation mechanism behind Jahn-Teller distortion is not yet fully understood, but it is believed to impose significant strain on the structure, leading to structural defects and amorphization.^[36]

Figure 3 presents an overview of the degradation process of a $\text{Na}_x\text{Mn}_y\text{TM}_{1-y}\text{O}_2$ electrode. Initially, phase transitions occur due to the gliding of the TMO_2 layer, causing a significant decrease in volume and structural collapse. Coupled with the Jahn-Teller distortion that causes structural defects and amorphization, cracks are nucleated. In the presence of reactive species like HF in the electrolyte, the active material, including Mn^{2+} , can dissolve, contributing to the propagation of cracks. Thereafter, more surface area becomes exposed, creating an ideal environment to accelerate crack propagation and CEI formation. Consequently, cycled cathode material shows poor structural integrity and is coated by a thick layer of CEI.

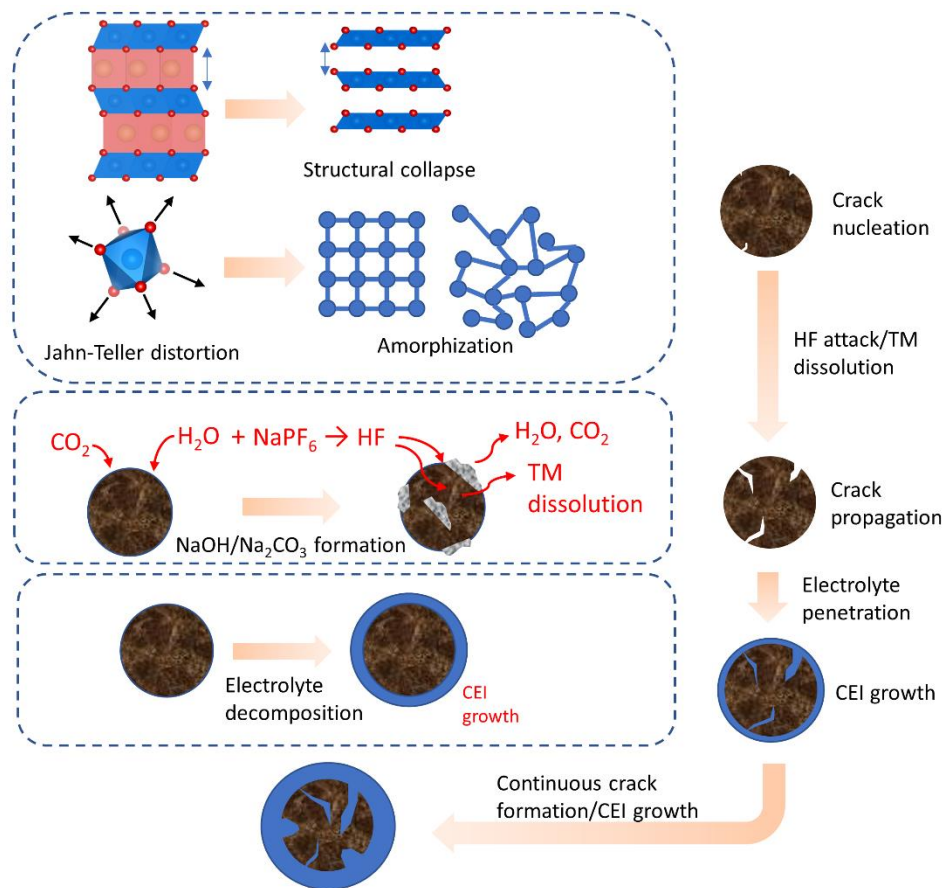


Figure 3. Schematic illustration of material degradation in $\text{Na}_x\text{MnyTM}_{1-y}\text{O}_2$

Chapter 3 Literature Review on Modification Strategies

A plethora of strategies have been extensively investigated to enhance the performance of $\text{Na}_x\text{Mn}_y\text{TM}_{1-y}\text{O}_2$ cathode in SIBs. In this regard, the most commonly reported approaches can be categorized into three distinct categories, namely doping, coating, and heterostructure design. The present section offers a comprehensive summary of these strategies, highlighting their individual merits.

3.1 Doping

Doping is one of the most reported strategies in overcoming some of the predicaments that exists in $\text{Na}_x\text{Mn}_y\text{TM}_{1-y}\text{O}_2$ through the change of bond strength and local electronic environment achieved by introducing a foreign species into the lattice. Doping can be generally categorized as TM layer doping and AM layer doping. Various improvements have been demonstrated, but the main effects are summarized as: 1) enhancing stability, and 2) improving electrochemical performance of the material.

Enhancing stability. Cu^{2+} [37–45], Al^{3+} [36,46–50], Li^+ [26,51–59], Mg^{2+} [60–65], K^+ [66,67], and Ti^{4+} [68–71] have demonstrated their success in enhancing the structural stability of $\text{Na}_x\text{Mn}_y\text{TM}_{1-y}\text{O}_2$. Currently, the structural instability stems from the Jahn-Teller distortion due to presence of Mn^{3+} , and irreversible TMO_2 layer gliding that causes structural collapse. Typically, the mechanism for mitigating Jahn-Teller distortion has been described as the increased ratio of $\text{Mn}^{4+}/\text{Mn}^{3+}$ upon doping, thereby reducing the amount of Jahn-Teller active Mn^{3+} . For instance, Wang et al. revealed via XPS that the ratio of $\text{Mn}^{4+}/\text{Mn}^{3+}$ increases from 0.59 to 0.91 in a Cu-doped material.^[40]

The effects of doping in mitigating structural collapse are more diverse and depend on the phase of the material. In P2 phase, the most intuitive method is to suppress the gliding altogether, and it can be achieved when doping into the AM layer that allows the dopants to act as “pillars”. The effects of “pillar” stabilization have been demonstrated using K^+ [66,67], Mg^{2+} [72–75], Ca^{2+} [58], and Zn^{2+} [76], where the gliding of TMO_2 layer have been hindered, giving rise to extended cycling performance.

The suppression of TMO_2 layer gliding can also be achieved by doping into the TM layer, though many reports ascribed the suppression to the reinforced TM layer due to stronger dopant-O bond without further explanation. In P2 Li-doped materials, Yang et al. reported a formation of Li/Mn superstructure in the TM layer upon Li substitution, and demonstrated the suppression of P2-O2 transition thanks to the superstructure acting as a large defect that pins TMO_2 layer from gliding.^[51,52] At the same time,

some studies indicate that in the presence of Li^+ , more Na^+ is retained in the structure during deep charge state to screen the electrostatic repulsion between the TMO_2 layer, thereby hindering the gliding.^[53,54,54,55] Interestingly, the activation of oxygen redox has been shown to hinder the gliding by reducing the electrostatic repulsion between the adjacent TMO_2 slabs.^[49] In O3-type material, the effort of doping has been mainly concerned with improving the reversibility of gliding by reducing the lattice contraction.^[71,77]

Improving electrochemical performance. Several strategies have been proposed to improve the electrochemical performance of $\text{Na}_x\text{Mn}_y\text{TM}_{1-y}\text{O}_2$. One approach is the disruption of Na^+ /vacancy ordering, which can be achieved by doping with elements such as Li^+ , Cu^{2+} , Al^{3+} , Mg^{2+} , Ti^{4+} , Sn^{4+} , and Zn^{2+} . The mechanism of the Na^+ /vacancy disordering can be generalized as restricted electron delocalization that destroys the superstructure formation in the TM layer.^[59,71,78]

Elevating the operating voltage is another strategy, and elements such as Sn^{4+} ^[24,78–81] and Ti^{4+} ^[28,82] have been shown to effectively raise the voltage of the material. The effects are more prominent with $\text{Ni}^{2+}/\text{Ni}^{4+}$ redox couple, where the lack of d-orbital and O-2p hybridization results in higher electronic density on O. Consequently, energy difference between Ni-3d and O-2p increases which results in high redox potential.^[24,83] Co-doping Zn and Cu has also been shown to increase the voltage through a similar mechanism.

The utilization of oxygen redox ($\text{O}^{2-}/\text{O}^{\cdot-}$, typically occurs at above 4 V) for charge compensation can potentially elevate the operating voltage, as well as providing additional charge storage capability that overall increases the energy density of $\text{Na}_x\text{Mn}_y\text{TM}_{1-y}\text{O}_2$. In LIB, the mechanism of oxygen redox in Li-rich layered oxide has been ascribed to the $\text{Li}^+\text{-O-Li}^+$ interaction. Such AM-O-AM configuration can be achieved in Na-deficient oxide by doping excess Mg^{2+} into the system, thus achieving dual effects of increasing energy density and improving structural stability.^[74,75] More recently, it has been shown that the AM-O-AM configuration in Na-deficient oxide is not a necessary condition for activating the oxygen redox reaction.^[65,84–88] Dopants such as Li, Mg, and Zn can trigger oxygen redox, although some studies demonstrate that other dopants such as Al and Cu can also trigger oxygen redox.

The utilization of oxygen redox provides additional capacity, but its current state is not completely reversible, resulting in rapid voltage and capacity fading related to irreversible oxygen release from the lattice. The released oxygen can also accelerate electrolyte decomposition that results in thick CEI in the cycled cathodes. House et al. revealed that the origin of O loss was largely contributed by under

coordinated oxygen (coordination number below 3) caused by driving the electrode to high degrees of alkali-ion deficiency. That is, high extraction of Na^+ can cause oxygen loss, thus limiting the reversible capacity of layered TMO in SIB.^[89] It should be noted that this contrasts the O-loss mechanism observed in Li-rich compounds such as $\text{Li}[\text{Li}_{0.2}\text{Ni}_{0.2}\text{Mn}_{0.6}]$, where the migration and extraction of Li trigger irreversible oxygen loss. Oxygen loss can cause material degradation and raise safety concerns. Avoid charging the material to above 4 V can suppress oxygen release, but largely impede the available capacity of the material. Therefore, irreversible oxygen redox also poses a challenge in $\text{Na}_x\text{Mn}_y\text{TM}_{1-y}\text{O}_2$. Fortunately, some recent research shows that oxygen redox can be improved via multiple-doping and topology design.

3.1.1 Single doping

Li⁺/Mg²⁺/Zn²⁺ doping. The use of Li^+ , Mg^{2+} and Zn^{2+} as dopants have been shown to stabilize the structure of material. In recent years, they have garnered significant attention due to their ability to facilitate oxygen redox to increase the energy density of the material.

Wang et al. conducted a study to synthesize a $\text{P2-Na}_{0.7}\text{Mg}_{0.05}[\text{Mn}_{0.6}\text{Ni}_{0.2}\text{Mg}_{0.15}]\text{O}_2$ by doping excess Mg^{2+} into the material, which allowed for simultaneous doping into both the AM and TM layers (Figure 4a). The Mg-O-Mg mimicked the Li-O-Li configuration in Li-rich material, and could facilitate the oxygen redox.^[74] Moreover, presence of Mg in the AM layer could serve as a “pillar”, thus enhancing the structural stability of the material.^[72,73] In situ XRD revealed that P2-O2 phase was suppressed owing to the stabilization effect of Mg “pillars”. From the cycling test, the modified electrode retained 79% of initial capacity after 1000 cycles between 1.5 – 4.2 V at 170 mA g^{-1} .^[74]

The oxygen redox reaction in $\text{Na}_x\text{Mn}_y\text{TM}_{1-y}\text{O}_2$ does not necessarily require an AM-O-AM configuration.^[65,84–88] Yabuuchi et al. first discovered a $\text{P2-Na}_{2/3}\text{Mg}_{0.28}\text{Mn}_{0.72}\text{O}_2$ material that exhibited an unusually high first-cycle discharge capacity of 220 mAh g^{-1} , suggesting the presence of oxygen redox.^[65] Subsequently, Bruce and coworkers experimentally verified the oxygen redox activity in this material, and their density of states (DOS) calculation using density functional theory (DFT) revealed that the Mg-3s and O-2p interaction formed weak ionic Mg-O bonds, which put O 2p states near the top of the valence band.^[84] Furthermore, the same group investigated the cause of voltage fading and presented a mechanism for oxygen redox in $\text{P2-Na}_{2/3}\text{Mg}_{0.28}\text{Mn}_{0.72}\text{O}_2$ (Figure 4b). The material originally exhibited a honeycomb ordering in the TM layer. Upon charging, Mg^{2+} migrated into the AM layer and formed cation-vacancy clusters that trapped O_2 . The following discharge repopulated Mg^{2+} in the TM

layer, and Mn/Mg honeycomb ordering was partially (70%) reformed. However, upon further cycling, honeycomb ordering was completely lost, corresponding to the loss of the charging plateau seen in the first cycle.^[86] Following this trend, other Mg-doped materials with a different stoichiometry have been reported. Dai et al. reported a P2-Na_{2/3}Mg_{1/3}Mn_{2/3}O₂ with strong oxygen redox, delivering a high first-cycle discharge capacity of 162 mAh g⁻¹, and 79% capacity retention at 1C after 100 cycles. They proposed a more reliable method for direct quantification of oxygen and Mn²⁺/Mn³⁺ redox through mapping of resonant inelastic X-ray scattering (mRIXS)^[90], which can resolve the energy of fluorescence photon that is missing in the traditional X-ray absorption spectroscopy (XAS). This overcame the technical limitations with soft X-ray O-K studies of X-ray photoelectron spectroscopy (XPS) and XAS such as low probe depths and TM-O hybridization in XAS. To quantify the cyclability of oxygen redox, the authors extracted super-partial fluorescence yield (sPFY) spectra by integrating the characteristic 523.7 eV emission-energy range, where the amount of oxygen redox could be calculated by the sPFY 531 eV peak intensity difference. The analyzed result revealed that the material exhibited reversible lattice oxygen redox over 100 cycles with 87% oxygen redox retained.^[85]

Substituting Mn with Li, Tarascon and colleagues synthesized an O3-NaLi_{1/3}Mn_{2/3}O₂ with a high reversible capacity of 190 mAh g⁻¹ owing to the facilitated oxygen redox.^[91] Similarly, Rong et al. reported a P2-Na_{0.72}[Li_{0.24}Mn_{0.76}]O₂, and demonstrated a very high initial discharge capacity of 270 mAh g⁻¹ between 1.5 – 4.5 V, and 200 mAh g⁻¹ between 2.0 – 4.5 V (Figure 4c). Interestingly, XRD analysis revealed that P2-O2 transition was not detected, even with high degree of Na⁺ extraction. The authors described the suppression mechanism of P2-O2 as decreased in negative charge upon the oxidation of O²⁻, which weakened the repulsion between the adjacent oxygen layers. As a result, the average repulsion between the O-2p orbitals became smaller compared with the activation energy required to make the TMO₂ slab glide, giving rise to a superior structural stability.^[26]

A few studies demonstrated charge compensation with oxygen redox in Zn-doped Na_xMn_yTM_{1-y}O₂ materials that delivered high capacities. For instance, a P2-Na_{2/3}Mn_{7/9}Zn_{2/9}O₂ with 200 mAh g⁻¹ in 1.5 – 4.2 V^[92], a P2-Na_{2/3}Zn_{1/4}Mn_{3/4}O₂ with 202.4 mAh g⁻¹ in 1.5 – 4.5 V^[93], and a P3-Na_{0.67}Mn_{0.9}Zn_{0.1}O₂ with 165 mAh g⁻¹ in 1.8 – 4.3 V^[94]. Though doping with Zn²⁺ can inhibit TMO₂ layer gliding^[93], the low reversibility of oxygen redox causes subpart cycling performance in these materials.

The low reversibility of oxygen redox has been a cause of concern due to oxygen evolution. It is well documented that these dopants can migrate to the AM layer into the Na⁺ vacancy sites at deep charge

state, and semi-reversibly repopulate the TM layer in the following discharge cycle. However, the low reversibility of dopants shuttling between TM and AM layer weakens and destroys the oxygen framework, leading to voltage and capacity fading. While the presence of Ni and Fe in the TM layer can suppress Li migration^[52,95,96], some reported the necessity of dopants migration in triggering oxygen redox^[97].

Recently, the topological features of the TM layer in Li-doped materials have been linked to the behavior of Li migration and repopulation, and hence the stability of oxygen redox. House et al. compared a P2-Na_{0.75}[Li_{0.25}Mn_{0.75}]O₂ with honeycomb ordering and a P2-Na_{0.6}[Li_{0.2}Mn_{0.8}]O₂ with ribbon ordering (Figure 4d). ⁶Li magic-angle-spinning (MAS) nuclear magnetic resonance (NMR) analysis showed that Li⁺ migrated into the AM layer and repopulated the TM layer in the following discharge. However, significant broadening of the peak around 1800 rpm in honeycomb-ordered material corresponded to the loss of superstructure upon Li⁺ repopulation. In contrast, the result of ribbon-ordered material did not change. Due to the maintained superlattice, ribbon ordering provided better framework stabilization for oxygen redox, thus exhibiting a lower voltage hysteresis.^[98] Gao et al. demonstrated that P3-Na_{0.6}Li_{0.2}Mn_{0.8}O₂ showed higher oxygen redox reversibility compared to its P2 counterpart (Figure 4e). The improvement was ascribed to the topological difference where P3 exhibited an α - γ TMO₂ layer stacking that was better for Li to reversibly migrate/repopulate compared to the α - β stacking of P2.^[99,100]

These topological designs in improving oxygen redox sparked similar investigation in Mg-doped material.^[87,88] For example, Zhao et al. found that while the P2 and P3 phases of Na_{2/3}Mg_{1/3}Mn_{2/3}O₂ have very similar crystal structures, the P3-phase could only maintain 41.5% capacity retention after 100 cycles, in contrast to minimal capacity fading in P2-phase. ²³Na MAS NMR and synchrotron XRD analysis showed an irreversible P3-O3 structural evolution during oxygen redox, while P2 demonstrated reversible local structural recovery. Moreover, DFT calculations indicated that Mg displacement is kinetically favorable in the P3 and O3 phases. Together, the author proposed that the low oxygen redox stability of the P3 phase was attributed to the substantial Mg displacement during deep charge, which disrupted the electronic structure and destabilized the oxygen framework.^[88]

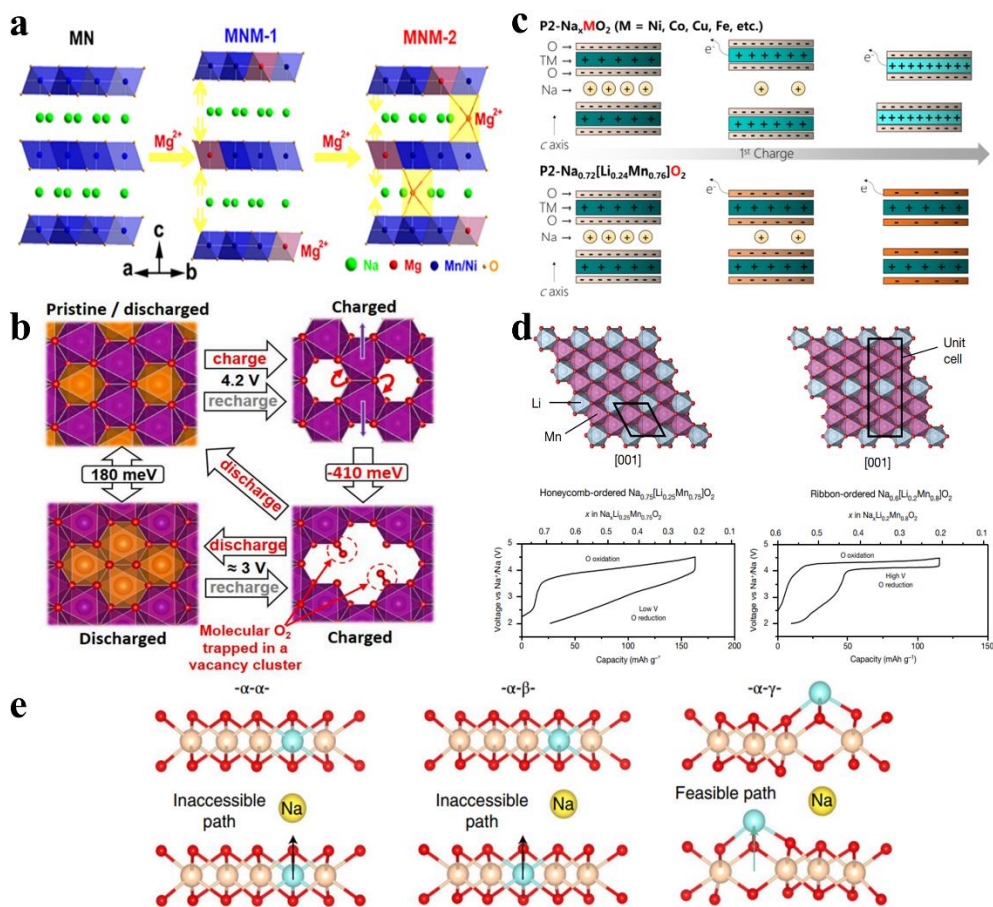


Figure 4. a) evolution of Mg^{2+} doping site with increasing Mg^{2+} concentration. Reproduced with permission.[74] b) schematic of oxygen redox mechanism showing cation-vacancy clusters and loss of honeycomb ordering. Reproduced with permission.[86] c) proposed P2-O₂ suppression mechanism due to oxygen redox. Reproduced with permission.[26] d) superstructure schematic and 1st cycle charge-discharge curve of honeycomb-ordered $Na_{0.75}[Li_{0.25}Mn_{0.75}]O_2$ and ribbon-ordered $Na_{0.6}[Li_{0.2}Mn_{0.8}]O_2$. Reproduced with permission.[98] e) schematics of α - α , α - β , and α - γ stackings. Reproduced with permission.[99]

Cu²⁺/Al³⁺ doping. The incorporations of inexpensive Cu^{2+} has emerged as a viable strategy for improving $Na_xMn_yTM_{1-y}O_2$, as it can enhance structural^[37-45] and surface stability^[40], disrupt Na^+ /vacancy ordering and improve rate capability.^[38,45] For example, Chen et al. synthesized a P2- $Na_{0.44}Mn_{0.6}Ni_{0.3}Cu_{0.1}O_2$, which exhibited a reversible capacity of 149 mAh g⁻¹ at 170 mA g⁻¹ and retained 81% of its initial capacity after 50 cycles.^[45] Lei Wang et al. studied P2- $Na_{0.67}Ni_{0.3-x}Cu_xMn_{0.7}O_2$ cathodes with different level of Cu^{2+} doping ($x = 0, 0.1, 0.2, 0.3$). In situ XRD revealed that the P2-O₂

transition was suppressed in Cu-doped samples even when cycled between 2.0 – 4.5V, giving rise to its structural stability. The ex-situ XRD analysis demonstrated that Na⁺/vacancy ordered structure was absent from Cu-doped sample, which promoted the rate performance of Cu-doped electrodes. Consequently, electrochemical testing of optimized Cu-doped electrode (i.e., x=0.2), though at a sacrificed of minor capacity reduction, displayed an improved cycling and rate performance when compared to non-doped electrode.^[44] Jianyin Wang et al. conducted sXAS analysis and concluded that Cu-doping reduced the surface content of Mn²⁺ that was associated with the dissolution of Mn in the material.^[40] It should be noted that Cu²⁺ is an electrochemically inactive dopant, substitution with Cu²⁺ inevitably reduces reversible capacity of the cathode material, though some recent research reported active Cu²⁺/Cu³⁺ redox couple that could provide additional capacity^[39,41,101,102].

The effects of Al-doping are similar to that of Cu according to the previous studies.^[36,46–50,103,104] A noteworthy example is the reported oxygen redox activity triggered by the presence of Al³⁺. Cheng et al. reported an Al-doped P2-Na_{0.6}Ni_{0.3}Mn_{0.7}O₂ with suppressed P2-O2 transition. XAS analysis with different probe depth elucidated the evolution of Ni oxidation state during the charge/discharge process. As expected, the Ni oxidation state increased when charged from open circuit voltage (OCV) to 4.35 V, but an inverse behavior where Ni was reduced upon charging from 4.35 V to 4.5 V was also observed. Integrated intensities of O K-edge pre-edge feature revealed the presence of oxygen redox activities, and the evolution of O oxidation state followed a similar trend to that of Ni. As such, the authors proposed an Al-induced reductive coupling mechanism (RCM) that suppressed the P2-O2 transition. Specifically, the electrons produced from the oxidation of oxygen flowed to an adjacent Ni to partially reduce it. The reduced electrostatic repulsion between the TMO₂ due to oxygen oxidation prevented the gliding of TMO₂ layer, enhancing the material structural stability and cyclability.^[49]

K⁺ doping. Previously, incorporating dopants such as Mg²⁺ into the AM layer to act as “pillars” have demonstrated the effectiveness in stabilizing the structure of the material. The idea of the “pillar” stabilization has been extended with K⁺ doping. Chenchen Wang et al. reported a P2-Na_{0.612}K_{0.056}MnO₂ with a reversible capacity of 240.5 mAh g⁻¹ at 20 mA g⁻¹ between 1.8 – 4.3 V, corresponding to 0.901 Na⁺ per formula of de/intercalation without P2-O2 transition. Moreover, its cycling test at 50 mA g⁻¹ showed a capacity retention of 98.2 % after 100 cycles. Via DFT, the mean square displacements (MSDs) analysis showed that K⁺ was riveted between layers without impeding the diffusion of Na⁺. The DOS calculation for the K-doped material showed an increase in spin-down electrons near the Fermi level, suggesting a stronger Mn and O hybridization. Moreover, crystal orbital Hamilton

populations (COHP) analysis revealed reinforced Mn-O bonds for both adjacent and distant Mn. Such reinforcement was believed to contribute to the suppression of P2-O2 transition, giving rise to a better structural stability and higher reversible capacity.^[66]

In a different approach of achieving K-pillar, Yuesheng Wang et al. investigated the electrochemical performance of a series of $K_x[Ni_{x/2}Mn_{1-x/2}]O_2$ ($x = 0.1, 0.2, 0.3, 0.4, 0.5, 0.6, 0.67$) layered structure. Interestingly, the charge-discharge curves showed that higher discharge capacities were attained in the second cycle, of which the $x=0.4$ compound stands out. This could be understood as partial replacement of K^+ with Na^+ via cation-exchange and electrochemical intercalation. Inductively coupled plasma (ICP) results showed the extraction of K^+ ions in the first discharge/charge cycle, and the total K^+ content was stabilized at 0.08 compared to 0.4 initially, suggesting the formation of $P2-Na_{0.74}K_{0.08}[Ni_{0.2}Mn_{0.8}]O_2$. The material exhibited a delayed P2-O2 transition disclosed by in-situ XRD. Via ab initio molecular dynamics (AIMD) simulation, the diffusion of Na^+ and K^+ show an overlap of trajectory, which indicated that the presence of K^+ in the AM layer did not hinder Na^+ diffusion. K-K radial distribution function (RDF) found that localization of K^+ led to a homogeneously distributed “pillars”, explaining the stabilization effect of only 8% of K^+ in the material. When cycled between 1.5 – 4.0 V, the as-formed $P2-Na_{0.74}K_{0.08}[Ni_{0.2}Mn_{0.8}]O_2$ compound could deliver a remarkably high capacities of 194 mAh g^{-1} at 0.1 C and 135 mAh g^{-1} at 4 C. Furthermore, it could retain 86% of the initial capacity (163 mAh g^{-1}) after 500 cycles at 1 C.^[67]

Sn⁴⁺/Ti⁴⁺ doping. Sn^{4+} and Ti^{4+} are commonly reported to disrupt Na^+ /vacancy ordering, promote voltage of active redox couple, and enhance structural stability. With these effects, Sn^{4+}/Ti^{4+} doping can improve cyclability, rate capabilities, and energy density of $Na_xMn_yTM_{1-y}O_2$.^[24,78–81] For instance, Song et al. reported a higher average voltage of 3.2 V in a 8%Sn-modified O3- $NaNi_{1/3}Fe_{1/3}Mn_{1/3}O_2$ with 81% capacity retention after 200 cycles owing to the improved structural stability.^[81]

While similar, recent research suggests that doping with Ti^{4+} seems to be more effective in improving the material’s rate capabilities. Wang et al. reported an O3- $NaNi_{0.5}Mn_{0.2}Ti_{0.3}O_2$ with 85% capacity retention after 200 cycles because of enhanced reversibility of O3-P3 phase transition.^[105] The same group demonstrated that superb rate performance could be achieved in a $P2-Na_{2/3}Ni_{1/3}Mn_{1/3}Ti_{1/3}O_2$, delivering about 70 mAh g^{-1} at 3460 mA g^{-1} (20 C) compared to near 0 mAh g^{-1} in the unmodified cathode. In addition, the Ti-doped material also retained 83.9% of the initial capacity after 500 cycles. Molecular dynamics (MD) simulation showed a 2D interconnected diffusion path of Na^+ , which

enhanced the Na⁺ mobility. The authors proposed that the excellent rate performance was due to the restricted electron delocalization upon Ti-substitution, effectively disrupting Na⁺/vacancy ordering, while enhanced cyclability was due to suppressed phase transition.^[69,71]

3.1.2 Multiple doping

As discussed, the effect of doping can largely improve the performance and stability of the Na_xMn_yTM_{1-y}O₂. Incorporation of more than one species can have synergistic effects.

In particular, co-doping of Cu and Mg can further improve the structural stability of the material^[42,60,106] and enhance the reversibility of oxygen redox.^[106–108] Kong et al. reported a dual doped Cu/Mg P2-Na_{0.67}Mn_{0.71}Ni_{0.25}Cu_{0.02}Mg_{0.02}O₂ for synergistic improvement on reversible anionic redox. They demonstrated that Cu and Mg doping can increase the ratio of lattice oxygen/surface oxygen, leading to a more reversible anionic redox as surface oxygen is associated with oxygen evolution. This was attributed to the enhanced TM-O bonding energy upon Cu doping. The dual doped electrode outperformed the bare electrode, delivering 162 mAh g⁻¹ at 0.05 C, 147 mAh g⁻¹ at 0.1 C with 86% retention after 100 cycles, and 124 mAh g⁻¹ at 1 C with a capacity retention of 81.9% after 100 cycles.^[107] Similarly, Cheng et al. demonstrated that lattice oxygen reversibility increased from 95% to 73% in a P2-Na_{0.6}Mg_{0.15}Mn_{0.7}Cu_{0.15}O₂ due to the overlap of Cu-3d and O-2p that reinforced the oxygen framework. This extended the capacity retention from 35.4 to 95.8% after 200 cycles.^[106] DFT calculations revealed that Cu could present a large area of electron delocalization that promoted the formation of abundant nonbonding oxygen, increasing the involvement of lattice oxygen that is responsible for reversible oxygen redox.^[108]

Various attempts have been made to improve the performance of Li-doped materials by introducing additional species. Yoon et al. doped a small amount of Al to prepare a P2-Na_{0.6}Li_{0.195}Al_{0.005}Mn_{0.8}O₂ with an increased utilization of oxygen redox from 59.3% to 74.9%. This effect was ascribed to Al-induced heterogeneous oxygen redox which stabilized the oxide framework upon cycling.^[109] Wang et al. prepared a Mg/Li co-doped Na_{2/3}[Li_{1/7}Mn_{5/14}][Mg_{1/7}Mn_{5/14}]O₂ with a dual-honeycomb ordering superstructure (i.e. [Li_{1/7}Mn_{5/14}] and [Mg_{1/7}Mn_{5/14}]) with improved oxygen redox reversibility (Figure 5a). The dual-honeycomb superstructure allowed for reversible shuttling of Li between the AM and TM layer, with Mg/Mn honeycomb maintaining the superstructure in the TM layer. The material achieved a capacity of 285.9 mAh g⁻¹ at 10 mA g⁻¹ and maintained 85.5% of the initial capacity after 50 cycles at 100 mA g⁻¹. The authors found that the oxidation onset potential in the presence of LiMn₆

was lower than that of MgMn_6 , and theoretical result supported the experimental findings.^[110] Wang et al. reported doping of Ca^{2+} into the AM layer of a $\text{P2-Na}_{0.75}\text{Ca}_{0.05}\text{Li}_{0.15}\text{Fe}_{0.2}\text{Mn}_{0.6}\text{O}_2$. The authors described the 2-fold effect of Ca: 1) Ca could serve as a “pillar” in the lattice to suppress P2-O2 phase transition. 2) Ca formed a stronger Ca-O bond, thus relieving some irreversible oxygen evolution.^[58] Zhang et al. showed that doping of Zn^{2+} into a Li-doped material could suppress Jahn-Teller effect as well as reducing the inherent phase separation. As a result, the $\text{Na}_{0.833}\text{Zn}_{0.0375}\text{Li}_{0.25}\text{Mn}_{0.7125}\text{O}_2$ delivered a capacity of 166 mAh g^{-1} with 97% capacity retention after 200 cycles.^[111]

Zhang et al. investigated the impact of Li/Ti co-doping on Na^+ /vacancy ordering in a $\text{P2-Na}_{7/9}\text{Li}_{1/9}\text{Ni}_{2/9}\text{Mn}_{5/9}\text{Ti}_{1/9}\text{O}_2$. The modified electrode demonstrated excellent rate capability compared to the unmodified electrode. At 15, 75, 150, 300, 750, and 1500 mA g^{-1} , the modified electrode delivered 140, 135, 132, 128, 121, and 113 mAh g^{-1} , respectively. Furthermore, the material demonstrated excellent cycling performance with 90.2% retention rate after 200 cycles at 150 mA g^{-1} . The superior cycling and rate performance suggested lack of phase transition and Na^+ /vacancy ordering upon doping. In situ XRD confirmed the absence of P2-O2 transition, and analysis of galvanostatic intermittent titration technique (GITT) result revealed two orders of magnitude higher Na^+ diffusivity in the modified electrode. DFT calculations revealed that more Na^+ occupied the Na_e site in the doped electrode, which further proved the disruption of Na/vacancy ordering. The calculated migration barrier of modified electrode was lower than that of the unmodified electrode, which was consistent with the excellent rate performance. Consequently, the authors ascribed the disrupted Na^+ /vacancy ordering to the breaking of TM ordering upon Li-doping that induced change in local electronic environment.^[59]

Cheng et al. synthesized a Zn/Cu co-doped $\text{P2-Na}_{0.67}\text{Ni}_{0.21}\text{Mn}_{0.67}\text{Cu}_{0.05}\text{Zn}_{0.07}\text{O}_2$ with suppressed P2-O2 phase transition, disrupted Na^+ /vacancy ordering, and elevated $\text{Ni}^{2+}/\text{Ni}^{4+}$ redox potential. The material delivered capacities of 125, 105, 96, and 84 mAh g^{-1} at current densities of 38, 850, 1700, and 3400 mA g^{-1} . In addition, the material could retained 91% capacity after 100 cycles, showcasing the superior structural stability owing to Zn/Cu co-doping.^[38]

HEO. Recently, the concept of high entropy has attracted vast interest in energy storage due to their ability to improve the performance and stability of the active material. In particular, the constructions of Mn-based high entropy oxide (HEO) have been revolved around doping a higher number of elements to increase its configurational entropy. Specifically, it is related to the mole fractions, x_i and x_j , in the cation and anion sites^[112]:

$$S_{config} = -R \left\{ \left[\sum_{i=1}^N x_i \ln(x_i) \right]_{cation} + \left[\sum_{i=1}^N x_i \ln(x_i) \right]_{anion} \right\} \quad 4$$

Therefore, reported HEO materials typically contain five or more species in the TM layer.

Yao et al. successfully synthesized an O3-NaNi_{0.25}Mg_{0.05}Cu_{0.1}Fe_{0.2}Mn_{0.2}Ti_{0.1}Sn_{0.1}O₂ with improved structural stability and activated oxygen redox, the material delivered 171.2 mAh g⁻¹ at 1 C, and extended cycling stability with 89.3% capacity retention at 1 C for 90 cycles (Figure 5b). The structural evolution analysis of the material revealed an early O3-P3 transition as well as suppressed P3-O3 transition at high-voltage region, suggesting that most of the capacity was stored in P3-phase that was favorable for high rate applications.^[113] Du et al. reported an O3-NaNi_{0.1}Mn_{0.15}Co_{0.2}Cu_{0.1}Fe_{0.1}Li_{0.1}Ti_{0.15}Sn_{0.1}O₂ with superior cycling stability at 160 mA g⁻¹, retaining 82.7% of the initial capacity after 1000 cycles. Though the highest reversible capacity was only 115 mAh g⁻¹, it had a comparatively higher operating voltage of 3.15 V.^[114]

Though these materials exhibited improved performance, the utilization of Co could limit their practical application. Ding et al. reported an O3- NaNi_{0.25}Mg_{0.05}Cu_{0.1}Fe_{0.2}Mn_{0.2}Ti_{0.1}Sn_{0.1}O₂ with a strengthened TMO₂ skeleton that suppressed TM dissolution, cracking, and Jahn-Teller distortion. The material delivered 130.8 mAh g⁻¹ at 14 mA g⁻¹ when operated between 2 – 4 V and retained 75% of initial capacity after 500 cycles at 140 mA g⁻¹. Interestingly, this high configuration entropy material also exhibited a higher portion of {010} active facet that is favorable for Na⁺ intercalation/extraction. Coupled with the disrupted Na⁺/vacancy ordering, the material delivered 108 mAh g⁻¹ at 700 mA g⁻¹.^[115] Fu et al. also reported a HEO with high percentage of {010} active facet, namely P2-Na_{0.62}Mn_{0.67}Ni_{0.23}Cu_{0.05}Mg_{0.09-2y}Ti_yO₂ (Figure 5c, d). The authors compared the percentage of {010} facet on three HEO with different configuration entropy as well as a low entropy NaMnNiO₂. It was determined that high configuration entropy could facilitate the anisotropy growth of the crystal as all the HEO material had at least 40% of {010} facet. With the high entropy stabilization effect and activation of anionic redox, the material output 148 mAh g⁻¹ at 12 mA g⁻¹, and retained 87% of capacity after 500 cycles at 120 mA g⁻¹, and 75% after 2000 cycles at 1200 mA g⁻¹.^[116]

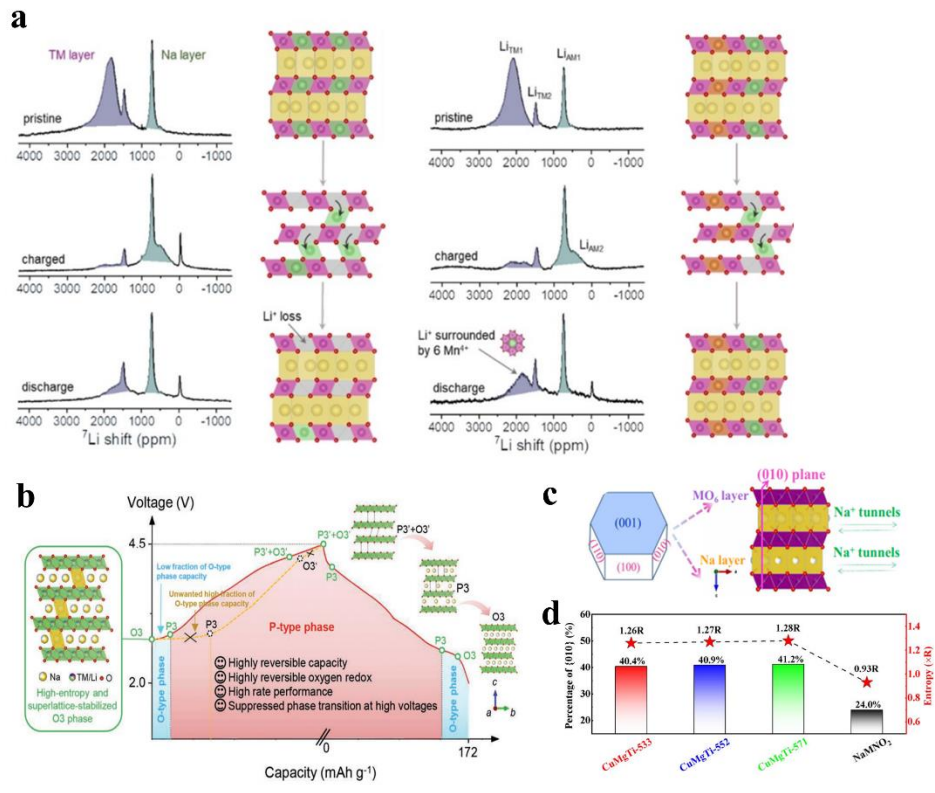


Figure 5. a) ^7Li NMR spectra at different stage of first charge/discharge cycle of samples with single honeycomb (LiMn_6 , left) and dual honeycomb ($\text{LiMn}_6\text{-MgMn}_6$, right) showing a reversible Li shuttling in the dual honeycomb sample. Reproduced with permission.[110] **b)** schematic summarizing the structural evolution of $\text{O}_3\text{-NaNi}_{0.25}\text{Mg}_{0.05}\text{Cu}_{0.1}\text{Fe}_{0.2}\text{Mn}_{0.2}\text{Ti}_{0.1}\text{Sn}_{0.1}\text{O}_2$, showing capacity were mainly stored in P-phase. Reproduced with permission.[113] **c)** schematic illustrations of active facets $\{010\}$ family of planes for Na^+ de/intercalation. **d)** experimentally measured percentage of $\{010\}$ facet in HEO and low entropy (NaMnO_2) materials. Reproduced with permission.[116]

High entropy oxide material has attracted significant attention owing to the stabilization effect. In $\text{Na}_x\text{Mn}_y\text{TM}_{1-y}\text{O}_2$, it typically contains five or more species in the TM layer. Rational selection of dopants can largely improve material performance and stability. Notable examples include $\text{O}_3\text{-NaNi}_{0.25}\text{Mg}_{0.05}\text{Cu}_{0.1}\text{Fe}_{0.2}\text{Mn}_{0.2}\text{Ti}_{0.1}\text{Sn}_{0.1}\text{O}_2$ and $\text{P}_2\text{-Na}_{0.62}\text{Mn}_{0.67}\text{Ni}_{0.23}\text{Cu}_{0.05}\text{Mg}_{0.09-2y}\text{Ti}_y\text{O}_2$ with extended cycling stability and high percentage of active facet (i.e., $\{010\}$ family of planes) for Na^+ de/intercalation.

3.2 Coating

Coating entails applying a thin protective layer onto the surface of $\text{Na}_x\text{Mn}_y\text{TM}_{1-y}\text{O}_2$ electrodes. Metal oxide and polyanion compounds are commonly explored for this purpose, with alternatives like alucone or polymer also proving effective. The primary function of coating is to inhibit direct contact between the electrode and electrolyte, thus minimizing parasitic side reactions.

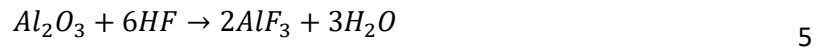
Metal oxide coating. As early as 2000, Al_2O_3 coatings have been reported for LIB^[117], and have remained a growing research topic due to their established ability in improving the stabilities of materials^[118–120]. Due to the similarities between LIB and SIB systems, metal oxide coating is believed to be an effective strategy to improve SIB. In a study conducted by Liu et al, the $\text{P2-Na}_{2/3}\text{Ni}_{1/3}\text{Mn}_{2/3}\text{O}_2$ cathode was coated with Al_2O_3 via wet chemistry, and the effect of coating was evaluated by comparing the coated cathode with a bare cathode. SEM analysis found that the cycled bare material exhibited cracking and exfoliation, due to the large lattice stress caused by 20% volume change during the P2-O2 transition. Consequently, the bare material showed poor cycling performance of 26.8% capacity retention after 300 cycles between 2.5 V to 4.3 V. In contrast, the coated cathode exhibited intact morphology, in accordance with the improved cycling performance. The improvement was ascribed to the external mechanical support that prevented the degradation and exfoliation of material.^[121]

Unlike wet chemistry or mechanical mixing, atomic layer deposition (ALD) can produce coating with precise thickness and high conformality.^[122] Kaliyappan et al. first alluded the importance of Al_2O_3 thickness via ALD.^[123] Building on their work, Alvarado et al. synthesized a $\text{P2-Na}_{2/3}\text{Ni}_{1/3}\text{Mn}_{2/3}\text{O}_2$ coated with 1 nm conformal Al_2O_3 , and analyzed the CEI composition to reveal the protective mechanism of Al_2O_3 . Common electrolyte typically undergoes side-reaction with the electrode material and decomposes. Thus, via XPS analysis, it was discovered that the CEI on the bare electrode contained more organic species such as carbonates, esters, and alkoxyl functionalities that impeded the Na^+ diffusivity. Meanwhile, the CEI on the coated material composed of polymeric species such as poly(ethylene oxide) that resulted in a flexible CEI with better protection against material exfoliation.^[124]

The “HF scavenging” effect of Al_2O_3 was also reported as the protective mechanism against particle exfoliation in SIB. Ji et al. reported an Al_2O_3 coated P2/P3 biphasic $\text{Na}_{2/3}\text{Ni}_{1/3}\text{Mn}_{2/3}\text{O}_2$ and studied the CEI stability. Via XPS, NaF , NiF_2 , and MnF_2 were detected for the bare electrode, which was due to the corrosive HF that attacked and degraded the active material. Comparatively, AlF_3 was found on the

Al₂O₃ coated electrode as a result of the reaction between Al₂O₃ and HF, suggesting elimination of HF. The passivating nature of Al₂O₃ also suppressed the side reactions such as electrolyte oxidation and residual decomposition. Compared with the bare electrode, Al₂O₃ coated electrode showed an absence of CO₂ evolution, proving the effectiveness of coating in suppressing side reactions. Furthermore, ICP analysis disclosed that Al₂O₃ also largely reduced active material dissolution. Consequently, the coated electrode retained 87% capacity after 300 cycles between 1.5 V – 4.1 V, compared to 62% retention for the bare electrode.^[30]

The “HF scavenging” of Al₂O₃ reaction can be described as^[125]:



However, the reaction between Al₂O₃ and HF generates water, which could further react with NaPF₆ to produce HF, and fall into a loop of continuous consumption of Al₂O₃. As such, direct deposit of AlF₃ have been reported to mitigate that issue.^[125,126]

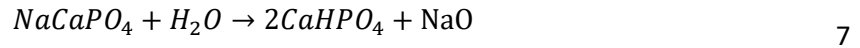
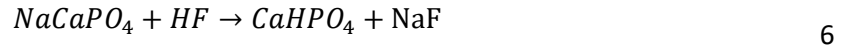
The benefits of Al₂O₃ have inspired explorations into other metal oxides. Kaliyappan and colleagues compared the effect of ultrathin coating of Al₂O₃, ZrO₂, and TiO₂ on a P2-Na_{0.66}Mn_{0.54}Co_{0.13}Ni_{0.13}O₂. Interestingly, it was found that Al₂O₃ improved the cycling stability of electrode, ZrO₂ enabled a better rate capability, while TiO₂ resulted in the worst improvement due to its catalytic activity. The authors attributed the effect ZrO₂ coating to its high toughness, which provided support for the mechanical integrity of electrode during high current cycling.^[127] However, Guo et al. reported a Ti-doped NaMnTi_{0.1}NiO₂ with a reconstructed Ti(III)-concentrated spinel-like oxide layer that improved surface stability and suppress Mn dissolution (Figure 6a). The material could maintain 81% of initial capacity after 500 cycles.^[28] Similarly, Ren et al. described a Zr-doping induced ZrO₂ decoration on a P2 Na-Ni-Mn electrode that showed synergistic improvements (Figure 6b), which can summarized as the following: 1) revealed by XRD analysis, Zr⁴⁺ doping suppressed P2-O2 transition, and maintained quasi-zero strain structure (volume variation 1.18%) which eliminated electrode exfoliation during cycling. 2) via DFT calculation, it was discovered that Zr⁴⁺ doping increased the oxygen vacancy formation energy, thus giving rise to a more reversible anionic redox. 3) through XPS analysis, ZrO₂ coating reduced HF corrosion and electrolyte decomposition. Consequently, the Zr-doped electrode delivered 132 mAh g⁻¹ after 50 cycles when cycled between 2.0 V to 4.5 V, and retained 86% capacity after 1000 cycles between 2.5 V to 4 V.^[128] Zhang et al. reported a simultaneous doping and coating on a P2-Na_{0.66}Ni_{0.33}Mn_{0.67}O₂. Due to more preferentially incorporation of Ni²⁺ into the octahedral sites than

Zn²⁺, doping of Zn²⁺ led to uniform passivation of ZnO on the surface of electrode. The passivating layer of ZnO on the electrode suppressed electrolyte side reaction and decomposition, thus hindering the growth of CEI and performance degradation, as evident by minor increase in R_{CEI} from 250 Ohm (pristine) to 279 Ohm (100th cycle).^[129] Similar dopant segregation-induced coating have been also shown with Al₂O₃ by Al³⁺ doping^[47] and CuO by Cu²⁺ doping^[130].

Binary oxide compounds have been shown to enhance the material performance and stability. For instance, Li et al. reported a P2-Na_{0.67}Mn_{0.5}Fe_{0.5}O₂ coated with Li₂TiO₃ via wet chemistry method which induced co-doping of Li⁺ and Ti⁴⁺ in the material. The incorporation of Li⁺ activated the oxygen redox at high voltage, contributing to higher capacity, while Ti⁴⁺ increased the bonding energy between TM ions and oxygen ions that benefited the reversibility of oxygen redox. Moreover, the Li₂TiO₃ coating restrained the oxygen on the surface and inhibited oxygen loss. Consequently, the material delivered 182 mAh g⁻¹ at 0.1 C and retained 81.3% of the initial capacity after 50 cycles, compared to less than 150 mAh g⁻¹ and 32.1% in the unmodified sample.^[131] Likewise, Xia et al. proposed a synergistic CaTiO₂ surface coating and bulk site-selective Ca/Ti co-doping strategy on a P2-Na_{2/3}Ni_{1/3}Mn_{2/3}O₂ cathode (Figure 6c). The authors proposed that strong dielectric effect of Ca and Ti could create a reverse electric field that prevented oxygen generated in the bulk to migrate to the surface. At the same time, selective doping of Ca²⁺ into the Na site weakened the electrostatic repulsion between the TMO₂ layers, while Ti⁴⁺ doping into the TM layer could enhance the bulk oxygen affinity owing to the strong Ti-O bonding strength. Differential scanning calorimetry (DSC) confirmed the suppression of oxygen evolution to an extent of 90%, and XRD analysis revealed a single-phase charge/discharge process with only 0.99% volume variation. Accordingly, the modified material could retained 75.3% of initial capacity after 200 cycles.^[132]

Polyanions coating. Zhang et al. reported a AlPO₄ coating that induced a small amount of Al³⁺ doping on a P2-N_{0.7}MnO_{2.05}. Owing to the synergetic effect of dual modification, the modified electrode maintained 92.4% capacity for 100 cycles at 1000 mA g⁻¹ current density.^[48] Tang et al. reported an interesting dual modification strategy of NASICON-type NaTi₂(PO₄)₃ coating and Mg substitution on a P2-Na_{0.67}Ni_{0.33}Mn_{0.67}O₂. The coating could facilitate Na⁺ diffusion and prevent HF attack due to its stable and open framework. As a result, the modified cathode exhibited superior rate capabilities and extended cycling performance.^[133]

Jo et al. developed coating method for coating NaPO₃ on a P2-Na_{2/3}Ni_{1/3}Mn_{2/3}O₂ electrode via a heat-assisted reaction of ammonium phosphate and surface residuals (i.e., Na₂CO₃ and NaOH), which formed a thin layer of NaPO₃ on the surface of the cathode. The electrochemical performance of the coated cathode exhibited better cyclability with 80% capacity retention after 50 cycles compared to that of 66% capacity retention of the bare cathode.^[134] Following the method of utilizing surface residuals for coating, the same group also demonstrated coating of NaCaPO₄. The coated cathode retained 43% more capacity after 200 cycles. Electron microscopies showed an intact morphology on the coated cathode, whereas the bare cathode exhibited intense particle exfoliation. Time-of-flight secondary-ion mass spectroscopy (ToF-SIMS) analysis revealed that Na₂POF⁺ and NiF⁺ fragments associated with reaction and formation of HF were noticeably reduced. Meanwhile, CaPOH₂⁺ fragments showed an intense peak in the coated electrode. With that, it was concluded that the improved cycling performance was contributed by HF and water “scavenging” capability of the coating material, thus prevented particle exfoliation and disintegration:^[135]



Other coatings. To further enhance the stability of coating materials beyond Al₂O₃ coating with ALD, molecular layer deposition (MLD) has been explored. One promising material is alucone, which is synthesized by alternating reactions between trimethylaluminum and ethylene glycol or glycerol. Alucone is more electrically conductive, less dense, and more flexible than Al₂O₃, thereby facilitating ion conduction and providing better mechanical support upon volume change. In a study by Kaliyappan et al., alucone was used to coat a P2-Na_{0.66}Mn_{0.9}Mg_{0.1}O₂ electrode, and the electrochemical performance of bare, Al₂O₃-coated, and alucone-coated electrodes were compared (Figure 6d). The alucone-coated electrode outperformed both bare and Al₂O₃-coated electrodes, with 86% capacity retention, initial capacity of 163.1 mA h g⁻¹, and 95.8% ICE at 1 C. In contrast, the bare and Al₂O₃-coated cathodes only maintained 65% and 71% of initial capacity, respectively. Additionally, the alucone-coated cathode delivered 113 mAh g⁻¹ at a 10 C rate, while the bare cathode could only deliver 66.5 mAh g⁻¹. The almost 95% retention of original capacity as the current density returned to 1 C indicated superior rate capability. Electrochemical impedance spectroscopy (EIS) of the three electrodes before and after 50 and 100 cycles showed that the growth of R_{ct} was significantly suppressed upon cycling in the alucone-coated electrode. These findings suggest that alucone could effectively suppress electrolyte side

reactions and HF attacks while providing better mechanical support to accommodate the volume change due to phase transitions.^[136]

Though less commonly explored, a couple exploration of polymer coating material for metal oxide cathodes LIBs have demonstrated promising results, as they offer the advantage of facile modification of functional group and relatively easy coating procedure.^[137,138] For instance, Yang et al. reported a self-adaptive polymer (polyrotaxane-co-poly(acrylic acid)) coating built on a $\text{LiNi}_{0.6}\text{Mn}_{0.2}\text{Co}_{0.2}\text{O}_2$ (NCM622) via a simple solution-processed method. The customized polymer consisted of α -cyclodextrin (α -CD) rings threaded on a poly (ethylene glycol) (PEG) chain, and the α -CD rings were covalently cross-linked to PAA via ester linkages. The modified NCM611 demonstrated an extended cycling performance when comparing to the pristine NCM611 at various voltage windows. The protection mechanism of the self-adaptive was two-fold (Figure 6e): first, the sliding motion of the polymer chain provided the polymer with high docility and toughness, which buffered the mechanical stress and anisotropic volume deformation, thereby reducing the formation of microcracks. Secondly, the abundance of carboxyl groups could chelate with Mn, which reduced its dissolution into the electrolyte^[138]. This work exemplifies the potential of tailored polymer coating in addressing some of the instabilities of layered metal oxide materials used in LIBs/SIBs.

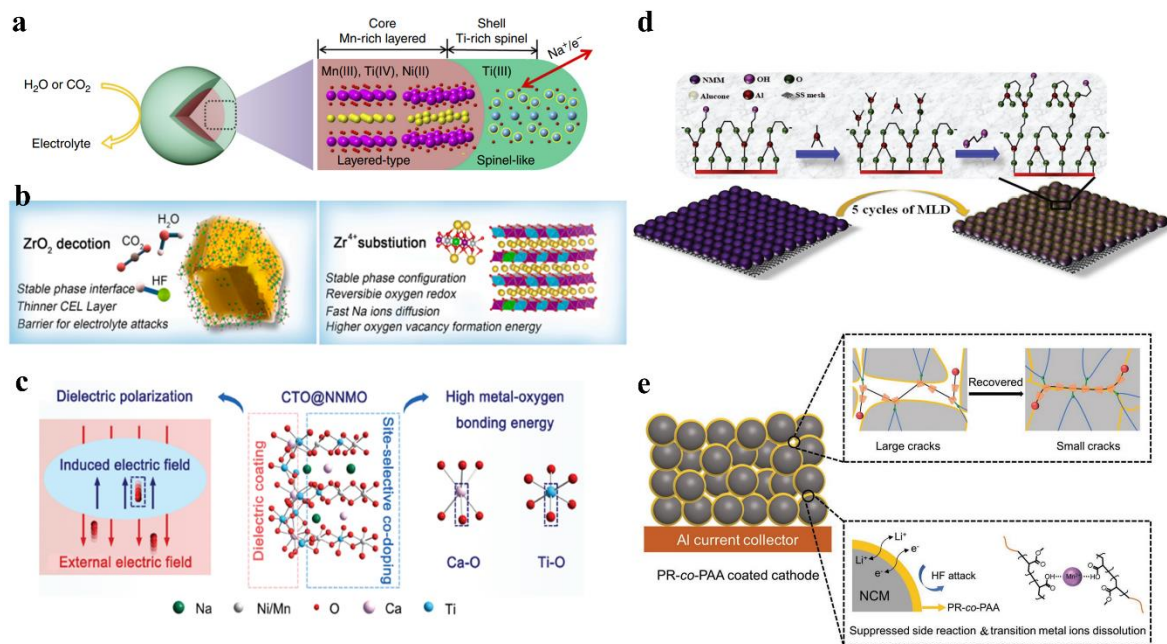


Figure 6. a) schematics showing the layer and bulk structure, and f) cycling performance of NaMnTi_{0.1}NiO₂ with a reconstructed Ti(III)-concentrated spinel-like oxide layer. Reproduced with permission.^[28] b) schematics showing design strategies of Zr⁴⁺ doping induced ZrO₂ coating. Reproduced with permission.^[128] c) schematic illustration of suppressed oxygen release mechanism with Ca/Ti co-doping and CaTiO₂ coating. Reproduced with permission.^[132] d) schematic illustrations of MLD deposition of alucone. Reproduced with permission.^[136] e) schematic illustrations of PR-co-PAA coating protective mechanisms. Reproduced with permission.^[138]

3.3 Heterostructure

Although Na_xMn_yTM_{1-y}O₂ exhibits limitations, combining various types of sodium manganese oxide into a composite can yield synergistic enhancements. Commonly explored heterostructure materials include P2/O3, P2/P3, and P2/tunnels composites, each showcasing unique mechanism in improving the performance of Na_xMn_yTM_{1-y}O₂.

P2/O3 heterostructure. Pure P2 and O3-Na_xMn_yTM_{1-y}O₂ have intrinsic limitations, which led to the idea of combining the two phases to achieve synergistic improvements.^[139] In 2015, Guo et al. developed a P2 (94.22 wt%)/O3 (5.78 wt%) Na_{0.66}Li_{0.18}Mn_{0.71}Ni_{0.21}Co_{0.08}O_{2+d} composite through

coprecipitation followed by a solid-state reaction (Figure 7a-c). The successful formation of a P2/O3 heterostructure was confirmed by SAED, HADDF, and ABF images. The electrochemical testing of the composite demonstrated an excellent capacity of 200 mAh g⁻¹ at 0.2 C when cycled between 1.5-4.5V, and retained 75% capacity after 150 cycles at 0.5 C.^[140] However, the use of cobalt posed an environmental and sustainability concern. To address this, Li et al. prepared a Co-free P2/O3 heterostructure by substituting Li for Ti in a P2-Na_{0.67}Mn_{0.55}Ni_{0.25}Ti_{0.2}O₂. XRD analysis indicated that portion of O3-phase increased with increasing Li doping, suggesting a possible method of tuning the composition by varying the concentration of Li doping.^[141] Following the strategy, Wang et al. reported a P2/O3 Na_{0.67}Li_{0.2}Fe_{0.2}Mn_{0.6}O₂ without any phase transition. The authors attributed the suppressed phase transition to the combined effect of Li-doping and P2/O3 biphasic structure. Consequently, the composite demonstrated improved cyclability with capacity retention increased from 6.5% to 83.5%.^[142]

Huang et al. reported a composite material by supersaturating Li to produce Na-P2 and Li-O3 intergrowth heterostructure without any P2-O2 transition at the deep charge state (Figure 7d, e). As evidenced by STEM ABF images, the composite consisted of Na-P2 and Li-O3 alternating structure, with Na-P2 being the major phase. The geometric phase analysis (GPA) simulation pattern of Na-P2/Li-O3 interface showed that the lattice mismatch between the two phases was responsible for the interfacial distortion. The authors proposed that the suppression of P2-O2 was due to the interfacial tensile shear stress exerted by the Li-O3 on Na-P2. Consequently, the composite maintained a capacity of 95.8 mAh g⁻¹ compared to 33.1 mAh g⁻¹ of pure P2 electrode after 200 cycles at 85 mA g⁻¹.^[143]

Interestingly, Sn-doping can also induce abnormal O3-phase in a P2 material. Xiao et al. reported a P2/O3-Na_{2/3}Mn_{1/3}Sn_{1/3}O₂. As shown by in-situ XRD, the electrode underwent multiple reversible phase transition: P2/O3 → P2/O3/P3 → P2/P3 → P2/O3/P3 → P2/O3. The conversion of O3 to P3 likely gave rise to an enhanced rate performance of the electrode. Consequently, the electrode maintained a superior 78.89% of capacity when switched from 24 mA g⁻¹ to 600 mA g⁻¹, and achieved an excellent 82.16% capacity retention after 600 cycles at 240 mA g⁻¹.^[144]

P2/P3 heterostructure. With possible synthesis of P3-phase, its higher discharge capacity, and faster Na⁺ diffusion, a P2/P3 heterostructure combining the advantages of both phases could achieve synergetic improvement. In 2014, Chagas et al. studied the influence of synthesis temperature on the structure of Na_xNi_{0.22}Co_{0.11}Mn_{0.66}O₂, finding that a 900 °C synthesis temperature produced pure micron-

sized P2-type particles, while 700 °C produced pure nano-sized P3-type particles. By adjusting the temperature to 750 °C, a P2/P3 biphasic particles was successfully synthesized.^[133,145]

Since then, several studies have been carried out to investigate P2/P3 heterostructures. In 2015, Chen et al. reported a P2/P3- $\text{Na}_{0.66}\text{Co}_{0.5}\text{Mn}_{0.5}\text{O}_2$ by calcinating the precursor powder at 800 °C, and confirmed the co-existence of P3 (76.05wt%) and P2 (23.95wt%) via XRD patterns. The composite demonstrated excellent cycling performance and rate performance as it delivered 86.5 mAh g⁻¹ at 10C, 67.0 mAh g⁻¹ at 20 C, and maintained 91% and 84.5% of initial capacity after 100 cycles at 10 C and 20 C, respectively.^[146]

Zhou et al. reported a P2/P3- $\text{Na}_{0.7}\text{Li}_{0.06}\text{Mg}_{0.06}\text{Ni}_{0.22}\text{Mn}_{0.67}\text{O}_2$ by calcinating the precursor powder at 800 °C. The material delivered 119 mAh g⁻¹ at 0.2 C with high initial Coulombic efficiency of 94.8%, and a high-capacity retention rate of 94.8% was achieved after 50 cycles between 2.0 – 4.4 V. At a rate of 5 C, the composite could deliver 85.5% of the capacity at 0.2 C, demonstrating remarkable rate performance. In-situ XRD revealed that the composite underwent P2/P3 – OP4/P3 phase transition, which contributed to the excellent rate and cycling performance due to the less detrimental P2-OP4 transition.^[147]

A recent study by Jiang et al. introduced an innovative dealloying-annealing approach for synthesizing P2/P3- $\text{Na}_{0.67}\text{Mn}_{0.64}\text{Co}_{0.30}\text{Al}_{0.06}\text{O}_2$. This approach enabled precise control over the phase composition by manipulating the content of cobalt substitution, making it a highly controllable method for synthesizing P2/P3 heterostructures. The optimal composition, denoted as MCA-3, contained 37.8% P3 phase with 30% cobalt doping, exhibited significantly improved cycling and rate performance. Specifically, the MCA-3 composition delivered a capacity of 83 mAh g⁻¹ at 1700 mA g⁻¹ and retained 81% of its capacity after 200 cycles, compared to 67% for the pure P2 phase (MCA-1).^[148]

P2/tunnel heterostructure. Tunnel-type transition metal oxides are known to have excellent rate and cycling performance, owing to their open 3D tunnels that facilitate Na⁺ diffusion and accommodate structural stress upon cycling (Figure 7f). However, their theoretical capacity is limited to 121.4 mAh g⁻¹ due to low sodium content (typical chemical formula is $\text{Na}_{0.44}\text{MnO}_2$, space group Pbam). In 2017, Wu et al. synthesized a P2 (65.4%)/tunnel (34.6%)- $\text{Na}_{0.6}\text{MnO}_2$ through a simple co-precipitation method (Figure 7g). The composite showed a high reversible capacity of 193.6 mAh g⁻¹ at 1C, retaining 70% of initial capacity after 100 cycles, compared to 166 mAh g⁻¹ and 38% retention for the pure P2 counterpart. The composite also delivered an unprecedentedly high capacity of 133.4 mAh g⁻¹ at 8 C,

underlying the synergistic effect of tunnel-layer hybrid structure. Moreover, its excellent rate capability was reflected via an extended cycling test at 10 C, where the composite delivered 83.3 mAh g⁻¹ after 700 cycles, corresponding to 72% capacity retention. The excellent performance of the composite was described by a current redistribution effect, which was revealed by a DFT simulation.^[149]

Extending this work, the same group investigated the effect of doping Ni²⁺, Cu²⁺, and Zr⁴⁺ into the P2/tunnel-Na_{0.6}MnO₂. To briefly summarized, Ni²⁺ induced high content of layered structure in the composite, Cu²⁺ shown to reduce the Jahn-Teller effect, and Zr⁴⁺ further increased the rate capability by increasing disorder in the TM layer.^[150–152]

In 2018, Xiao et al. developed a P2/tunnel intergrowth Na_{0.6}MnO₂ composite via a facile thermal polymerization method followed by a subsequent solid-state reaction. Due to the synergistic effect of intergrown layered/tunnel heterostructure, the composite demonstrated enhanced rate performance, delivering a high capacity of 80.6 mAh g⁻¹ at 1000 mA g⁻¹.^[153] The same group reported a cobalt-induced P2 (83.6%)/tunnel (9.02%) Na_{0.44}Co_{0.1}Mn_{0.9}O₂ composite which delivered a high capacity of 173.2 mAh g⁻¹ at 0.2 C in a voltage range of 2.0 V – 4.0 V. Even at 5 C, it delivered a remarkable capacity of 108.3 mAh g⁻¹ and maintained 81.97% of its initial capacity after 100 cycles.^[154]

In a similar study, Gao et al. reported an interface-rich P2 (33%)/tunnel (67%)-Na_xCo_{0.1}Mn_{0.9}O₂ where the coexistence of P2 and tunnel phase separated by interfaces was clearly observed via HRTEM. This composite material delivered capacity of 219 mAh g⁻¹ at 0.1 C, higher than that of the pure P2 (189 mAh g⁻¹) and tunnel phase (113 mAh g⁻¹) material. Through CV and EIS analysis of Na⁺ diffusion, the P2/tunnel composite demonstrated synergistic improvement as its Na⁺ diffusion was much higher than that of pure P2 or tunnel phase. The remarkable electrochemical performance of this hybrid material was attributed to the interfaces separating the P2 and tunnel phase, which offered additional channels that promoted the rate capabilities and additional charge storage at the vacancies or holes.^[155]

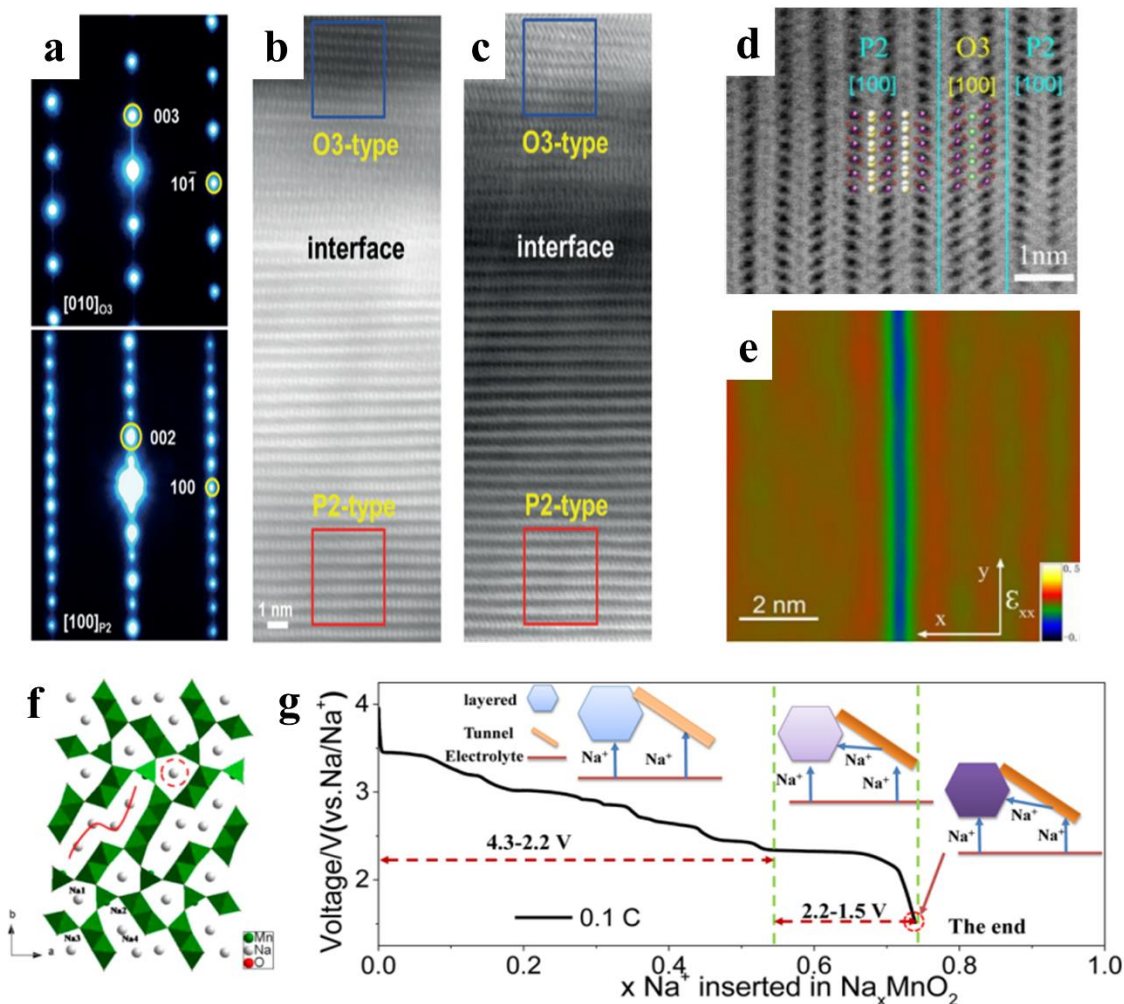


Figure 7. a) the SAED patterns, b) HADDF and c) ABF images of P2/O3 $\text{Na}_{0.66}\text{Li}_{0.18}\text{Mn}_{0.71}\text{Ni}_{0.21}\text{Co}_{0.08}\text{O}_{2+d}$ composite. Reproduced with permission.^[140] d) ABF images and e) the GPA analysis of Na-P2/Li-O3 composite. Reproduced with permission.^[143] f) crystal structure of tunnel-phase. g) proposed mechanism for P2-tunnel current redistribution effect. Reproduced with permission.^[149]

On the basis that tunnel-phase is structurally stable during cycling, more resistant to cathode-electrolyte side reactions and moisture, and have a higher Na^+ diffusivity, Huang et al. reported a refreshing core-shell composite. Specifically, tunnel- $\text{Na}_{0.44}\text{Mn}_{0.5}\text{Ti}_{0.5}\text{O}_2$ was used as a protective shell for a P2- $\text{Na}_{0.7}\text{Mn}_{0.66}\text{Ni}_{0.17}\text{Co}_{0.17}\text{O}_2$ core. When operating within 1.5 – 4.5 V, the composite delivered 200 mAh g^{-1} at 20 mA g^{-1} and 90 mAh g^{-1} at 1000 mA g^{-1} , while the bare P2 electrode could only delivered 60

mAh g⁻¹ at 1000 mA g⁻¹. Moreover, after 100 cycles at 50 mA g⁻¹, the composite could maintain 77.3% of initial capacity compared to 64.2% of the bare P2 electrode.^[156]

3.4 Summary

To summarize, doping into the TM and AM layer in Na_xMn_yTM_{1-y}O₂ can improve its stability. Reports of successful doping with Cu, Al, Li, Mg and Ti into the TM layer show that dopants can suppress Jahn-Teller distortion and TMO₂ layer gliding. Typically, suppression of Jahn-Teller distortion is related to the change in average oxidation state of Mn upon doping, while the suppression of TMO₂ layer gliding has been commonly ascribed to stronger dopant-O bond. Oxygen redox manifested by Li and Al doping can reduce the electrostatic repulsion between the adjacent TMO₂ layer has been shown as an interesting alternative mechanism for eliminating TMO₂ layer gliding. A more intuitive method in suppressing layer gliding is to implement “pillars” by doping into the AM layer. K, Mg, Ca, and Zn have been successfully doped into the AM layer and demonstrated lattice stabilization effect. In particular, implementation of K “pillars” results in the best result. In O3-phase, suppression of TMO₂ layers with doping is not often seen in the scientific community, with the majority of the efforts focusing on improving the reversibility of TMO₂ gliding.

Doping has also been demonstrated to improve electrochemical performance. Doping with elements such as Li, Cu, Al, Mg, Ti, Sn, and Zn demonstrated success in disrupting Na⁺/vacancy ordering which enhances the Na diffusion in the lattice. Doping with Sn and Ti can elevate the operating voltage of the material containing Ni²⁺/Ni⁴⁺ redox couple. Aside from TM species that are active for charge compensation, activating oxygen redox for additional charge storage can be achieved via doping with Li, Mg, Zn in Na_xMn_yTM_{1-y}O₂. Moreover, due to its higher redox potential (~ 4 V), utilizing oxygen redox can simultaneously increase the material operating voltage and reversible capacity. However, the current status of oxygen redox in Na_xMn_yTM_{1-y}O₂ is not practical due to fast voltage and capacity fading, and safety concerns associated with irreversible oxygen loss.

Owing to the superior energy density of oxygen redox, different strategies such as multiple doping (Cu/Mg, Al/Li, Mg/Li, and Ca/Li), and more recently introduced, topology design (TM layer superlattice and stacking sequence) has been shown to improve the reversibility of oxygen redox, making it more viable for practical applications.

Understanding the general effects of different dopants allows for rational design of multiple-doped material that exhibits synergistic improvements. Aside from the abovementioned examples in

improving oxygen redox, Li/Ti co-doping can improve rate capabilities by eliminating Na⁺/vacancy ordering, Zn/Cu co-doping can elevate Ni²⁺/Ni⁴⁺ redox potential and suppress phase transition.

Coating Na_xMn_yTM_{1-y}O₂ electrodes provides multiple benefits such as reducing active material dissolution, masking electrode-electrolyte side reactions and enhancing mechanical stability. Specifically, Al₂O₃ in the metal oxide category has been repeatedly shown to enhance the structural and surface stability that prolongs the cyclability. Other metal oxides such as ZrO₂, ZnO, TiO₂, and CuO₂ have also been successfully coated onto the surface, but their effectiveness is less than that of Al₂O₃. Binary metal oxides such as Li₂TiO₃ and CaTiO₃ are particularly interesting due to their ability to suppress oxygen release, which is useful when oxygen redox is utilized. Another class of coating material is polyanion compounds. Compounds such as NaPO₃ and CaHPO₄ are successfully coated by reacting precursor with Na_xMn_yTM_{1-y}O₂ surface residuals. These materials feature water and HF “scavenging” abilities which significantly enhanced the surface stability of cathode.

According to these reports, the effectiveness of coating materials is highly dependent on the coating method used. The use of ALD as a coating method produces Al₂O₃ with low thickness, high uniformity, and conformity, resulting in better surface stabilization. Following that, the use of MLD to produce more complex coating material such as alucone showed better improvement than Al₂O₃ coating. Finally, the less commonly explored polymer coating showcased their feasibility due to its simple coating method and high customizability.

The development of heterostructure design has led to the successful synthesis of composite materials that exhibit improved stability and electrochemical performance. P2/O3, P2/P3, and P2/tunnel composites have been successfully synthesized, each with unique advantages. P2/O3 composites demonstrate improved structural stability, resulting in extended cycling performance. The synthesis of P2/O3 composites typically involves higher Li-doping concentration that increases the sodium content in the AM layer. P2/P3 composites, on the other hand, can be synthesized by tuning the calcination temperature. Owing to higher Na⁺ content and faster Na⁺ diffusion of P3-phase, P2/P3 composite exhibits improved rate capability and high initial Coulombic efficiency that is important for full cell application. Lastly, P2/tunnel composites show excellent rate capabilities, thanks to the open 3D tunnel that allows for faster Na⁺ diffusion and accommodation of structural stress upon cycling. The synergistic effect of P2/tunnel has been described by a current redistribution mechanism, where the P2 component is responsible for charge storage, while the tunnel phase facilitates the transport of Na⁺.

Overall, the development of these heterostructures offers a promising avenue for improving the performance of $\text{Na}_x\text{Mn}_y\text{TM}_{1-y}\text{O}_2$.

Chapter 4 Functionalized Polyamic Acid as a Protective Layer on a P2-Na_{0.7}MnO₂ cathode for Sodium-ion Batteries

4.1 Introduction

The application of a protective layer on the surface of cathodes provides several advantages, including the reduction of active material dissolution, masking of electrode-electrolyte side reactions, and enhancement of mechanical stability. Notably, Al₂O₃, among metal oxide type coatings, has consistently demonstrated the ability to improve both structural and surface stability, thereby extending cyclability.^[118–121,124] Compounds like NaPO₃^[134] and CaHPO₄^[135] have been applied through reactions with Na_xMnO₂ surface residuals, showcasing water and HF "scavenging" capabilities that significantly enhance the surface stability of the cathode.

Polymer-type materials are less commonly used as a protective layer for the cathode due to its lower ionic conductivity. Few studies successfully demonstrated an increase in ionic conductivity of polymer solid-state electrolyte when the number of polar functional groups on the polymer increases. For instance, Lin et al. showed an increase in Li⁺ ionic conductivity due to the coordination of Li⁺ by C=O in poly(vinyl ethylene carbonate) (PVEC).^[157] In addition to increased ionic conductivity, incorporating functional groups can also realize mechanisms that can be effective in enhancing cathode stability. For instance, Yang et al. developed a self-adaptive polymer coating (polyrotaxane-co-poly(acrylic acid)) for LiNi_{0.6}Mn_{0.2}Co_{0.2}O₂ (NCM622) operated through two mechanisms: the sliding motion of the polymer chain enhanced docility and toughness, buffering mechanical stress and reducing microcrack formation; the abundance of carboxyl groups chelated with Mn, decreasing its dissolution into the electrolyte.^[138]

Herein, we investigate the encapsulation of a functionalized polyamic acid (PAA) polymer nanolayer on a P2-Na_{0.7}MnO₂ cathode material as a protective coating (Figure 8a). The PAA polymer is equipped with abundant hydroxyl/carboxyl/amide, aromatic ring, and fluoromethyl groups that can effectively enhance the interfacial and structural stability of the cathode material by mitigating electrolyte decomposition, reducing active material dissolution, and suppressing structural transition. By evaluating the rate capability and cyclability, the PAA coated cathode (PAA@NM) demonstrated significant improvement compared to the bare cathode (NM).

4.2 Results and Discussions

The molecular weight analysis conducted through gel permeation chromatography (GPC) revealed a number averaged molecular weight (M_n) of 74 kDa with a dispersity of 1.44 (Figure S 1 a). The as-synthesized polymer was characterized by ^1H and ^{19}F nuclear magnetic resonance (NMR), confirming its structure as well as fluoromethyl functionalization (Figure 8b, c).^[158–160] To validate the functionalization of the PAA polymer, Fourier-transform infrared spectroscopy (FTIR) was employed (Figure 8d). The analysis identified specific peaks, including a broad band in the $3700 - 2800 \text{ cm}^{-1}$ range corresponding to O-H and N-H stretching, C=O stretching in the imide ring at 1719 cm^{-1} , N-H bending at 1596 cm^{-1} , phenol O-H bending at 1393 cm^{-1} , aromatic amine C-N stretching at 1326 cm^{-1} , aromatic ester C-O stretching at 1289 cm^{-1} , and C-F stretching at 1186 cm^{-1} . The X-ray diffraction (XRD) pattern of the PAA polymer revealed the absence of noticeable crystallinity, which is a crucial factor for facilitating rapid Na^+ conduction through the polymer coating (Figure S 1 b).^[161–163] Thermogravimetric analysis (TGA) of the synthesized PAA polymer showed excellent thermal stability without weight loss up to $120 \text{ }^\circ\text{C}$, which is compatible with the drying temperature of the slurry to fabricate cathode (Figure S 1 c).

The powder XRD patterns (Figure 8e) of NM and PAA@NM align with a $\text{Na}_{0.7}\text{MnO}_2$ layered material exhibiting a P2 phase (PDF#27-0751). Notably, the strong peak intensity in the diffraction patterns without impurity peaks signifies the purity and high crystallinity of the samples. Importantly, the introduction of PAA polymer onto the NM powder surface did not induce any alterations to its crystal structure. The secondary electron microscope (SEM) images of the NM and PAA@NM samples indicate the formation of micron-sized particles with a uniform size distribution (Figure 8f, Figure S 2a, b). The morphologies of both samples are similar, featuring plate-like hexagonally shaped particles in accordance with previous reports.^[164] The coated sample's surface does not exhibit increased roughness compared to the bare sample, suggesting a thin layer of polymer conformally adheres to the surface of NM powder. Quantitative elemental mapping via energy-dispersive X-ray spectroscopy (EDS) on PAA@NM reveals a well-distributed composition of Na, Mn, and O throughout the material without agglomeration (Figure 8g). Furthermore, F and N mapping highlights the even overlap of these elements with the material, providing compelling evidence for the successful coating of PAA polymer. High-resolution transmission electron microscope (HR-TEM) was employed to examine the surface characteristic of these materials. The NM sample displayed exposed flaky edges which can contribute

to an accelerated interfacial degradation process (Figure S 2c, d). Conversely, PAA@NM sample displayed an unexposed edge, shielded by approximately 8 nm of PAA nanolayer on the surface of the NM powder (Figure 8h). No discernible lattice fringes were observed for the PAA nanolayer, aligning with its amorphous nature. By contrast, distinct lattice fringes with interplanar spacing of 2.53 Å corresponding to the (002) plane of a typical P2-Na_{0.7}MnO₂ were detected. This observation further substantiates the presence of a conformal PAA coating on the NM surface, which can be attributed to the abundant hydroxyl/carboxyl/amide groups that endow hydrogen – manganese interactions.^[165,166]

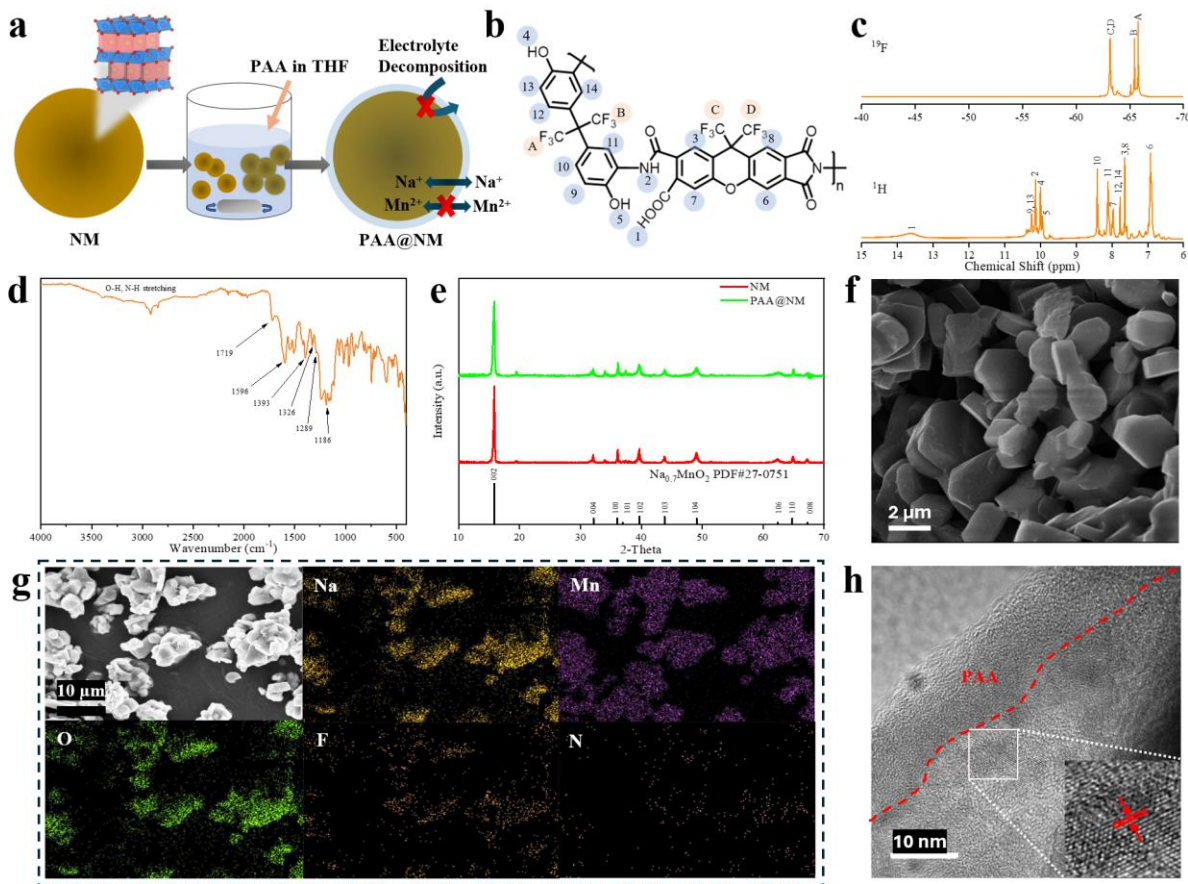


Figure 8. a) Schematic illustration of coating of NM cathode and multiple protective mechanism of PAA coating. b) Chemical structure, c) ¹⁹F (top) and ¹H (bottom) NMR spectra, and d) FTIR spectrum of the functionalized PAA polymer. e) XRD patterns of NM and PAA@NM. f) SEM image, g) EDS mapping, and h) HR-TEM image of PAA@NM.

The X-ray photoelectron spectroscopy (XPS) is useful for surface characterization of the cathode active materials owing to its shallow penetration depth of ~ 10 nm.^[167,168] In this work, XPS was conducted

on Na, Mn, O, C, F, and N, with subsequent deconvolution of the spectra into distinct peaks. The Na 1s, O 1s, and C 1s spectra reveal the presence of surface residuals (NaCOOH-like species) on the NM powder that are known to accelerate the deterioration of cathode.^[29,169] As these residuals were formed due to reaction between the surface NM and water/CO₂,^[33,170] the absence of these residuals for the PAA@NM powder suggests enhanced air stability conferred by the coating. Peaks in the C 1s and O 1s spectra of the PAA@NM sample have been ascribed to various carbon and oxygen species found on the PAA polymer, such as C-C/C-H, C-O, C=O, and CF₃,^[138,171] as well as the adventitious carbon (AdC) due to contamination^[172,173]. Furthermore, the presence of F and N was confirmed on the PAA@NM powder (Figure 9e, f).

Interestingly, analysis of Mn 2p spectra unveils a shift in the average Mn oxidation state upon the encapsulation with PAA polymer. The Mn 2p spectra, coupled with their deconvoluted peaks, show a splitting of Mn 2p_{3/2} and 2p_{1/2}, indicating the concurrent presence of Mn³⁺ and Mn⁴⁺ (Figure 9b). The integrated area under each peak correlates to the relative abundance of each species. For the surface or near-surface region of NM and PAA@NM samples, the Mn³⁺/Mn⁴⁺ ratio stands at 1.75 and 2.01, respectively. Since the PAA polymer adheres to the surface of NM particles via hydrogen bonding, the physisorption of the PAA polymer does not alter the chemical feature of NM particles. Consequently, the higher Mn³⁺/Mn⁴⁺ ratio observed with an increasing weight percentage of the PAA coating is attributed to the mitigation of the Mn disproportion reaction. This reaction splits Mn³⁺ into equal parts Mn⁴⁺ and Mn²⁺, with the latter being soluble in the electrolyte.^[28,174] The mechanism behind this reduced Mn disproportion reaction can be elucidated by the robust chelation of Mn species facilitated by the abundant hydroxyl/carboxyl/amide groups on the PAA polymer. In simpler terms, the plentiful polar functional groups from the PAA coating secure any as-formed Mn²⁺, impeding further Mn²⁺ formation.^[138,165,166]

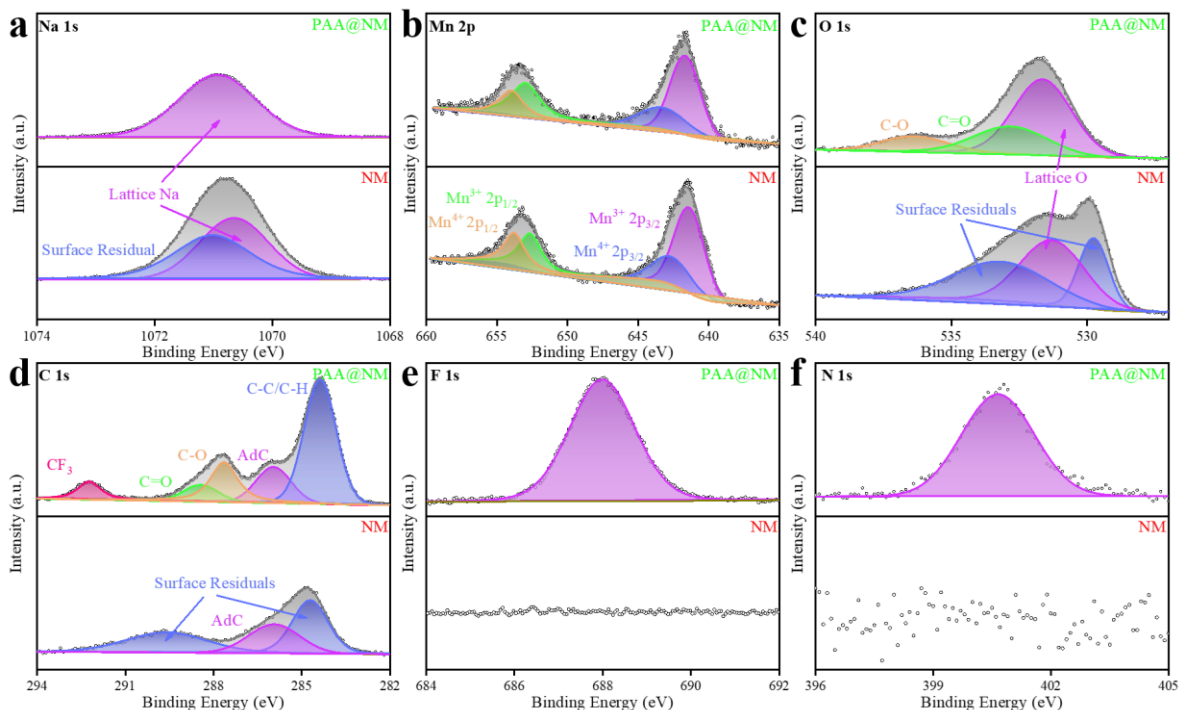


Figure 9. XPS spectra of PAA@NM and NM powder a) Na 1s, b) Mn 2p, c) O 1s, d) C 1s, e) F 1s, and f) N 1s.

To evaluate the electrochemical performance of the cathodes, sodium-ion half-cells were fabricated and tested within a voltage range of 1.5 – 4.2 V. All fresh half cells activated by undergoing cycling at a low current density of 10 mA g⁻¹ for 5 cycles (Figure 10a, Figure S 3). Upon the initial charging, the NM cathode exhibited an unexpectedly high capacity of 193.4 mAh g⁻¹, significantly surpassing the theoretical capacity of 170 mAh g⁻¹ for a typical P2-phase layered sodium manganese oxide material. Subsequent discharge resulted in a capacity of 141.2 mAh g⁻¹, yielding an unsatisfactory initial Coulombic efficiency of 73%. This additional capacity was attributed to the oxidation of electrolyte during high-voltage charging (4.2 V), resulting in electrolyte decomposition at the cathode-electrolyte interface.^[28,30] The pattern of high charge capacity and lower discharge capacity persisted for the second cycle, yielding a Coulombic efficiency of 86.3%. Following the third cycle, the Coulombic efficiency exceeded 95%, suggesting the formation of a passivating film on the cathode surface that reduced electrolyte decomposition.

Contrary to the NM cathode, the PAA@NM cathode exhibited a capacity of 73.2 mAh g⁻¹ upon the first charge due to a lower initial sodium content in the lattice of P2-Na_{0.7}MnO₂. However, unlike the

NM cathode, the Coulombic efficiency for the remaining four cycles exceeded 98%, indicating the absence of electrolyte decomposition due to enhanced interfacial stability in PAA@NM cathodes. This superior stability arises from the abundant fluoromethyl groups in the PAA polymer coating, where strong electron-withdrawing property of F species reduced the density of lone-pair electrons surrounding oxygen species, thereby elevated the oxidative stability at the interface.^[175–177]

Differential capacity analysis emerged as a crucial analytical tool for dissecting voltage plateaus, with each peak representing a specific voltage plateau on the charge/discharge curve (Figure 10b). During charging, the peak in the 2.0 to 2.5 V range corresponded to the $\text{Mn}^{3+}/\text{Mn}^{4+}$ oxidation reaction, while peaks in the 2.5 to 4.0 V range were associated with Na^+ /vacancy ordering observed in solid solution reactions.^[35,136,178] The NM cathode exhibited a shifted peak voltage in the $\text{Mn}^{3+}/\text{Mn}^{4+}$ oxidation reaction due to increasing resistance from continuous electrolyte decomposition as the as-formed CEI layer hinder the transport of Na^+ ^[28,30]. In contrast, the peak voltage associated with $\text{Mn}^{3+}/\text{Mn}^{4+}$ oxidation for the PAA@NM cathode remained consistent throughout the activation process. An obvious peak in the 4.0 to 4.2 V range for the NM cathode indicated a structural transition from P2 phase to O2 phase, deemed undesirable due to associated volume variations and stress on the crystal leading to crack growth.^[22,27] During discharge, a weaker peak in the 4.2 to 4.0 V range indicated partial reversibility of the P2/O2 transition at high voltage. Peaks in the 4.0 to 2.5 V range during discharge were attributed to charge ordering, with a peak in the 2.5 to 1.7 V range related to the $\text{Mn}^{4+}/\text{Mn}^{3+}$ reduction reaction. Notably, a broadening of peaks during the first two discharge cycles for the NM cathode suggested the occurrence of additional mechanisms in this voltage region.

To investigate the effect of PAA polymer on the structural stability of NM particles, XRD experiments were conducted on both NM and PAA@NM cathodes in their charged and discharged states (Figure S 4). Charging the NM cathode to 4.2 V resulted in the disappearance of most P2 characteristics peaks, notably a significant reduction in the intensity of the peak corresponding to the (002) crystal plane. This observation signifies the loss of the P2 structure. Simultaneously, new peaks at $2\theta = 12.2$ and 25.2 emerged, commonly attributed to the hydration peak, indicating the intercalation of trace water molecules into the lattice of the material which leads to the degradation of the material.^[63,179,180] Upon discharging the NM cathode to 1.5 V, the characteristic peaks of the P2 phase reappeared but with lower intensity. However, a broadening around the (002) peak indicated a distorted lattice, indicative of Mn^{3+} Jahn-Teller distortion.^[180] This distortion is frequently associated with the dissolution of Mn

species from the lattice into the electrolyte, contributing to crack propagation and material amorphization.^[28,174]

In contrast, the PAA@NM cathode exhibited remarkable structural stability, with XRD patterns in its charged and discharged states closely resembling its pristine form. This enhanced structural stability is attributed to the protective mechanism of the PAA coating, operating on two fronts: 1) the high mechanical strength of the PAA due to high percentage of aromatic rings, coupled with abundant hydroxyl/carboxyl/amide groups fostering π - π , π -hydrogen, and hydrogen-hydrogen interactions^[181–185] that effectively prevented structural transitions during the charged state^[121], and 2) the abundance of functional groups facilitated a chelation mechanism, preventing Mn dissolution and mitigating the impact of Jahn-Teller distortion on the structural stability of the cathode material.^[138,165,166]

The cathodes were tested at different current densities from 20 to 2000 mA g⁻¹ (Figure 10c). As shown, PAA@NM cathode exhibited the best rate performance, as it achieved capacities of 127.8, 112.7, 97.1, and 89.5 mAh g⁻¹ at current densities of 50, 100, 200, 1000, and 2000 mA g⁻¹. The PAA@NM cathode demonstrated a particularly superior charge transfer, especially at higher current densities, exhibiting 70% capacity retention at 2000 mA g⁻¹, in stark contrast to the 57% observed for the bare sample. The charge/discharge curves at different current density reveal a lower polarization due to an enhanced charge transfer for the coated cathodes (Figure S 5a, b). As the mechanism ionic transport through polymer is driven by the influence of polar groups within polymer chains^[157,186,187], the improved rate capability of the coated cathodes stems from more efficient Na⁺ transport between cathode and electrolyte compare to that of as-formed CEI on the NM cathode.^[125]

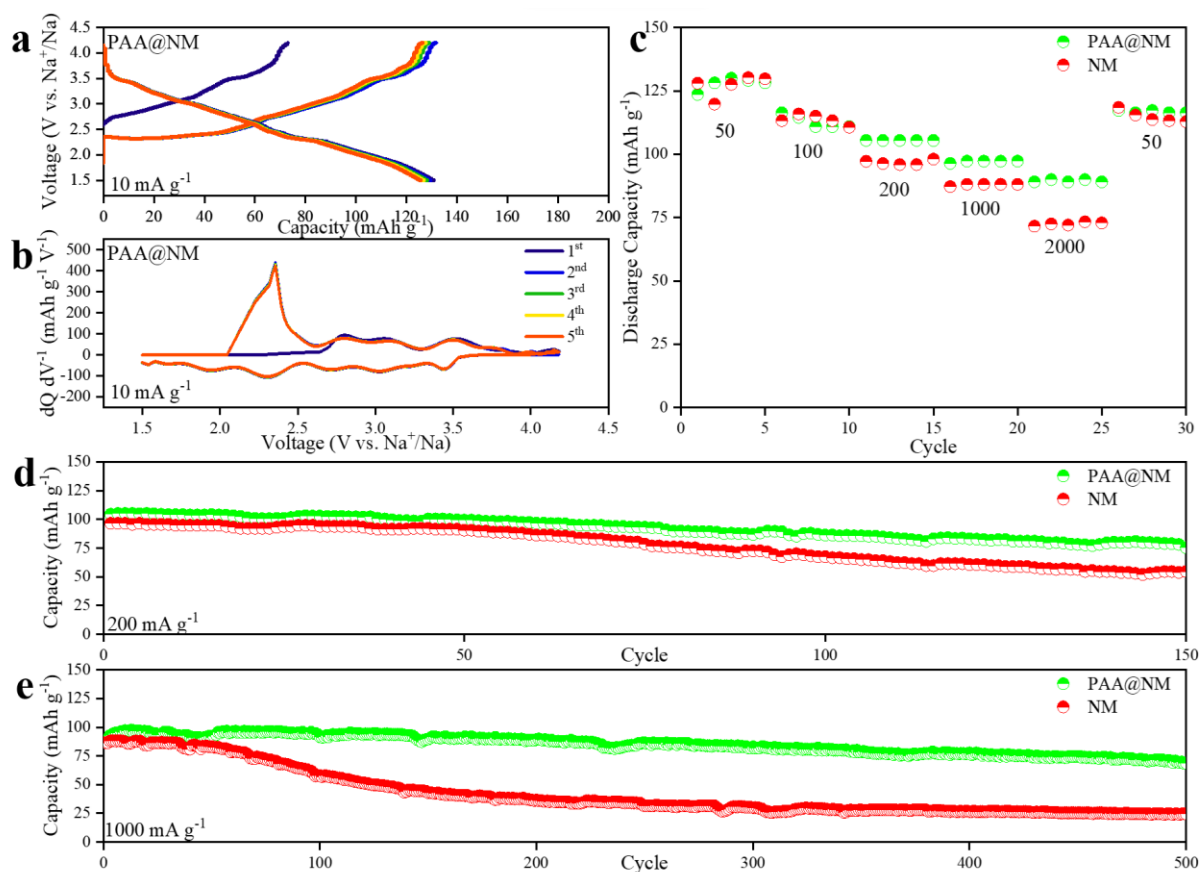


Figure 10. a) charge-discharge curve of the initial activation at 10 mA g^{-1} , and b) corresponding $dQ \text{ dV}^{-1}$ profiles for the PAA@NM cathode. c) rate capability test at different current density from 50 mA g^{-1} to 2000 mA g^{-1} , d) cycling test at 200 mA g^{-1} , and e) long cycling test at 1000 mA g^{-1} for NM and PAA@NM cathodes.

The cathodes were cycled at 200 mA g^{-1} for 150 cycles to evaluate their stability under repeated charge and discharge (Figure 10d). Remarkably, the PAA@NM cathode demonstrated a capacity retention of 75.7% after 150 cycles, while the NM cathode only retained 56.6%. To investigate their long-term cycling capabilities, the cathodes were subjected to cycling at 1000 mA g^{-1} for 500 cycles (Figure 10e). Intriguingly, the bare cathode experienced a rapid decline in capacity to 24 mAh g^{-1} , resulting in a capacity retention of only 28% by the end of the cycling period. In contrast, PAA-coated cathodes exhibited significantly better capacity retention under high current density cycling, showcasing retention rates of 72% for PAA@NM cathode. Indeed, XRD result of the cycled cathodes show that

the NM cathode lost all P2 characteristic peaks and displayed intense hydration peaks while PAA@NM cathode retained its structure (Figure 11a).

Electrochemical impedance spectroscopy (EIS) analysis was conducted on the cathodes before and after extended cycling to investigate changes in impedance (Figure 11bFigure 8). The impedance spectra of pristine cathodes (before activation) are shown in Figure S 8. The impedance spectra (Nyquist plots) were fitted using a simple Randles model to extract parameters for the equivalent circuit (Figure S 7). The model includes R_e (electrolyte resistance), C_f/R_f (capacitance/resistance of the thin film on the anode), C_{dl} and R_{ct} (capacitance/resistance of the charge transfer resistance and double layer capacitance on the cathode), and Z_w (Warburg impedance associated with Na^+ diffusion into the bulk of the cathode material).^[28] Table 1 provides a summary of R_f , and R_{ct} obtained from fitting the equivalent circuit model to the Nyquist plot.

Table 1. Summary of model parameters of pristine and cycled NM and PAA@NM cathodes.

Electrode	R_f [Ω]	R_{ct} [Ω]
Pre-cycling NM	16	712
Cycled NM	606	1819
Pre-cycling PAA@NM	14	638
Cycled PAA@NM	25	751

Prior to cycling, both NM and PAA@NM cathodes have similar R_{ct} values, measuring at 712 and 638 Ω , respectively. Following cycling, the charge transfer resistance of the NM cathode surged to 1819 Ω , signifying severe interfacial degradation that amplified the impedance at the interface. In contrast, the coated cathode exhibited a modest rise in its charge transfer resistance, indicating the effective suppression of interfacial degradation.

The rise in impedance of the SEI layer corresponds to the trend observed in the charge transfer resistance of the cathodes. Notably, when the NM cathode was employed, the SEI resistance increased from 16 to 606 Ω , while a marginal increase from 14 to 25 Ω was observed with the PAA@NM cathode. The lesser increase in SEI resistance is attributed to the mitigation of crosstalk effects through a chelation mechanism between hydroxyl/carboxyl/amide groups and Mn species.

For a more direct insight into the impact of the coating material, the cycled cathodes were visualized through SEM (Figure 11c, d, Figure S 9). The NM cathode displayed extensive intergranular cracks across the electrode surface, indicative of the cathode losing its integrity during prolonged cycling at a high current density. These large intergranular cracks resulted in the disconnection of active material from the current collector, significantly contributing to capacity fading. Additionally, intragranular cracks were also observed, particularly on the (002) crystal planes which were responsible for Na⁺ intercalation/extraction. The development of large intragranular cracks is attributed to repeated volume expansion and collapse of the interlayer spacing, nucleating cracks and exacerbated by active material dissolution, propagating these cracks.^[27] The intragranular cracks further contribute to the cathode's disintegration, increasing the amount of active material unusable for Na⁺ intercalation/extraction. In contrast, the evaluation of the coated cathode's morphology post-cycling indicates that the PAA coating material can mitigate both intergranular and intragranular cracks, aiding the cathode in retaining its capacity despite high current density cycling.

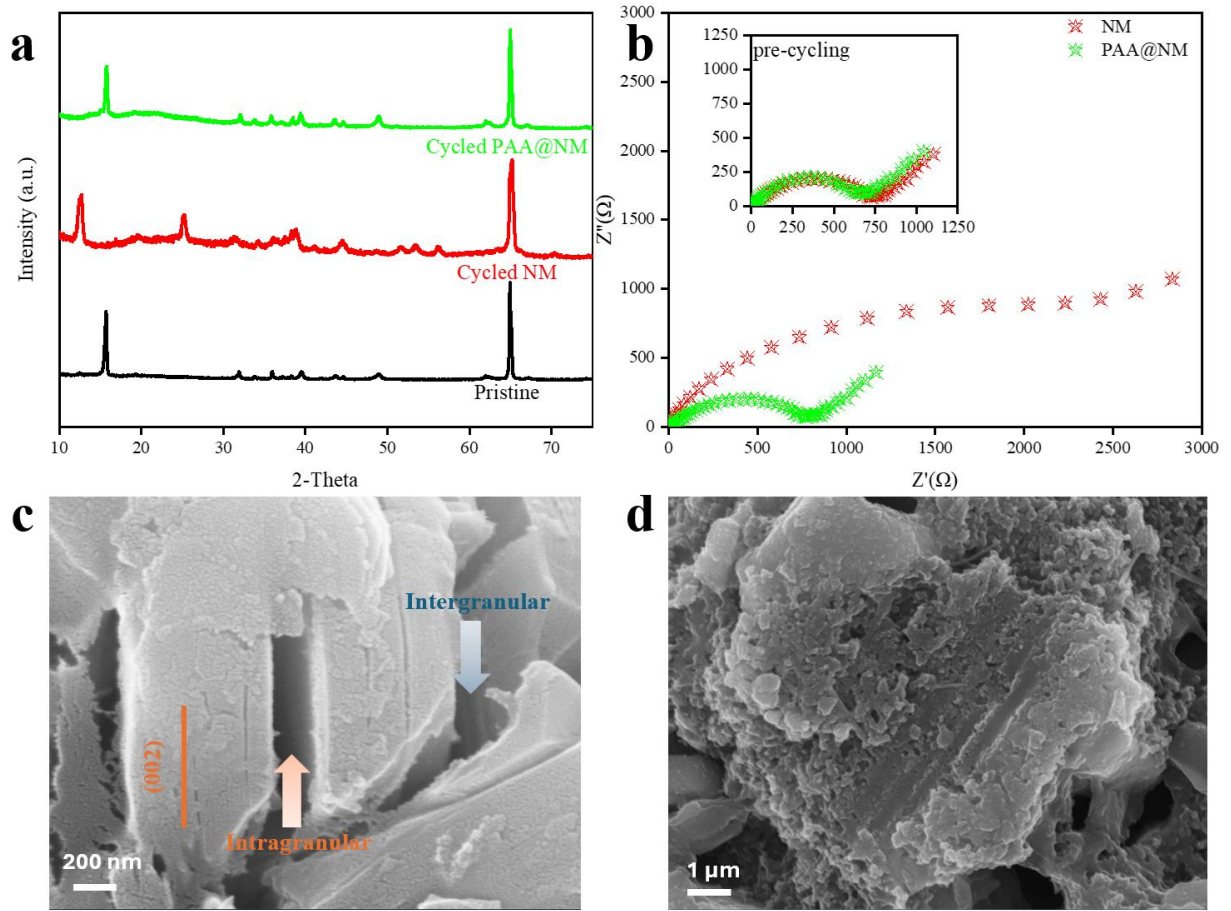


Figure 11. a) Nyquist plot of pre-cycling, and b) after 500 cycles at 1000 mA g^{-1} . SEM image of the electrodes c) before and d) after 500 cycles at 1000 mA g^{-1} .

4.3 Experimental

Synthesis of NM: NM synthesis employed a straightforward high-temperature solid-state method. Stoichiometrically amounts of sodium carbonate and manganese (III) oxide were thoroughly mixed and grounded using Agate pestle and mortar to a homogeneous precursor mixture. This precursor underwent heating in a tube furnace at 900 °C for 12 hours, with a heating rate of 10 °C/min under air conditions, resulting in the production of NM powder.

Synthesis of PAA polymer: The two-component PAA solution was prepared using 2,2'-Bis(3-amino-4-hydroxyphenyl) hexafluoropropane (1) and 9,9-bis(trifluoromethyl)-2,3,6,7-xanthene tetracarboxylic dianhydride (2) and dimethylacetamide (DMAC) as a solvent under an argon atmosphere. The mole ratio of (1)/(2) was fixed at 1. In detail, 1 (1.75 g, 4.78 mmol) was completely dissolved in 30 g of DMAC while stirring in a three-neck flask at room temperature. 2 (2.19 g, 4.78 mmol) was added into 1 solution in three aliquots in 30 min. Then, the above mixture was stirred for another 8 hours to form the PAA solution. The PAA sediment was collected and dried in a vacuum oven overnight at 60 °C.

Synthesis of xPAA@NM: To coat the NM powder with PAA polymer, 50 mg of the polymer was first dissolved in 10 ml of tetrahydrofuran (THF) to prepare a 5 mg ml⁻¹ PAA solution. Subsequently, 500 mg of NM powder was dispersed into 2 ml of the PAA solution to prepare PAA@NM. The mixture underwent continuous stirring for 2 hours, followed by 30 minutes of sonication. The mixture was then transferred to a vacuum chamber to allow THF evaporation under room temperature.

Electrochemical Testing: The cathodes were prepared using the slurry casting method. Specifically, a slurry was created by thoroughly mixing 80% active material (NM or PAA@NM), 10% polyvinylidene fluoride (PVDF) as a binder, and 10% carbon black in N-Methylpyrrolidone (NMP) solvent. This slurry was cast onto aluminum foil using a doctor's blade and subsequently dried in an oven for 12 hours at 80 °C. The typical loading level was set at 2–3 mg cm⁻². The cathodes were then punched into discs with a 12 mm diameter and assembled into sodium-ion half-cells using CR2032-type coin cells. Sodium discs, prepared by rolling sodium metal cubes into sheets and punching into 16 mm diameter discs, were used as the anode for the half-cells. Discs of 18 mm glass fiber B (GF/B) served as the separator, with 1.0 M NaClO₄ in EC/DMC (1:1) containing 5 wt. % fluoroethylene carbonate (FEC) additive employed as the electrolyte. Charge/discharge tests were conducted on a Land CT2001A battery test system (Land, Wuhan, China) within a voltage range of 1.5 to 4.2 V at 25°C. EIS experiments were

carried out on a potentiostat (VPS-300, Bio-Logic, France) in the frequency range of 100 mHz to 1 MHz with a sinus amplitude of 10 mV.

Physical Characterization: XRD experiments were conducted on a desktop XRD machine (Miniflex 600, Rigaku, Japan) using Cu K α radiation ($\lambda = 1.5406$ nm). The materials' morphology and elemental mapping were examined using a field emission SEM with EDX capability (UltraPlus, Zeiss, Switzerland). The visualization of the PAA coating layer on NM powder was performed by HR-TEM (JEM-F200, JEOL, Japan). Surface chemical features were analyzed using XPS (ESCLAB 250Xi, Thermo Fisher Scientific, USA). The infrared absorption spectrum experiment was conducted using the Bruker Vector 33 Fourier-transform infrared spectrometer. Infrared attenuated total reflection mode was selected for detection, and the testing wavelength range was set at 400-4000 cm $^{-1}$. NMR hydrogen and fluorine spectra were tested on a Bruker Avance spectrometer. Deuterated dimethyl sulfoxide was employed as the solvent, with tetramethylsilane (TMS, $\delta = 0$ ppm) used as the internal reference. Thermal stability analysis of polymers was conducted using the TA Instruments TGA 5500 thermogravimetric analyzer. The experiments were performed under a nitrogen protective atmosphere. The temperature range was set between 40 to 800 °C, with a heating rate of 10 °C/min. The molecular weight of prepared PAA polymer was measured by gel permeation chromatography (polystyrene standard in tetrahydrofuran (THF)) to give average M_n 74 kDa.

Chapter 5 Conclusion

The development of SIBs as an alternative energy storage solution continues to remain a popular research area due to the growing concerns of high demand but low supply of lithium. Layered transition metal oxide is widely investigated as a cathode technology, with Mn-based ($\text{Na}_x\text{Mn}_y\text{TM}_{1-y}\text{O}_2$) being a promising candidate due to its material abundance, low-cost, and relatively higher reversible capacity ($\sim 160 \text{ mAh g}^{-1}$). However, this material suffers from unsatisfactory cyclabilities that limit their practical applications.

The inferior cyclability of $\text{Na}_x\text{Mn}_y\text{TM}_{1-y}\text{O}_2$ stems from the structural and surface instabilities. In particular, gliding of TMO_2 layers upon Na^+ de/intercalation and Jahn-Teller distortions due to Mn^{3+} cause structural instabilities. The results of which are cracks nucleation that disintegrate the cathode material. The dissolution of Mn contributes to surface instabilities due to the formation of corrosive species in the electrolyte during operation, which propagates the nucleated cracks. The formation of larger cracks exposes a higher surface area to the electrolyte, which accelerates the growth of CEI that impedes the transport of Na^+ between electrolyte and cathode. Albeit having higher charge storage capabilities than polyanion compounds, there is still room for improvement in its energy and power density. This review has introduced current strategies in improving $\text{Na}_x\text{Mn}_y\text{TM}_{1-y}\text{O}_2$, namely doping, coating, and heterostructure design.

Doping has been shown to be an effective strategy for improving the stability and electrochemical performance of $\text{Na}_x\text{Mn}_y\text{TM}_{1-y}\text{O}_2$. Successful doping with various elements such as Cu, Al, Li, Mg, and Ti into the TM layer has been shown to reinforce the lattice and suppress Jahn-Teller distortion and TMO_2 layer gliding. Doping with K, Mg, Ca, and Zn into the AM layer has been found to stabilize the lattice by implementing "pillars". Various dopants have been shown to disrupt Na^+ /vacancy ordering thereby enhancing Na^+ diffusion, with Ti-doped materials and multiple-doped systems containing Ti exhibiting superior rate capabilities. Doping with Sn and Ti can elevate the operating voltage of the material, particularly when the $\text{Ni}^{2+}/\text{Ni}^{4+}$ redox couple is used for charge compensation. Dopants such as Li, Mg, and Zn can facilitate oxygen redox, contributing to a higher energy density. However, fast capacity and voltage drop are associated with oxygen redox due to irreversible oxygen loss. Strategies such as multiple doping and topology design can improve the reversibility of oxygen redox. Aside from improving oxygen redox, multiple doping can invoke synergistic effects that further mitigate some of the other challenges mentioned above. Particularly, HEO materials with at least five elements in the

TM layer show high entropy stabilization effect, highlighting the importance of rational selection of dopants.

Combining multiple phases in a heterostructure design can potentially lead to breakthroughs in performance. The goal of heterostructure is to combine the intrinsic advantages of different phases to achieve a synergistic effect. Examples of prominent heterostructures include P2/O3, P2/P3, and P2/tunnel can simultaneously improve reversible capacity, cyclability, and rate performance. Specifically, P2/O3 and P2/P3 exhibit higher capacity and stability, while P2/P3 and P2/tunnel feature better rate performance.

The main focus of coating is to improve the surface stability of $\text{Na}_x\text{Mn}_y\text{TM}_{1-y}\text{O}_2$. Currently, metal oxide coating, especially Al_2O_3 , is the most popular coating material due to its ability to protect the surface and extend cycling performance. Other metal oxides like ZrO_2 , TiO_2 , CuO , Li_2TiO_3 , and CaTiO_3 have also been studied. Polyanions such as NaPO_3 , NaCaPO_4 , and AlPO_4 , NASICON-type $\text{NaTi}_2(\text{PO}_4)_3$ exhibit similar effects in passivating the surface, protecting against HF attacks, and eliminating water in the electrolyte. Extending from ALD to MLD, more complex alternative coating material such as alcone demonstrated better improvement compared to Al_2O_3 .

Though polymer-typed coating materials are less studied, facile functionalization allows for a higher degree of freedom in material customization. We have demonstrated the effective encapsulation of NM cathodes with a nanolayer of PAA polymer film. The incorporation of diverse functional groups on the polymer imparts multiple protective mechanisms to enhance the cathode's performance significantly. Firstly, the introduction of fluoromethyl groups elevated the oxidative stability at the interface, effectively suppressing electrolyte decomposition during cycling. Secondly, the abundant hydroxyl/carboxyl/amide functional groups facilitated the conformal coating of PAA polymer on the NM particle surface and prevented active material dissolution through a chelation mechanism. Moreover, these polar functional groups contributed to improving the ionic transport of Na^+ across the cathode/electrolyte interface. Thirdly, the high toughness, achieved through interactions among the functional groups, mitigated structural transitions during charge and discharge, leading to improved structural stability. Collectively, these synergistic effects contributed to a remarkable enhancement in the cyclability of the NM cathode, achieving an outstanding 75.7% capacity retention after 500 cycles at 1000 mA g^{-1} , in sharp contrast to the 28% observed in the unmodified NM cathode. This research introduces an effective strategy for enhancing the interfacial and structural stability of NM cathodes,

showcasing the potential of functionalized polymers as promising coating materials for battery cathode materials.

Future work should continue with the abovementioned strategies. The current body of literature on topology design is limited and should be extended to other dopant such as Zn, or multiple-doped system. In addition, efforts should focus on identifying key topology features of newly designed materials, as early reports suggest their significance in material performance.

Regarding HEO materials, there is a need for further investigation into the underlying mechanisms of their stabilization effects. A systematic approach to synthesizing different HEO compositions can accelerate the exploration of these materials. While some reports have demonstrated activated oxygen redox for charge compensation, further work is necessary to understand the effect of high entropy on oxygen redox.

While coating provides protection against electrolytes, combining coating with other strategies can result in more comprehensive improvements. Thus, future research should focus on identifying the optimal combination of strategies. The role of coating in suppressing oxygen release could be significant, and it is essential to understand this mechanism through ongoing research.

To fully realize the potential of heterostructure systems, it is crucial to gain a comprehensive understanding of the improvement process through advanced characterization techniques. This understanding will not only facilitate the development of new and improved heterostructure systems but also aid in the identification of optimal combinations of strategies, including ternary or quaternary heterostructures, which have the potential to achieve unprecedented levels of performance.

Supplementary Information

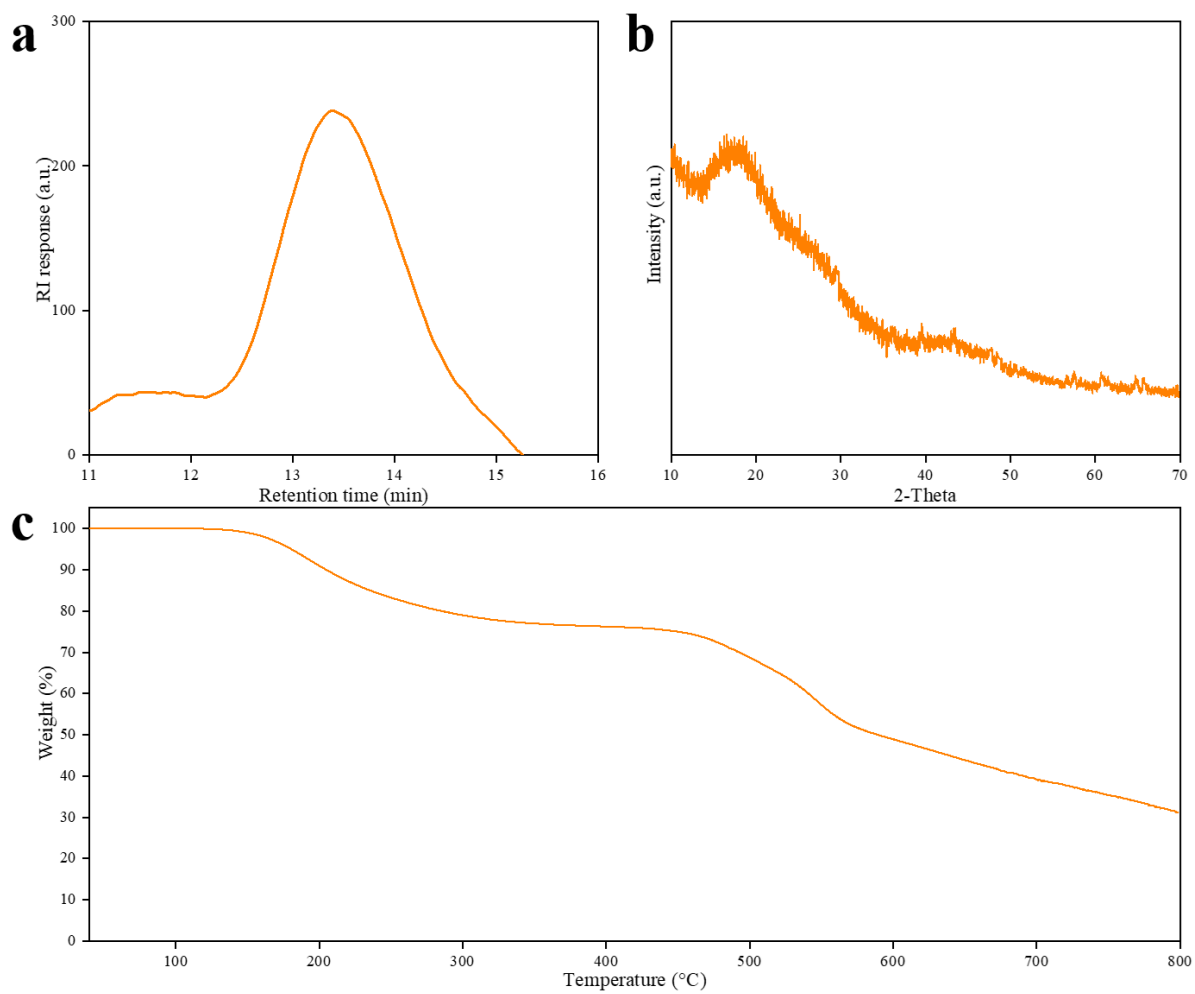


Figure S 1. a) GPC, b) XRD, and c) TGA results of the functionalized PAA polymer.

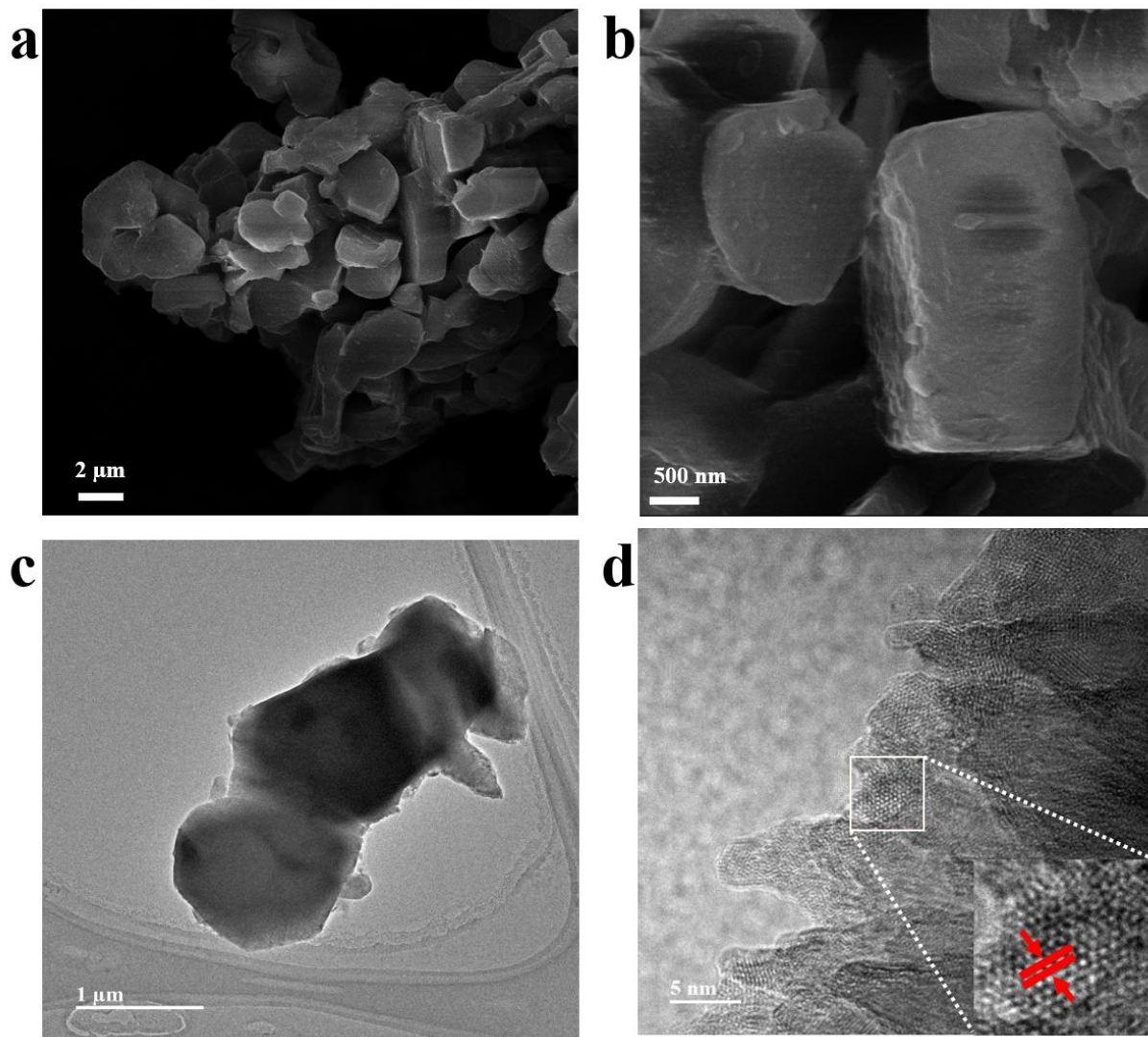


Figure S 2. a-b) SEM images and c-d) TEM images of NM.

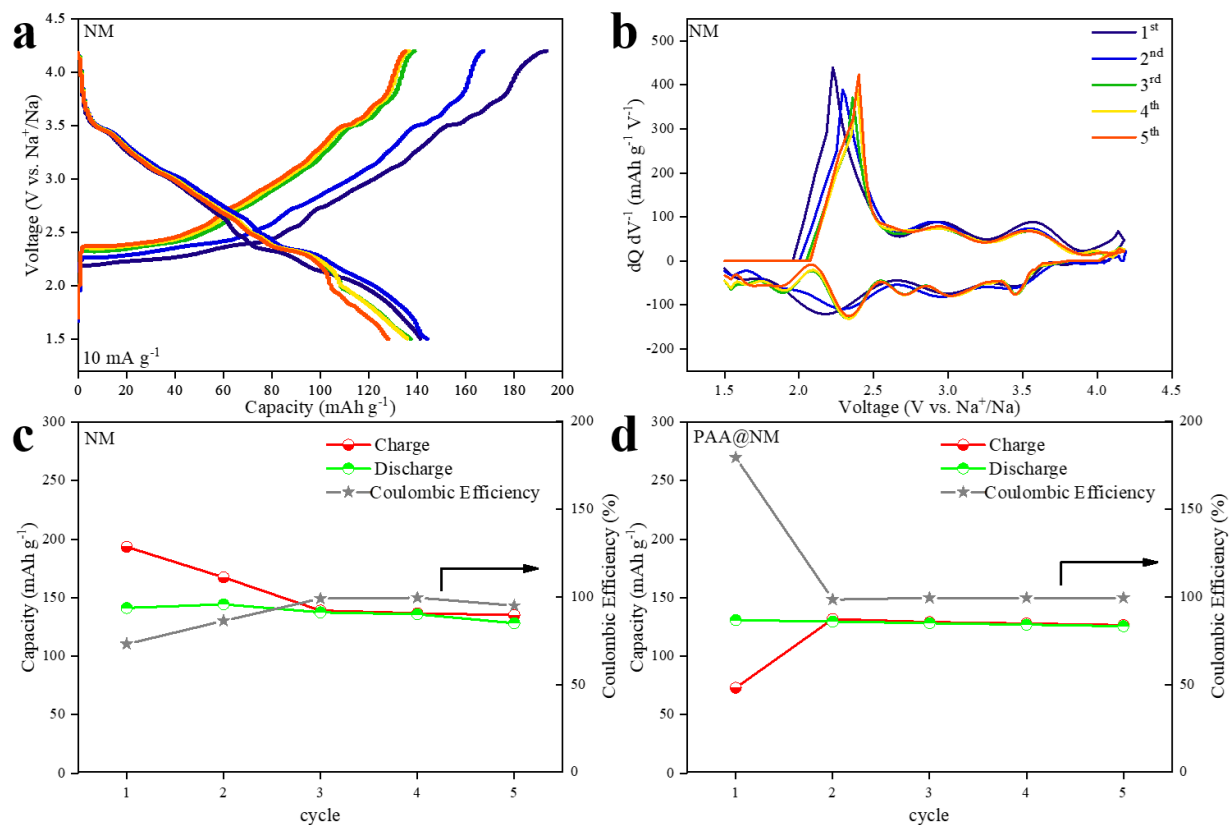


Figure S 3. a) charge-discharge curve of NM cathode and b) corresponding dQ/dV^{-1} . c) charge and discharge capacities, and corresponding Coulombic efficiencies during the first cycles of activation process for NM and d) PAA@NM cathodes.

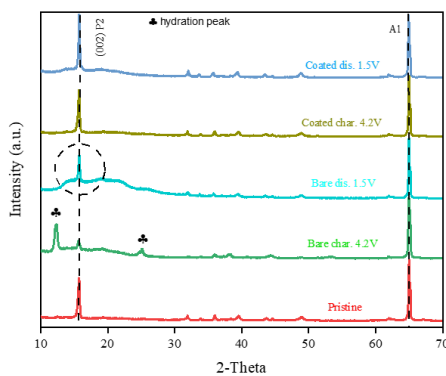


Figure S 4. Comparison of XRD patterns of NM and PAA@NM cathodes when charged to 4.2 V and discharged to 1.5 V.

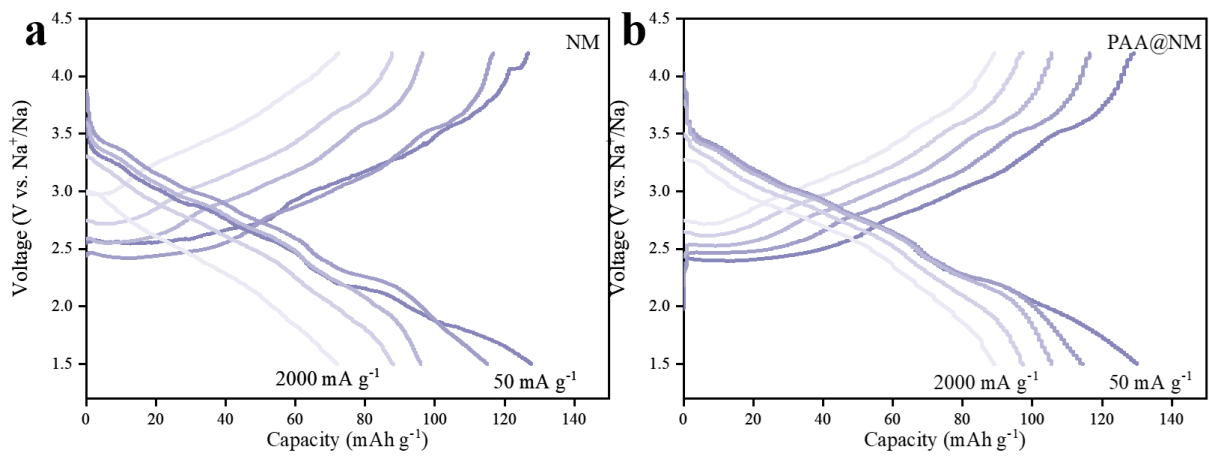


Figure S 5. a) Charge-discharge curve during rate capability test of NM and b) PAA@NM cathodes.

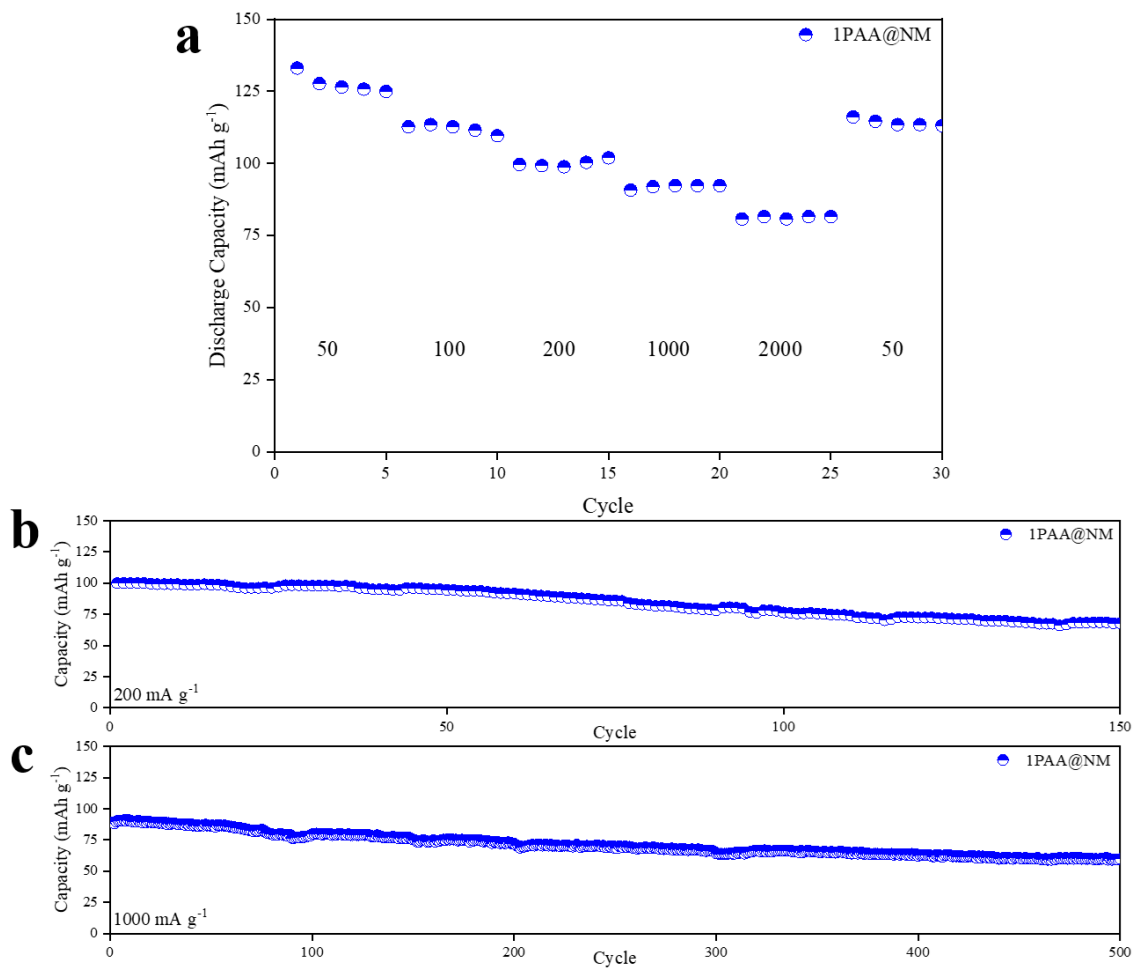
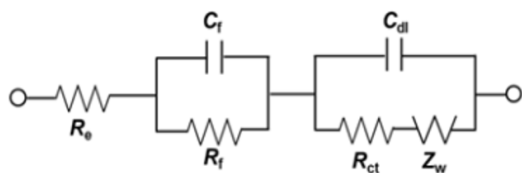


Figure S 6. a) rate capability, b) cycling test at 200 mA g⁻¹, and c) cycling test at 1000 mA g⁻¹ for the 1wt% PAA coated NM cathodes.

a



b

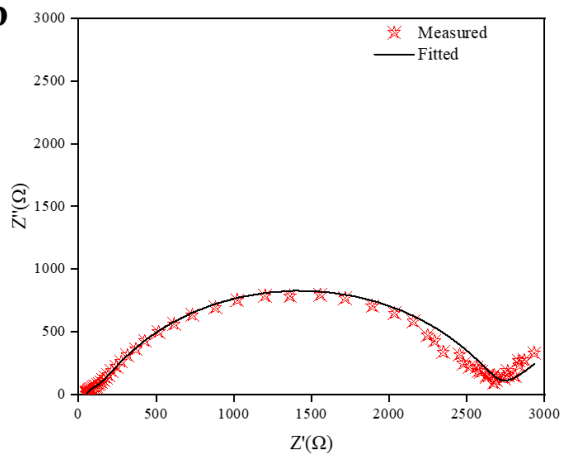


Figure S 7. a) Randles model for fitting EIS results. b) comparison of experimental and fitted impedance data.

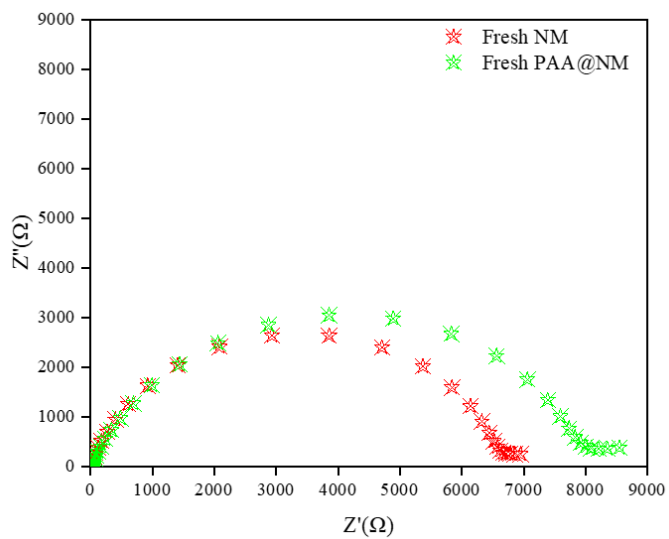


Figure S 8. Nyquist plot of fresh NM and PAA@NM cathode

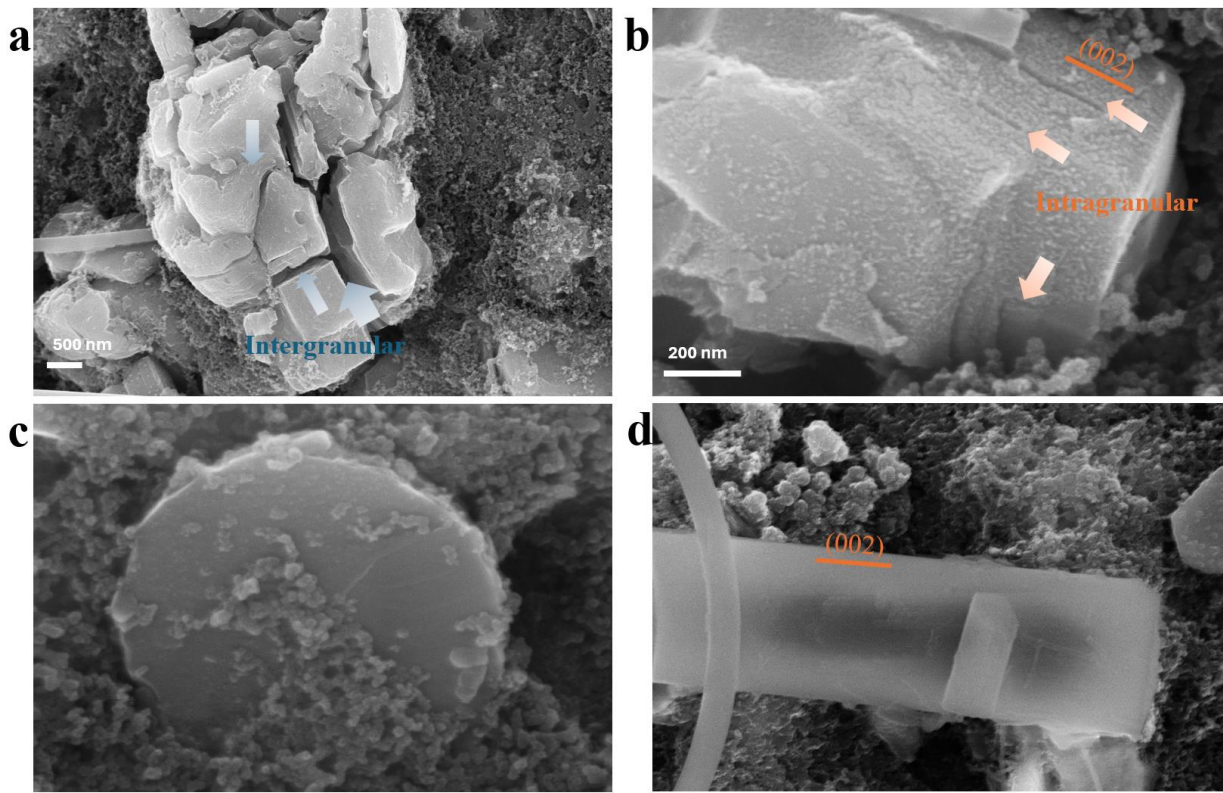


Figure S 9. Additional SEM images of cycled cathode. a-b) NM cathode. c-d) 2PAA@NM cathode.

References

- [1] T. Jin, H. Li, K. Zhu, P.-F. Wang, P. Liu, L. Jiao, *Chemical Society Reviews* **2020**, *49*, 2342.
- [2] P.-F. Wang, Y. You, Y.-X. Yin, Y.-G. Guo, *Advanced Energy Materials* **2018**, *8*, 1701912.
- [3] P. Moreau, D. Guyomard, J. Gaubicher, F. Boucher, *Chem. Mater.* **2010**, *22*, 4126.
- [4] M. Avdeev, Z. Mohamed, C. D. Ling, J. Lu, M. Tamaru, A. Yamada, P. Barpanda, *Inorg Chem* **2013**, *52*, 8685.
- [5] S. Kajiyama, K. Kai, M. Okubo, A. Yamada, *Electrochemistry* **2016**, *84*, 234.
- [6] P. Barpanda, T. Ye, S. Nishimura, S.-C. Chung, Y. Yamada, M. Okubo, H. Zhou, A. Yamada, *Electrochemistry Communications* **2012**, *24*, 116.
- [7] P. Barpanda, G. Liu, M. Avdeev, A. Yamada, *ChemElectroChem* **2014**, *1*, 1488.
- [8] L. Li, Y. Xu, X. Sun, R. Chang, Y. Zhang, X. Zhang, J. Li, *Advanced Energy Materials* **2018**, *8*, 1801064.
- [9] W. Pan, W. Guan, S. Liu, B. B. Xu, C. Liang, H. Pan, M. Yan, Y. Jiang, *J. Mater. Chem. A* **2019**, *7*, 13197.
- [10] W. Guan, B. Pan, P. Zhou, J. Mi, D. Zhang, J. Xu, Y. Jiang, *ACS Appl. Mater. Interfaces* **2017**, *9*, 22369.
- [11] C. Delmas, C. Fouassier, P. Hagenmuller, *Physica B+C* **1980**, *99*, 81.
- [12] N. Yabuuchi, K. Kubota, M. Dahbi, S. Komaba, *Chem. Rev.* **2014**, *114*, 11636.
- [13] E. M. Lotfabad, J. Ding, K. Cui, A. Kohandehghan, W. P. Kalisvaart, M. Hazelton, D. Mitlin, *ACS Nano* **2014**, *8*, 7115.
- [14] D. A. Stevens, J. R. Dahn, *J. Electrochem. Soc.* **2000**, *147*, 1271.
- [15] E. Irisarri, A. Ponrouch, M. R. Palacin, *J. Electrochem. Soc.* **2015**, *162*, A2476.
- [16] K. Chayambuka, G. Mulder, D. L. Danilov, P. H. L. Notten, *Advanced Energy Materials* **2018**, *8*, 1800079.
- [17] A. Ponrouch, D. Monti, A. Boschini, B. Steen, P. Johansson, M. R. Palacín, *J. Mater. Chem. A* **2014**, *3*, 22.
- [18] S. Komaba, C. Takei, T. Nakayama, A. Ogata, N. Yabuuchi, *Electrochemistry Communications* **2010**, *12*, 355.
- [19] C. Didier, M. Guignard, C. Denage, O. Szajwaj, S. Ito, I. Saadoune, J. Darriet, C. Delmas, *Electrochem. Solid-State Lett.* **2011**, *14*, A75.
- [20] Á. Caballero, L. Hernán, L. Sánchez, J. Santos-Peña, M. Aranda, *Journal of Materials Chemistry - J MATER CHEM* **2002**, *12*, 1142.
- [21] N. Yabuuchi, M. Kajiyama, J. Iwatate, H. Nishikawa, S. Hitomi, R. Okuyama, R. Usui, Y. Yamada, S. Komaba, *Nature Mater* **2012**, *11*, 512.
- [22] Z. Lu, J. R. Dahn, *J. Electrochem. Soc.* **2001**, *148*, A1225.
- [23] R. Berthelot, D. Carlier, C. Delmas, *Nature Mater* **2011**, *10*, 74.
- [24] M. Sathiyaa, Q. Jacquet, M.-L. Doublet, O. M. Karakulina, J. Hadermann, J.-M. Tarascon, *Advanced Energy Materials* **2018**, *8*, 1702599.
- [25] T.-Y. Yu, H.-H. Ryu, G. Han, Y.-K. Sun, *Advanced Energy Materials* **2020**, *10*, 2001609.
- [26] X. Rong, E. Hu, Y. Lu, F. Meng, C. Zhao, X. Wang, Q. Zhang, X. Yu, L. Gu, Y.-S. Hu, H. Li, X. Huang, X.-Q. Yang, C. Delmas, L. Chen, *Joule* **2019**, *3*, 503.
- [27] K. Wang, P. Yan, M. Sui, *Nano Energy* **2018**, *54*, 148.
- [28] S. Guo, Q. Li, P. Liu, M. Chen, H. Zhou, *Nat Commun* **2017**, *8*, 135.
- [29] L. Chen, B. Kishore, M. Walker, C. E. J. Dancer, E. Kendrick, *Chem. Commun.* **2020**, *56*, 11609.

- [30] H. Ji, J. Zhai, G. Chen, X. Qiu, H. Fang, T. Zhang, Z. Huang, W. Zhao, Z. Wang, M. Chu, R. Wang, C. Wang, R. Li, W. Zeng, X. Wang, Y. Xiao, *Advanced Functional Materials* **2022**, *32*, 2109319.
- [31] F. Cheng, M. Cao, Q. Li, C. Fang, J. Han, Y. Huang, *ACS Nano* **2023**, *17*, 18608.
- [32] K. Kubota, S. Komaba, *J. Electrochem. Soc.* **2015**, *162*, A2538.
- [33] D. Buchholz, L. G. Chagas, C. Vaalma, L. Wu, S. Passerini, *J. Mater. Chem. A* **2014**, *2*, 13415.
- [34] M. Roger, D. J. P. Morris, D. A. Tennant, M. J. Gutmann, J. P. Goff, J.-U. Hoffmann, R. Feyerherm, E. Dudzik, D. Prabhakaran, A. T. Boothroyd, N. Shannon, B. Lake, P. P. Deen, *Nature* **2007**, *445*, 631.
- [35] Y. Wang, R. Xiao, Y.-S. Hu, M. Avdeev, L. Chen, *Nat Commun* **2015**, *6*, 6954.
- [36] G. Zhang, J. Li, Y. Fan, Y. Liu, P. Zhang, X. Shi, J. Ma, R. Zhang, Y. Huang, *Energy Storage Materials* **2022**, *51*, 559.
- [37] H. Liu, X. Gao, J. Chen, J. Gao, H. Wang, Y. Mei, H. Liu, W. Deng, G. Zou, H. Hou, X. Ji, *Journal of Energy Chemistry* **2022**, *75*, 478.
- [38] C. Cheng, H. Hu, C. Yuan, X. Xia, J. Mao, K. Dai, L. Zhang, *Energy Storage Materials* **2022**, *52*, 10.
- [39] P. Ma, W. Kang, Y. Wang, D. Cao, L. Fan, D. Sun, *Applied Surface Science* **2020**, *529*, 147105.
- [40] J. Wang, H. Liu, Q. Yang, B. Hu, F. Geng, C. Zhao, Y. Lin, B. Hu, *ACS Appl. Mater. Interfaces* **2020**, *12*, 34848.
- [41] W. Zheng, Q. Liu, Z. Wang, Z. Wu, S. Gu, L. Cao, K. Zhang, J. Fransaer, Z. Lu, *Energy Storage Materials* **2020**, *28*, 300.
- [42] T. Chen, W. Liu, F. Liu, Y. Luo, Y. Zhuo, H. Hu, J. Guo, J. Yan, K. Liu, *ACS Appl. Energy Mater.* **2019**, *2*, 844.
- [43] J. Deng, W.-B. Luo, X. Lu, Q. Yao, Z. Wang, H.-K. Liu, H. Zhou, S.-X. Dou, *Advanced Energy Materials* **2018**, *8*, 1701610.
- [44] T. Chen, W. Liu, H. Gao, Y. Zhuo, H. Hu, A. Chen, J. Zhang, J. Yan, K. Liu, *Journal of Materials Chemistry A* **2018**, *6*, 12582.
- [45] L. Wang, Y.-G. Sun, L.-L. Hu, J.-Y. Piao, J. Guo, A. Manthiram, J. Ma, A.-M. Cao, *J. Mater. Chem. A* **2017**, *5*, 8752.
- [46] I. Hasa, S. Passerini, J. Hassoun, *J. Mater. Chem. A* **2017**, *5*, 4467.
- [47] Y. Shi, S. Li, A. Gao, J. Zheng, Q. Zhang, X. Lu, L. Gu, D. Cao, *ACS Appl. Mater. Interfaces* **2019**, *11*, 24122.
- [48] Y. Zhang, Y. Pei, W. Liu, S. Zhang, J. Xie, J. Xia, S. Nie, L. Liu, X. Wang, *Chemical Engineering Journal* **2020**, *382*, 122697.
- [49] C. Cheng, M. Ding, T. Yan, J. Jiang, J. Mao, X. Feng, T.-S. Chan, N. Li, L. Zhang, *Small Methods* **2022**, *6*, 2101524.
- [50] Q. Ni, Y. Zhao, X. Yuan, J. Li, H. Jin, *Small* **2022**, *18*, 2200289.
- [51] L. Yang, X. Li, X. Ma, S. Xiong, P. Liu, Y. Tang, S. Cheng, Y.-Y. Hu, M. Liu, H. Chen, *Journal of Power Sources* **2018**, *381*, 171.
- [52] L. Yang, X. Li, J. Liu, S. Xiong, X. Ma, P. Liu, J. Bai, W. Xu, Y. Tang, Y.-Y. Hu, M. Liu, H. Chen, *J. Am. Chem. Soc.* **2019**, *141*, 6680.
- [53] S. Li, Y. Xiao, Y.-F. Zhu, Y.-C. Li, T. Chen, D. Wang, Y.-H. Liu, H. Liu, Y. Li, C. Li, G.-K. Wang, Y.-X. Liu, Y. Song, Z.-G. Wu, B.-H. Zhong, X.-D. Guo, *Chemical Engineering Journal* **2021**, *412*, 128719.
- [54] T. Jin, P.-F. Wang, Q.-C. Wang, K. Zhu, T. Deng, J. Zhang, W. Zhang, X.-Q. Yang, L. Jiao, C. Wang, *Angewandte Chemie International Edition* **2020**, *59*, 14511.

- [55] C. Zhao, Z. Yao, Q. Wang, H. Li, J. Wang, M. Liu, S. Ganapathy, Y. Lu, J. Cabana, B. Li, X. Bai, A. Aspuru-Guzik, M. Wagemaker, L. Chen, Y.-S. Hu, *J. Am. Chem. Soc.* **2020**, *142*, 5742.
- [56] E. de la Llave, E. Talaie, E. Levi, P. K. Nayak, M. Dixit, P. T. Rao, P. Hartmann, F. Chesneau, D. T. Major, M. Greenstein, D. Aurbach, L. F. Nazar, *Chem. Mater.* **2016**, *28*, 9064.
- [57] L. Li, G. Su, C. Lu, X. Ma, L. Ma, H. Wang, Z. Cao, *Chemical Engineering Journal* **2022**, *446*, 136923.
- [58] Y. Wang, X. Zhao, J. Jin, Q. Shen, N. Zhang, X. Qu, Y. Liu, L. Jiao, *Energy Storage Materials* **2022**, *47*, 44.
- [59] T. Zhang, H. Ji, X. Hou, W. Ji, H. Fang, Z. Huang, G. Chen, T. Yang, M. Chu, S. Xu, Z. Chen, C. Wang, W. Yang, J. Yang, X. Ma, K. Sun, D. Chen, M. Tao, Y. Yang, J. Zheng, F. Pan, Y. Xiao, *Nano Energy* **2022**, *100*, 107482.
- [60] Y. Xiao, Y.-F. Zhu, H.-R. Yao, P.-F. Wang, X.-D. Zhang, H. Li, X. Yang, L. Gu, Y.-C. Li, T. Wang, Y.-X. Yin, X.-D. Guo, B.-H. Zhong, Y.-G. Guo, *Advanced Energy Materials* **2019**, *9*, 1803978.
- [61] J. Billaud, G. Singh, A. R. Armstrong, E. Gonzalo, V. Roddatis, M. Armand, T. Rojo, P. G. Bruce, *Energy Environ. Sci.* **2014**, *7*, 1387.
- [62] R. J. Clément, J. Billaud, A. R. Armstrong, G. Singh, T. Rojo, P. G. Bruce, C. P. Grey, *Energy Environ. Sci.* **2016**, *9*, 3240.
- [63] P.-F. Wang, Y. You, Y.-X. Yin, Y.-S. Wang, L.-J. Wan, L. Gu, Y.-G. Guo, *Angewandte Chemie International Edition* **2016**, *55*, 7445.
- [64] K. Mathiyalagan, K. Karuppiyah, A. Ponnaiah, S. Rengapillai, S. Marimuthu, *International Journal of Energy Research* **2022**, *46*, 10656.
- [65] N. Yabuuchi, R. Hara, K. Kubota, J. Paulsen, S. Kumakura, S. Komaba, *J. Mater. Chem. A* **2014**, *2*, 16851.
- [66] C. Wang, L. Liu, S. Zhao, Y. Liu, Y. Yang, H. Yu, S. Lee, G.-H. Lee, Y.-M. Kang, R. Liu, F. Li, J. Chen, *Nat Commun* **2021**, *12*, 2256.
- [67] Y. Wang, Z. Feng, P. Cui, W. Zhu, Y. Gong, M.-A. Girard, G. Lajoie, J. Trottier, Q. Zhang, L. Gu, Y. Wang, W. Zuo, Y. Yang, J. B. Goodenough, K. Zaghbi, *Nat Commun* **2021**, *12*, 13.
- [68] D. Pahari, S. Puravankara, *Journal of Power Sources* **2020**, *455*, 227957.
- [69] M. Ren, S. Zhao, S. Gao, T. Zhang, M. Hou, W. Zhang, K. Feng, J. Zhong, W. Hua, S. Indris, K. Zhang, J. Chen, F. Li, *J. Am. Chem. Soc.* **2023**, *145*, 224.
- [70] T. Yang, Y. Huang, J. Zhang, H. Zhu, J. Ren, T. Li, L. C. Gallington, S. Lan, L. Yang, Q. Liu, *Journal of Energy Chemistry* **2022**, *73*, 542.
- [71] P.-F. Wang, H.-R. Yao, X. Liu, Y.-X. Yin, J. Zhang, Y. Wen, X. Yu, L. Gu, Y.-G. Guo, *Science Advances* **2018**, *4*, eaar6018.
- [72] X. Cui, S. Wang, X. Ye, X. Fan, C. Gao, Y. Quan, S. Wen, X. Cai, J. Huang, S. Li, *Energy Storage Materials* **2022**, *45*, 1153.
- [73] K. Wang, H. Wan, P. Yan, X. Chen, J. Fu, Z. Liu, H. Deng, F. Gao, M. Sui, *Advanced Materials* **2019**, *31*, 1904816.
- [74] Q.-C. Wang, J.-K. Meng, X.-Y. Yue, Q.-Q. Qiu, Y. Song, X.-J. Wu, Z.-W. Fu, Y.-Y. Xia, Z. Shadik, J. Wu, X.-Q. Yang, Y.-N. Zhou, *J. Am. Chem. Soc.* **2019**, *141*, 840.
- [75] Y. Hou, J. Jin, C. Huo, Y. Liu, S. Deng, J. Chen, *Energy Storage Materials* **2023**, *56*, 87.
- [76] B. Peng, Y. Chen, F. Wang, Z. Sun, L. Zhao, X. Zhang, W. Wang, G. Zhang, *Advanced Materials* **2022**, *34*, 2103210.
- [77] Q. Wang, S. Mariyappan, J. Vergnet, A. M. Abakumov, G. Rousse, F. Rabuel, M. Chakir, J.-M. Tarascon, *Advanced Energy Materials* **2019**, *9*, 1901785.

- [78] S. Li, Y. Zhang, K. Lei, Q. Yang, Z. Liu, K. Jiang, F. Li, Q. Lu, D. Mikhailova, S. Zheng, *Journal of Materials Chemistry A* **2022**, *10*, 10391.
- [79] X. Rong, X. Qi, Y. Lu, Y. Wang, Y. Li, L. Jiang, K. Yang, F. Gao, X. Huang, L. Chen, Y.-S. Hu, *Journal of Energy Chemistry* **2019**, *31*, 132.
- [80] Y. Meng, J. An, L. Chen, G. Chen, L. Shi, M. Lu, D. Zhang, *Chemical Communications* **2020**, *56*, 8079.
- [81] T. Song, L. Chen, D. Gastol, B. Dong, J. F. Marco, F. Berry, P. Slater, D. Reed, E. Kendrick, *Chem. Mater.* **2022**, *34*, 4153.
- [82] H. Yoshida, N. Yabuuchi, K. Kubota, I. Ikeuchi, A. Garsuch, M. Schulz-Dobrick, S. Komaba, *Chem. Commun.* **2014**, *50*, 3677.
- [83] P.-F. Wang, H. Xin, T.-T. Zuo, Q. Li, X. Yang, Y.-X. Yin, X. Gao, X. Yu, Y.-G. Guo, *Angewandte Chemie International Edition* **2018**, *57*, 8178.
- [84] U. Maitra, R. A. House, J. W. Somerville, N. Tapia-Ruiz, J. G. Lozano, N. Guerrini, R. Hao, K. Luo, L. Jin, M. A. Pérez-Osorio, F. Massel, D. M. Pickup, S. Ramos, X. Lu, D. E. McNally, A. V. Chadwick, F. Giustino, T. Schmitt, L. C. Duda, M. R. Roberts, P. G. Bruce, *Nature Chem* **2018**, *10*, 288.
- [85] K. Dai, J. Wu, Z. Zhuo, Q. Li, S. Sallis, J. Mao, G. Ai, C. Sun, Z. Li, W. E. Gent, W. C. Chueh, Y. Chuang, R. Zeng, Z. Shen, F. Pan, S. Yan, L. F. J. Piper, Z. Hussain, G. Liu, W. Yang, *Joule* **2019**, *3*, 518.
- [86] E. Boivin, R. A. House, M. A. Pérez-Osorio, J.-J. Marie, U. Maitra, G. J. Rees, P. G. Bruce, *Joule* **2021**, *5*, 1267.
- [87] J. Vergnet, M. Saubanère, M.-L. Doublet, J.-M. Tarascon, *Joule* **2020**, *4*, 420.
- [88] C. Zhao, C. Chen, B. Hu, W. Tong, H. Liu, B. Hu, C. Li, *Chem. Mater.* **2022**, *34*, 9240.
- [89] R. A. House, U. Maitra, L. Jin, J. G. Lozano, J. W. Somerville, N. H. Rees, A. J. Naylor, L. C. Duda, F. Massel, A. V. Chadwick, S. Ramos, D. M. Pickup, D. E. McNally, X. Lu, T. Schmitt, M. R. Roberts, P. G. Bruce, *Chem. Mater.* **2019**, *31*, 3293.
- [90] R. Qiao, Q. Li, Z. Zhuo, S. Sallis, O. Fuchs, M. Blum, L. Weinhardt, C. Heske, J. Pepper, M. Jones, A. Brown, A. Spucces, K. Chow, B. Smith, P.-A. Glans, Y. Chen, S. Yan, F. Pan, L. F. J. Piper, J. Denlinger, J. Guo, Z. Hussain, Y.-D. Chuang, W. Yang, *Review of Scientific Instruments* **2017**, *88*, 033106.
- [91] Q. Wang, S. Mariyappan, G. Rousse, A. V. Morozov, B. Porcheron, R. Dedryvère, J. Wu, W. Yang, L. Zhang, M. Chakir, M. Avdeev, M. Deschamps, Y.-S. Yu, J. Cabana, M.-L. Doublet, A. M. Abakumov, J.-M. Tarascon, *Nat. Mater.* **2021**, *20*, 353.
- [92] X. Bai, M. Sathiya, B. Mendoza-Sánchez, A. Iadecola, J. Vergnet, R. Dedryvère, M. Saubanère, A. M. Abakumov, P. Rozier, J.-M. Tarascon, *Advanced Energy Materials* **2018**, *8*, 1802379.
- [93] Y. Wang, L. Wang, H. Zhu, J. Chu, Y. Fang, L. Wu, L. Huang, Y. Ren, C.-J. Sun, Q. Liu, X. Ai, H. Yang, Y. Cao, *Advanced Functional Materials* **2020**, *30*, 1910327.
- [94] S. F. Linnell, M. Hirsbrunner, S. Imada, G. Cibin, A. B. Naden, A. V. Chadwick, J. T. S. Irvine, L. C. Duda, A. R. Armstrong, *ChemElectroChem* **2022**, *9*, e202200240.
- [95] X. Qi, L. Wu, Z. Li, Y. Xiang, Y. Liu, K. Huang, E. Yuval, D. Aurbach, X. Zhang, *Advanced Energy Materials* **2022**, *12*, 2202355.
- [96] Z.-Y. Li, X. Ma, K. Sun, L. He, Y. Li, D. Chen, *ACS Appl. Energy Mater.* **2022**, *5*, 1126.
- [97] S. M. Kang, D. Kim, K.-S. Lee, M.-S. Kim, A. Jin, J.-H. Park, C.-Y. Ahn, T.-Y. Jeon, Y. H. Jung, S.-H. Yu, J. Mun, Y.-E. Sung, *Advanced Science* **2020**, *7*, 2001263.
- [98] R. A. House, U. Maitra, M. A. Pérez-Osorio, J. G. Lozano, L. Jin, J. W. Somerville, L. C. Duda, A. Nag, A. Walters, K.-J. Zhou, M. R. Roberts, P. G. Bruce, *Nature* **2020**, *577*, 502.

- [99] A. Gao, Q. Zhang, X. Li, T. Shang, Z. Tang, X. Lu, Y. Luo, J. Ding, W. H. Kan, H. Chen, W. Yin, X. Wang, D. Xiao, D. Su, H. Li, X. Rong, X. Yu, Q. Yu, F. Meng, C. Nan, C. Delmas, L. Chen, Y.-S. Hu, L. Gu, *Nat Sustain* **2022**, *5*, 214.
- [100] E. J. Kim, P. A. Maughan, E. N. Basseby, R. J. Clément, L. A. Ma, L. C. Duda, D. Sehwat, R. Younesi, N. Sharma, C. P. Grey, A. R. Armstrong, *Advanced Energy Materials* **2022**, *12*, 2102325.
- [101] E. J. Kim, T. Hosaka, K. Kubota, R. Tatara, S. Kumakura, S. Komaba, *ACS Appl. Energy Mater.* **2022**, *5*, 12999.
- [102] Z. Yan, L. Tang, Y. Huang, W. Hua, Y. Wang, R. Liu, Q. Gu, S. Indris, S.-L. Chou, Y. Huang, M. Wu, S.-X. Dou, *Angewandte Chemie International Edition* **2019**, *58*, 1412.
- [103] D. Yuan, W. He, F. Pei, F. Wu, Y. Wu, J. Qian, Y. Cao, X. Ai, H. Yang, *J. Mater. Chem. A* **2013**, *1*, 3895.
- [104] W.-L. Pang, X.-H. Zhang, J.-Z. Guo, J.-Y. Li, X. Yan, B.-H. Hou, H.-Y. Guan, X.-L. Wu, *Journal of Power Sources* **2017**, *356*, 80.
- [105] P.-F. Wang, H.-R. Yao, X.-Y. Liu, J.-N. Zhang, L. Gu, X.-Q. Yu, Y.-X. Yin, Y.-G. Guo, *Advanced Materials* **2017**, *29*, 1700210.
- [106] C. Cheng, C. Chen, S. Chu, H. Hu, T. Yan, X. Xia, X. Feng, J. Guo, D. Sun, J. Wu, S. Guo, L. Zhang, *Advanced Materials* **2022**, *34*, 2201152.
- [107] W. Kong, R. Gao, Q. Li, W. Yang, J. Yang, L. Sun, X. Liu, *J. Mater. Chem. A* **2019**, *7*, 9099.
- [108] B. Ouyang, T. Chen, X. Chen, X. Fan, J. Wang, W. Liu, Z. Lu, K. Liu, *Chemical Engineering Journal* **2023**, *452*, 138912.
- [109] G.-H. Yoon, S. Koo, S.-J. Park, J. Lee, C. Koo, S. H. Song, T.-Y. Jeon, H. Kim, J.-S. Bae, W.-J. Moon, S.-P. Cho, D. Kim, S.-H. Yu, *Advanced Energy Materials* **2022**, *12*, 2103384.
- [110] Q. Wang, Y. Liao, X. Jin, C. Cheng, S. Chu, C. Sheng, L. Zhang, B. Hu, S. Guo, H. Zhou, *Angewandte Chemie International Edition* **2022**, *61*, e202206625.
- [111] K. Zhang, D. Kim, Z. Hu, M. Park, G. Noh, Y. Yang, J. Zhang, V. W. Lau, S.-L. Chou, M. Cho, S.-Y. Choi, Y.-M. Kang, *Nat Commun* **2019**, *10*, 5203.
- [112] A. Sarkar, Q. Wang, A. Schiele, M. R. Chellali, S. S. Bhattacharya, D. Wang, T. Brezesinski, H. Hahn, L. Velasco, B. Breitung, *Advanced Materials* **2019**, *31*, 1806236.
- [113] L. Yao, P. Zou, C. Wang, J. Jiang, L. Ma, S. Tan, K. A. Beyer, F. Xu, E. Hu, H. L. Xin, *Advanced Energy Materials* **2022**, *12*, 2201989.
- [114] X.-Y. Du, Y. Meng, H. Yuan, D. Xiao, *Energy Storage Materials* **2023**, *56*, 132.
- [115] F. Ding, C. Zhao, D. Xiao, X. Rong, H. Wang, Y. Li, Y. Yang, Y. Lu, Y.-S. Hu, *J. Am. Chem. Soc.* **2022**, *144*, 8286.
- [116] F. Fu, X. Liu, X. Fu, H. Chen, L. Huang, J. Fan, J. Le, Q. Wang, W. Yang, Y. Ren, K. Amine, S.-G. Sun, G.-L. Xu, *Nat Commun* **2022**, *13*, 2826.
- [117] J. Cho, Y. J. Kim, B. Park, *Chem. Mater.* **2000**, *12*, 3788.
- [118] J. Cho, Y. J. Kim, T.-J. Kim, B. Park, *Angewandte Chemie* **2001**, *113*, 3471.
- [119] M. R. Laskar, D. H. K. Jackson, Y. Guan, S. Xu, S. Fang, M. Dreibelbis, M. K. Mahanthappa, D. Morgan, R. J. Hamers, T. F. Kuech, *ACS Appl. Mater. Interfaces* **2016**, *8*, 10572.
- [120] B. Han, T. Paulauskas, B. Key, C. Peebles, J. S. Park, R. F. Klie, J. T. Vaughey, F. Dogan, *ACS Appl. Mater. Interfaces* **2017**, *9*, 14769.
- [121] Y. Liu, X. Fang, A. Zhang, C. Shen, Q. Liu, H. A. Enaya, C. Zhou, *Nano Energy* **2016**, *27*, 27.
- [122] F. Yu, L. Du, G. Zhang, F. Su, W. Wang, S. Sun, *Advanced Functional Materials* **2020**, *30*, 1906890.
- [123] K. Kaliyappan, J. Liu, A. Lushington, R. Li, X. Sun, *ChemSusChem* **2015**, *8*, 2537.

- [124] J. Alvarado, C. Ma, S. Wang, K. Nguyen, M. Kodur, Y. S. Meng, *ACS Appl. Mater. Interfaces* **2017**, *9*, 26518.
- [125] T. Or, S. W. D. Gourley, K. Kaliyappan, Y. Zheng, M. Li, Z. Chen, *Electrochem. Energy Rev.* **2022**, *5*, 20.
- [126] H.-H. Sun, J.-Y. Hwang, C. S. Yoon, A. Heller, C. B. Mullins, *ACS Nano* **2018**, *12*, 12912.
- [127] K. Kaliyappan, J. Liu, B. Xiao, A. Lushington, R. Li, T.-K. Sham, X. Sun, *Advanced Functional Materials* **2017**, *27*, 1701870.
- [128] H. Ren, L. Zheng, Y. Li, Q. Ni, J. Qian, Y. Li, Q. Li, M. Liu, Y. Bai, S. Weng, X. Wang, F. Wu, C. Wu, *Nano Energy* **2022**, *103*, 107765.
- [129] F. Zhang, J. Liao, L. Xu, W. Wu, X. Wu, *ACS Appl. Mater. Interfaces* **2021**, *13*, 40695.
- [130] C. Yu, L. Yang, S. Sun, D. Chen, Y. Yin, H. Y. Yang, Y. Bai, *Ceramics International* **2022**, *48*, 36715.
- [131] Z. Li, W. Kong, Y. Yu, J. Zhang, D. Wong, Z. Xu, Z. Chen, C. Schulz, M. Bartkowiak, X. Liu, *Angewandte Chemie* **2022**, *134*, e202115552.
- [132] X. Xia, T. Liu, C. Cheng, H. Li, T. Yan, H. Hu, Y. Shen, H. Ju, T.-S. Chan, Z. Wu, Y. Su, Y. Zhao, D. Cao, L. Zhang, *Advanced Materials* **2022**, *n/a*, 2209556.
- [133] K. Tang, Y. Huang, X. Xie, S. Cao, L. Liu, M. Liu, Y. Huang, B. Chang, Z. Luo, X. Wang, *Chemical Engineering Journal* **2020**, *384*, 123234.
- [134] J. H. Jo, J. U. Choi, A. Konarov, H. Yashiro, S. Yuan, L. Shi, Y.-K. Sun, S.-T. Myung, *Advanced Functional Materials* **2018**, *28*, 1705968.
- [135] C.-H. Jo, J.-H. Jo, H. Yashiro, S.-J. Kim, Y.-K. Sun, S.-T. Myung, *Advanced Energy Materials* **2018**, *8*, 1702942.
- [136] K. Kaliyappan, T. Or, Y.-P. Deng, Y. Hu, Z. Bai, Z. Chen, *Advanced Functional Materials* **2020**, *30*, 1910251.
- [137] J. Zhang, Q. Lu, J. Fang, J. Wang, J. Yang, Y. NuLi, *ACS Appl. Mater. Interfaces* **2014**, *6*, 17965.
- [138] H. Yang, R.-M. Gao, X.-D. Zhang, J.-Y. Liang, X.-H. Meng, Z.-Y. Lu, F.-F. Cao, H. Ye, *Advanced Materials* **2022**, *34*, 2204835.
- [139] E. Lee, J. Lu, Y. Ren, X. Luo, X. Zhang, J. Wen, D. Miller, A. DeWahl, S. Hackney, B. Key, D. Kim, M. D. Slater, C. S. Johnson, *Advanced Energy Materials* **2014**, *4*, 1400458.
- [140] S. Guo, P. Liu, H. Yu, Y. Zhu, M. Chen, M. Ishida, H. Zhou, *Angewandte Chemie International Edition* **2015**, *54*, 5894.
- [141] Z.-Y. Li, J. Zhang, R. Gao, H. Zhang, L. Zheng, Z. Hu, X. Liu, *J. Phys. Chem. C* **2016**, *120*, 9007.
- [142] J. E. Wang, H. Kim, Y. H. Jung, D. K. Kim, D. J. Kim, *Small* **2021**, *17*, 2100146.
- [143] Q. Huang, M. Wang, L. Zhang, S. Qi, Y. Feng, P. He, X. Ji, P. Wang, L. Zhou, S. Chen, W. Wei, *Energy Storage Materials* **2022**, *45*, 389.
- [144] Y. Xiao, H.-R. Wang, H.-Y. Hu, Y.-F. Zhu, S. Li, J.-Y. Li, X.-W. Wu, S.-L. Chou, *Advanced Materials* **2022**, *34*, 2202695.
- [145] L. G. Chagas, D. Buchholz, C. Vaalma, L. Wu, S. Passerini, *Journal of Materials Chemistry A* **2014**, *2*, 20263.
- [146] X. Chen, X. Zhou, M. Hu, J. Liang, D. Wu, J. Wei, Z. Zhou, *J. Mater. Chem. A* **2015**, *3*, 20708.
- [147] Y.-N. Zhou, P.-F. Wang, Y.-B. Niu, Q. Li, X. Yu, Y.-X. Yin, S. Xu, Y.-G. Guo, *Nano Energy* **2019**, *55*, 143.
- [148] N. Jiang, Q. Liu, J. Wang, W. Yang, W. Ma, L. Zhang, Z. Peng, Z. Zhang, *Small* **2021**, *17*, 2007103.

- [149] Z.-G. Wu, J.-T. Li, Y.-J. Zhong, X.-D. Guo, L. Huang, B.-H. Zhong, D.-A. Agyeman, J.-M. Lim, D. Kim, M. Cho, Y.-M. Kang, *ACS Appl. Mater. Interfaces* **2017**, *9*, 21267.
- [150] H. Chen, Z. Wu, Z. Zheng, T. Chen, X. Guo, J. Li, B. Zhong, *Electrochimica Acta* **2018**, *273*, 63.
- [151] T.-R. Chen, T. Sheng, Z.-G. Wu, J.-T. Li, E.-H. Wang, C.-J. Wu, H.-T. Li, X.-D. Guo, B.-H. Zhong, L. Huang, S.-G. Sun, *ACS Appl. Mater. Interfaces* **2018**, *10*, 10147.
- [152] J. Qu, T. Sheng, Z. Wu, T. Chen, H. Chen, Z. Yang, X. Guo, J. Li, B. Zhong, X. Dou, *Journal of Materials Chemistry A* **2018**, *6*, 13934.
- [153] Y. Xiao, P.-F. Wang, Y.-X. Yin, Y.-F. Zhu, X. Yang, X.-D. Zhang, Y. Wang, X.-D. Guo, B.-H. Zhong, Y.-G. Guo, *Advanced Energy Materials* **2018**, *8*, 1800492.
- [154] Y. Xiao, Y.-F. Zhu, W. Xiang, Z.-G. Wu, Y.-C. Li, J. Lai, S. Li, E. Wang, Z.-G. Yang, C.-L. Xu, B.-H. Zhong, X.-D. Guo, *Angewandte Chemie* **2020**, *132*, 1507.
- [155] G. Gao, D. Tie, H. Ma, H. Yu, S. Shi, B. Wang, S. Xu, L. Wang, Y. Zhao, *J. Mater. Chem. A* **2018**, *6*, 6675.
- [156] Q. Huang, Y. Feng, S. Xu, L. Xiao, P. He, X. Ji, P. Wang, L. Zhou, W. Wei, *ChemElectroChem* **2020**, *7*, 4383.
- [157] Z. Lin, X. Guo, Z. Wang, B. Wang, S. He, L. A. O'Dell, J. Huang, H. Li, H. Yu, L. Chen, *Nano Energy* **2020**, *73*, 104786.
- [158] N. Du, C. Wong, M. Feurstein, O. A. Sadik, C. Umbach, B. Sammakia, *Langmuir* **2010**, *26*, 14194.
- [159] Q. Zhang, L. Yue, R. Yan, D.-J. Liaw, J. Shi, Z. Li, C. Liang, Y. Cheng, Z. Ge, Y. Zhang, *Macromol Rapid Commun* **2023**, *44*, e2300092.
- [160] İ. Yazgan, *Polym. Bull.* **2020**, *77*, 1191.
- [161] J. Hu, C. Lai, K. Chen, Q. Wu, Y. Gu, C. Wu, C. Li, *Nat Commun* **2022**, *13*, 7914.
- [162] C.-Z. Zhao, Q. Zhao, X. Liu, J. Zheng, S. Stalin, Q. Zhang, L. A. Archer, *Advanced Materials* **2020**, *32*, 1905629.
- [163] A. M. Stephan, K. S. Nahm, M. Anbu Kulandainathan, G. Ravi, J. Wilson, *European Polymer Journal* **2006**, *42*, 1728.
- [164] C. Hakim, N. Sabi, L. A. Ma, M. Dahbi, D. Brandell, K. Edström, L. C. Duda, I. Saadoun, R. Younesi, *Commun Chem* **2020**, *3*, 1.
- [165] M. Kim, E. Seok, J. Park, S. Lee, H. Kang, M. Ku, K. Yoon Chung, H. Jung, W. Choi, *Chemical Engineering Journal* **2022**, *450*, 137939.
- [166] Q. Ye, F. Zhou, W. Liu, *Chem. Soc. Rev.* **2011**, *40*, 4244.
- [167] D. N. G. Krishna, J. Philip, *Applied Surface Science Advances* **2022**, *12*, 100332.
- [168] Z. Shadike, E. Zhao, Y.-N. Zhou, X. Yu, Y. Yang, E. Hu, S. Bak, L. Gu, X.-Q. Yang, *Advanced Energy Materials* **2018**, *8*, 1702588.
- [169] M. Zarrabeitia, F. Nobili, O. Lakuntza, J. Carrasco, T. Rojo, M. Casas-Cabanas, M. Á. Muñoz-Márquez, *Commun Chem* **2022**, *5*, 1.
- [170] W. Zuo, J. Qiu, X. Liu, F. Ren, H. Liu, H. He, C. Luo, J. Li, G. F. Ortiz, H. Duan, J. Liu, M.-S. Wang, Y. Li, R. Fu, Y. Yang, *Nat Commun* **2020**, *11*, 3544.
- [171] D. Ji, T. Li, Y. Zou, M. Chu, K. Zhou, J. Liu, G. Tian, Z. Zhang, X. Zhang, L. Li, D. Wu, H. Dong, Q. Miao, H. Fuchs, W. Hu, *Nat Commun* **2018**, *9*, 2339.
- [172] G. Greczynski, L. Hultman, *Vacuum* **2022**, *205*, 111463.
- [173] L. H. Grey, H.-Y. Nie, M. C. Biesinger, *Applied Surface Science* **2024**, *653*, 159319.
- [174] J. Lu, C. Zhan, T. Wu, J. Wen, Y. Lei, A. J. Kropf, H. Wu, D. J. Miller, J. W. Elam, Y.-K. Sun, X. Qiu, K. Amine, *Nat Commun* **2014**, *5*, 5693.

- [175] H. Q. Pham, G. Kim, H. M. Jung, S.-W. Song, *Advanced Functional Materials* **2018**, *28*, 1704690.
- [176] M. Ma, F. Shao, P. Wen, K. Chen, J. Li, Y. Zhou, Y. Liu, M. Jia, M. Chen, X. Lin, *ACS Energy Lett.* **2021**, *6*, 4255.
- [177] M. Jia, P. Wen, Z. Wang, Y. Zhao, Y. Liu, J. Lin, M. Chen, X. Lin, *Advanced Functional Materials* **2021**, *31*, 2101736.
- [178] Q. Shen, Y. Liu, X. Zhao, J. Jin, X. Song, Y. Wang, X. Qu, L. Jiao, *Advanced Energy Materials* **2022**, *n/a*, 2203216.
- [179] K. W. Nam, S. Kim, E. Yang, Y. Jung, E. Levi, D. Aurbach, J. W. Choi, *Chem. Mater.* **2015**, *27*, 3721.
- [180] Q. Yang, P.-F. Wang, J.-Z. Guo, Z.-M. Chen, W.-L. Pang, K.-C. Huang, Y.-G. Guo, X.-L. Wu, J.-P. Zhang, *ACS Appl. Mater. Interfaces* **2018**, *10*, 34272.
- [181] L. Zhang, J. Wu, N. Sun, X. Zhang, L. Jiang, *Journal of Materials Chemistry A* **2014**, *2*, 7666.
- [182] A. D. Mohanty, C. Bae, in *Advances in Organometallic Chemistry* (Ed.: P. J. Pérez), Academic Press, **2015**, pp. 1–39.
- [183] J. Du, C. Pu, X. Sun, Q. Wang, H. Niu, D. Wu, *Polymers* **2023**, *15*, 1032.
- [184] J. M. Dennis, T. R. Long, A. Krishnamurthy, N. T. Tran, B. A. Patterson, C. E. Busch, K. A. Masser, J. L. Lenhart, D. B. Jr. Knorr, *ACS Appl. Polym. Mater.* **2020**, *2*, 2414.
- [185] F. Bao, Z. Dong, R. Zhang, F. Qi, X. Dai, X. Qiu, *Journal of Materials Research and Technology* **2021**, *12*, 1143.
- [186] M. Jin, J. Wang, K. Weng, T. Sun, D. Guo, X. Wang, X. Chen, S. Wang, *Advanced Engineering Materials* **2023**, *25*, 2201390.
- [187] Z. Li, J. Fu, X. Zhou, S. Gui, L. Wei, H. Yang, H. Li, X. Guo, *Advanced Science* **2023**, *10*, 2201718.